A Comparison of The Performance of A Low Voltage Microprobe For Two Thermal Field Emitters

Jia Zheng Li
B.S. Science and Technology University of China, 1967

A dissertation submitted to the faculty
of the Oregon Graduate Center
in partial fulfillment of the
requirements for the degree
Doctor of Philosophy
in
Applied Physics
March, 1986

The dissertation "The comparison of The Performance of A Low Voltage Microprobe For Two Thermal Field Emitters" by Jia Zheng Li, has been examined and approved by the following examination committee:

Dr. Lynwood W. Swanson, thesis advisor

Dr. Jonathan H. Orloff

Dr. Anthony Bell

Dr. Eric Munro, Imperial College, London

ACKNOWLEDGMENTS

I would like to thank my advisor, Professor Lynwood W. Swanson, not only for the benefit of his considerable expertise and experience, but also for being a personal example of great dedication to the cause and for his deep kindness.

Many thanks are also due to the whole "Surface Physics" group: Professor Jon Orloff, Dr. Anthony Bell, Dr. Paul Davis, and Greg Schwind. The friendly atmospherer and nice academic environment was very helpful.

I am grateful to Dave Tuggle for many helpful discussions. The SCWIM program, originally written by Nian-Kan Kang, has proven to be very useful. I could not forget the computer facilities provided by Tektronix Inc. and the powerful word processor made available by the Computer Science Department, OGC.

Tables of Content

List of Figures

List of tables

List of symbols

SYMBOL	DEFINITION
A	emission area
b	faceting length of the ZrO/W emitter
C_C	chromatic aberration coefficient
C_S	spherical aberration coefficient
d	spot size (diameter)
d_b	diameter of the radial broadening disk
d_C	diameter of chromatic aberration disk
d_S	diameter of spherical aberration disk
d_c	diameter of chromatic aberration in source
d_V	virtual source size (diameter)
d_s	diameter of spherical aberration in source
d_d	diameter of diffraction aberration disk
d_g	diameter of Gaussian aberration disk
D	distance between two lenses in column
e	electron charge
E_i	electron intrinsic energy
E_C	electron energy from Boersch effect
ΔE_t	calculated value of FWHM of TED
ΔE	experimental value of FWHM of TED
f	frequency
F	electric field strength
g	emitter protrusion from suppressor
h	Planck's constant
$h_{\theta \text{ or } E \text{ etc}}$	mesh sizes in SCWIM program
i	image when used as suffix
I_t	total emission current
I_P	beam current
ΔI_P	beam current fluctuation
I'	angular intensity
J	current density
k	Boltzmann's constant
L	distance between emitter and anode
M	linear magnification
m	angular magnification
n	electron density
o	object when used as suffix
q	tunneling number
Q	image distance
r	emitter radius
R	anode bore radius or big sphere radius
S	power spectrum density or object distance

S(f)	power spectrum density
T	emitter temperature
V_E	extraction voltage
V_B	beam voltage
V_S	suppressor voltage
v	electron velocity
W	electron normal energy
Z	coordinate along the optical axis
α_o	aperture half angle (in source, $=\alpha$)
α	beam final angle
β	field factor (F/V) or brightness
γ	surface tension
ϵ_o	vacuum permittivity
θ	electro launch angle
μ	Fermi-level
ρ	space charge density
ϕ	work function
Ω	solid angle

ABSTRACT

The Comparison of The Performance of A Low Voltage Microprobe
For Two Thermal Field Emitters

Jia Zheng Li, Ph.D.
Oregon Graduate Center

Supervising Professor: Lynwood W. Swanson

Field emission has long been identified with high brightness electron sources. It is particularly suitable for low voltage, sub-micron focused beam applications. To make full use of this unique feature and to overcome stability problems associated with room temperature field emitters, we investigated long life, low noise, thermal field cathodes capable of operating at a source brightness $\sim 10^{10} A/cm^2/sr$ in a background pressure 1×10^{-8} torr. Two promising cathodes fabricated from the (100) oriented tungsten crystal, the ZrO/W and the built-up W cathodes, were investigated in a comparative manner with respect to several important characteristics including the beam spot size, current transmission, noise level, virtual source size, etc. A commercial scanning electron microscope (SEM) was modified to meet the experimental requirement for the two thermal field emitters.

A special computer simulation program (SCWIM) was used to calculate the emitter surface field, current density and electron trajectories. Space charge was also included in the calculations to show its effect. The virtual source size is an important parameter for calculating the source brightness. Methods previously used for calculating the virtual source size require a particular emitter shape, e.g the sphere and sphere-on-cone models. According to the SCWIM program any arbitrary shaped emitters (facet or other possible geometry) can be easily evaluated. Here, the virtual source size and its relationship with emitter radius and aperture angle were obtained for the both ZrO/W and built-up W(100) emitters.

The experimental results, theoretical prediction and computer simulation calculations were reasonably consistent. They provide a set of practical data and considerations for the development of advanced field emission equipment with a high source angular current intensity ($>$1mA/sr), low beam voltage ($<$1.kV), small beam size ($< 0.2\mu$m), low noise level (noise/signal $\sim$0.5 %), and relatively simple electron optical column (because of smaller virtual source size) with relaxed vacuum requirement. It is shown that the ZrO/W source is generally superior to the built-up emitter owing to its ten times less noise level and smaller energy spread.

Chapter 1

Introduction

A pressing need in the semiconductor industry is the ability to inspect and test semiconducting and insulating surfaces at high resolution without surface charging and specimen damage. One method of addressing this kind of problem is the use of a low voltage (<1.5 kV) beam as a contactless testing probe[1]. Increasingly, the low voltage SEM is being used for inspection of I.C.s and resist patterns, line-width measuring, voltage contrast and stroboscopic SEM etc.

With low beam voltage the secondary electron yield coefficient, δ, increases to unity while the electron's penetration range ($R=KV^{3/2}$) and the energy deposited per electron both decrease[2]; thus the surface charging of insulating samples and distortion of the energy band structure of the devices by trapped electron charges which degrade and possibly destroy their function can be avoided. Also, one may achieve the ultimate in resolution of insulating biological or chemical samples by using low voltage SEM imaging.

The development of low voltage SEM has been delayed by technical limitation of low beam brightness when using a conventional W thermionic cathode. Because of a relatively large virtual source size and smaller emission current density the brightness of a conventional thermionic electron source is limited to low value ($\sim 10^4$ A/cm^2/sr). The conservation law of brightness β is given by

$$\frac{\beta_S}{V_S} = \frac{\beta_i}{V_i} \tag{1-1}$$

where subscript s represents source side and i the image side; this makes low voltage beams suffer further reduction of image brightness.

From the source optics of a field emitter the angular intensity I' can be given by[3]

$$I' = \frac{J_C \, r^2}{m^2} \tag{1-2}$$

where m is angular magnification, J_C is cathode current density, and r is emitter radius as shown in Fig.1-1. The virtual source brightness is

$$\beta_S = \frac{4 \, I'}{d_S^2 \, \pi} \tag{1-3}$$

or

$$\beta_S = \frac{4 \, J_C \, r^2}{\pi \, m^2 d_S^2} \tag{1-4}$$

where d_S is virtual source size. It is obvious that a small value of d_S means high brightness.

Because of the small virtual source size and the high current density the field emitter exhibits a brightness that surpasses that of the thermionic emitter by several orders of magnitude. The small virtual source size also allows a relatively simple optical column to be used because there is no need for further demagnification of the beam size.

The focused beam size (blur disk's diameter), d, of a single lens column can be expressed as

$$d^2 = \left[d_S^2 + (\frac{1}{2} C_S \alpha^3)^2 + (C_C \alpha \frac{\Delta V}{V})^2 + (\frac{15. \times 10^{-7}}{V^{0.5} \alpha})^2 \right] M^2 \qquad (mm) \tag{1-5}$$

where the spherical and chromatic aberration coefficients C_S and C_C are referred to

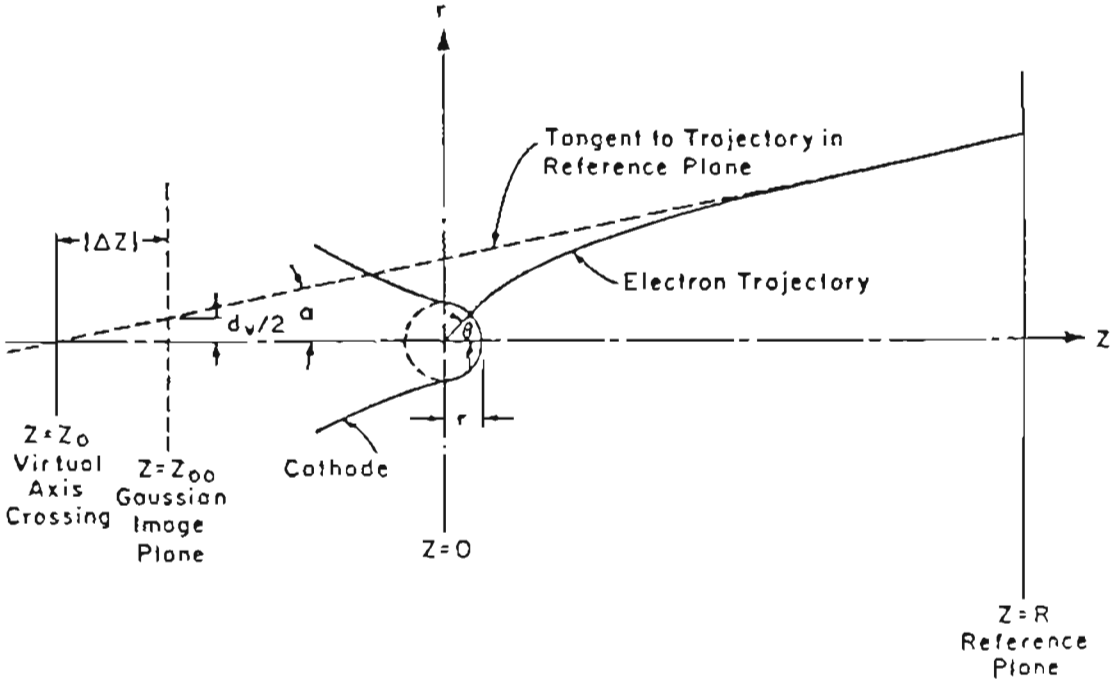

Fig.1-1 : Illustration of typical trajectory and position of virtual axis crossing relative to Gaussian plane

where the spherical and chromatic aberration coefficients C_S and C_C are referred to the object side, M is the total lens magnification, V is the extraction voltage, α is the aperture half angle subtended by emitter and ΔV represents the electron energy spread.

When the chromatic aberration and virtual disks dominate the aberration terms the beam current I_P is given by

$$I_P = (\frac{d^2}{M^2} - d_S^2)\,(\frac{V}{C_C \Delta V})^2\,\pi\, I' = (\frac{d^2}{M^2} - d_S^2)\,(\frac{V}{C_C \Delta V})^2 \frac{\pi J_C\, r^2}{m^2} \qquad (1\text{-}6)$$

Equation (1-6) shows the importance of ΔV, I' , and d_S, which are the source parameters, and M, C_C, and V, which are the column parameters. Thus, for a specified value of d, the beam current, I_P, is proportional to the source parameter, $\frac{I'}{(\Delta V)^2}$ and $(\frac{d^2}{M^2} - d_S^2)$. Therefore, an increased energy spread, ΔV, or column chromatic aberration coefficient, C_C, will play an unfavorable role on beam current and spot size. Thus, the reduction of the beam energy spread and chromatic aberration coefficient must be emphasized when equation (1-6) holds.

Among the field electron sources there are two modes of operation: one is cold field emission (CFE), the other is the thermal field emission. The operating range of the cold emitter is low temperature (room temperature usually) and high field strength ($\sim 10^7$V/cm). The operating range of the thermal field emitter (TFE) is elevated temperature (1800K usually) and lower high electric field ($\sim 10^6$V/cm). The thermal field emitter has several advantages over the cold field emitters. For example, it exhibits a much lower noise level in practical vacuum environments, longer continuous operating time and relaxation of vacuum requirements. There are two types of thermal field emitters developed recently that were used in this investigation. They both use a (100) oriented single crystal tungsten emitter and are known as the built-up W (100) emitter and the zirconium coated W (100) emitter (ZrO/W).

up W (100) emitter and the zirconium coated W (100) emitter (ZrO/W).

The main purpose of this study was to gain understanding of the emission and focusing properties of two different thermal field emitters operating in a low voltage SEM. Measurements included focused beam size, current transmission, noise level, angular current intensity, emitter surface field strength, and the influence of geometrical factors, i.e. emitter radius, suppressor bias, emitter-anode spacing, emitter protrusion and aperture angle. Experimental operating parameters were obtained and compared with theoretical prediction. The results provide a practical basis for comparing the built-up W (100) and ZrO/W thermal field emitters in a low voltage SEM with that of the CFE.

Chapter 2

Electron emission

Electrons may be removed from metals either by excitation of the conduction electrons by heat or photons or by the application of an electric field high enough to enable the electrons to escape from the metal by tunneling through a reduced potential energy barrier. The mechanisms are described by several electron emission theories. In this chapter a brief review of the thermal and field electron emission theories are given.

2.1 Thermionic and Schottky emission

When a metal filament is heated in vacuum, electrons emitted from its surface can be collected on a nearby positively charged plate. This phenomenon called thermionic emission, requires thermal energy for electrons to overcome their binding energy (the work function) in the metal. The energy distribution of these electrons in the solid are assumed to follow Fermi-Dirac statistics

$$f(E) = \frac{1}{e^{(E-\mu)/kT}+1} \tag{2-1}$$

where $f(E)$ gives the probability that a state of energy E will be occupied in thermal equilibrium, μ is Fermi level and is defined as the energy of the topmost filled electron state at absolute zero, and k is Boltzmann's constant. Fig.2-1 gives the model used to define E, μ, and work function ϕ.

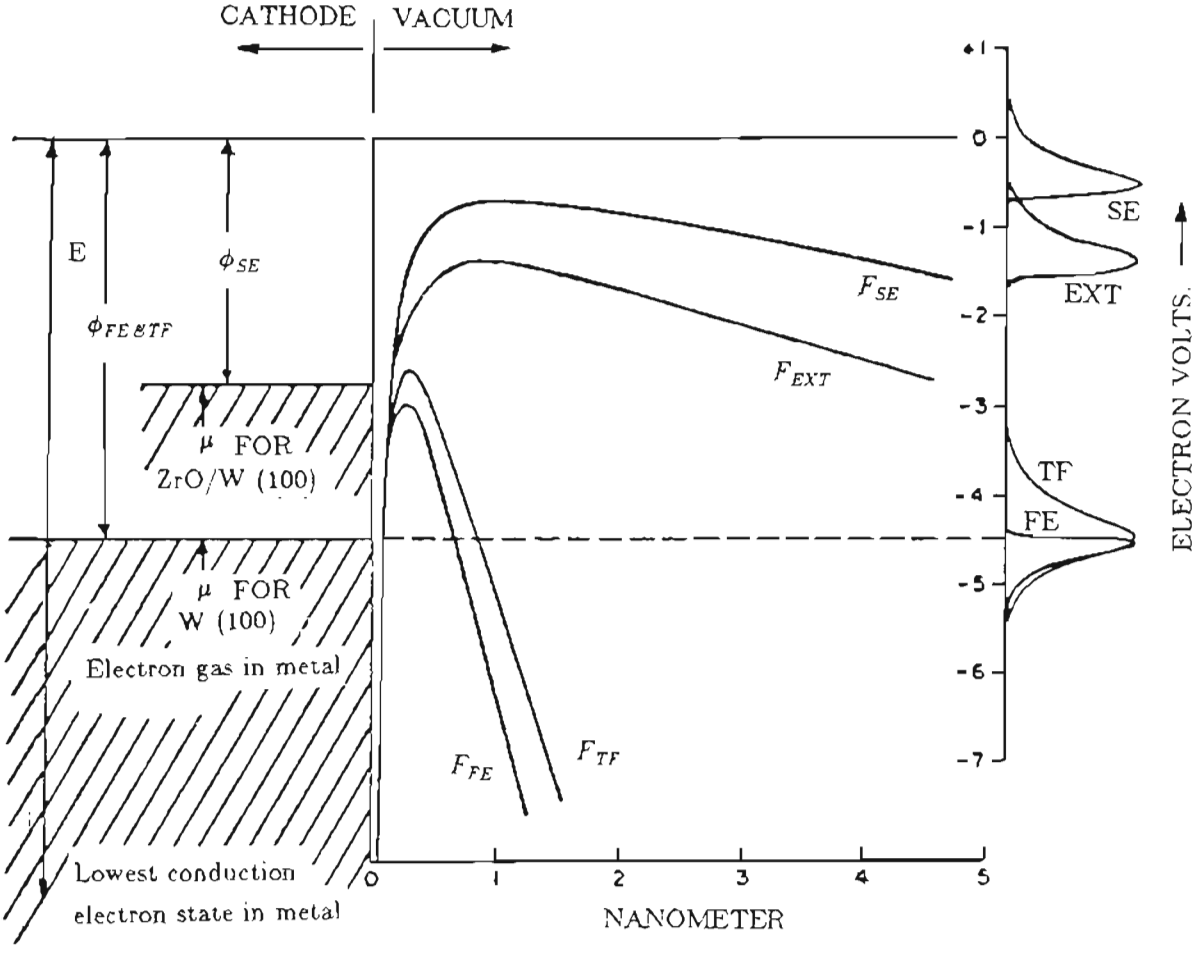

Fig.2-1 : Energy level diagram to define the work function, ϕ, and different emission regimes: SE–Schottky emission, TF–thermal field emission, FE--room temperature field emission, EXT--extended Schottky emission with emitted electron energy distribution shown at the right

One can compute the flux of electrons of energy E> $\phi+\mu$ leaving the metal cathode at any temperature. This will give the current density $J(A/cm^2)$

$$J = e\ n\ v \tag{2-2}$$

where n is the density of high energy electrons, v their mean velocity normal to the surface, and e the electron charge. The value of n is given by

$$n = \int_0^\infty N(E)\, f\,(E)\, dE \tag{2-3}$$

where $N(E)$ in number of electrons per unit energy range[34].

$$N(E) = \frac{1}{2\,\pi^2}\left(\frac{8\pi^2 m}{h^2}\right)^{3/2} E^{1/2} \tag{2-4}$$

One can integrate Eq.(1-3) and obtain n

$$n = \frac{2(2\pi m k T)^{3/2}}{h^3}\ e^{-\phi/kT} \tag{2-5}$$

The mean velocity can be obtained by using a Maxwell-Bolzmann distribution and is given by

$$v = \left(\frac{kT}{2\,\pi m}\right)^{1/2} \tag{2-6}$$

substituting these equations into Eq.(2-2) one gets the well-known Richardson-Dushman Equation[6]

$$J_{OT} = A T^2\ e^{-\phi/kT} \tag{2-7}$$

where $A = 4\pi em\ k^2/h^3 = 120$ (A/cm^2deg^2). The electron flux leaving the surface increases with increasing temperature and decreasing work function.

When a small accelerating electric field F is applied to the surface of a heated cathode the electron emission is referred to as Schottky emission. Schottky[6] made the

first attempt to explain the process in which the height of potential barrier arising from the electron's image force near a metal surface in Fig.2-2(a) is reduced by the application of an external electric field in Fig.2-2(b). As a consequence more electrons are now able to escape into vacuum over this field reduced potential barrier. The amount $\Delta\Phi$ by which the height of the potential barrier is reduced is

$$\Delta\Phi = \frac{-e^2}{16\pi\,\epsilon_0\,x_0} - eFx_0 \tag{2-8}$$

where F is the applied uniform electric field; ϵ_0 is the permittivity of free space; the distance x_0 is the position of maximum of the electron potential near the metal surface under the influence of the applied field and is given by

$$x_0 = \left(\frac{e}{16\,\pi\,\epsilon_0\,F}\right)^{1/2} \tag{2-9}$$

Substituting Eq.(2-9) into Eq.(2-8) the decrease in the work function is given by

$$\Delta\Phi = \left(e^3\frac{F}{4\,\pi\,\epsilon_0}\right)^{1/2} \propto \quad F^{1/2} \tag{2-10}$$

This lowering of the barrier because of the applied field F causes the Richardson Equation to be modified as

$$J_{0S} = J_{0T}\,e^{cF^{1/2}/kT} = 120T^2\,e^{-\phi/kT}\;e^{cF^{1/2}/kT} \tag{2-11}$$

where $c=(\frac{e^3}{4\,\pi\epsilon_0})^{1/2}$ and J_{0T} is given by Eq.(2-7)

2.2 Field emission

Schottky's theory of electron emission holds for field strengths such that tunneling can be neglected. In 1928 a new theory of electron emission by Fowler and Nordheim[6] was developed which took into account tunneling. In their model the

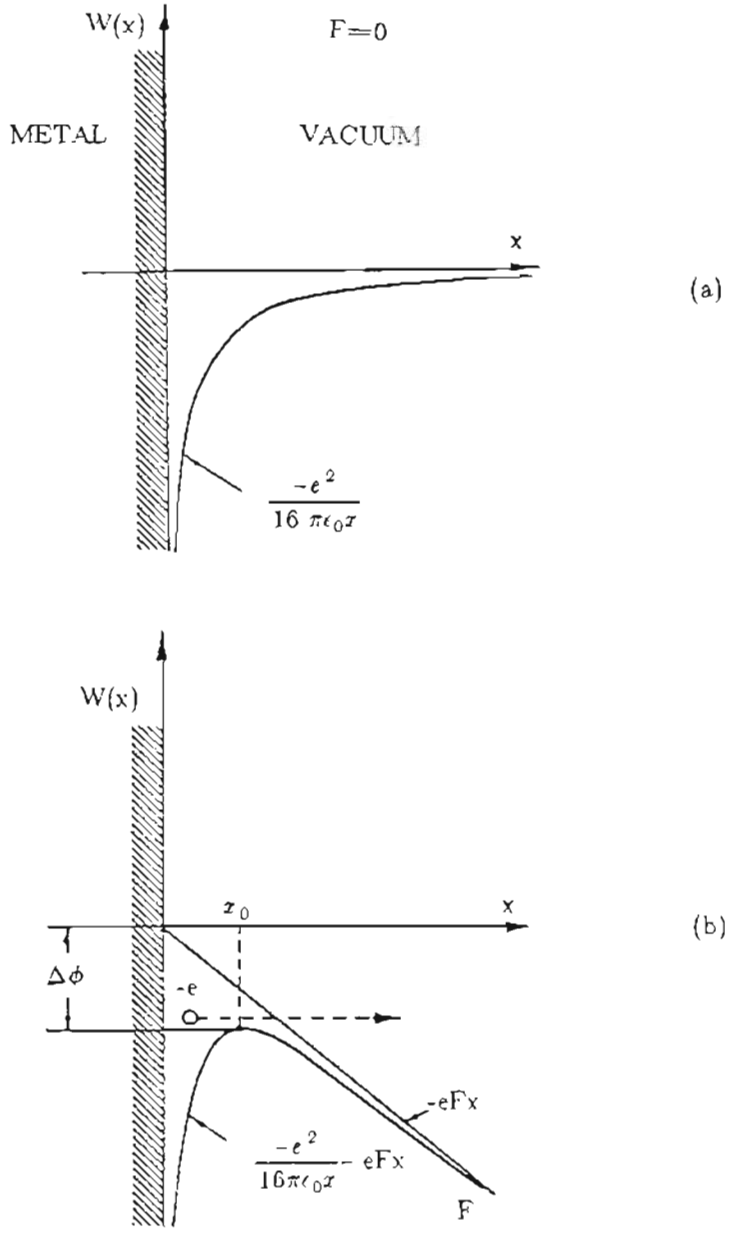

Fig.2-2 : (a) Image potential of an electron near metal surface (Schottky 1923).

(b) Lowering of the image potential barrier by application of an external electric field. Thermal electron escapes into vacuum over "hump", at x_0

conduction electrons, assumed to have a Fermi-Dirac distribution inside the metal, fill various energy levels up to the Fermi level μ. At T=0K no electrons can occupy energy levels above μ. The zero of energy is assumed at the top of the potential well. They considered a field emission process in terms of a one-dimensional tunneling problem. It can be shown quantum mechanically that electrons can penetrate the barrier of such a potential well, if this barrier is lowered, e.g. by means of an added external electric field. The tunneling probability D(W) can be calculated by the WKB method[35] which, for electrons with normal kinetic energy W, yields

$$D(W) \approx e^{-c+(W+\mu)/d} \tag{2-12}$$

where

$$c = \frac{8\pi(2m\,\phi^{3/2})^{1/2}}{3heF}\, v((e^2F)^{1/2}/\phi)$$

$$d = \frac{h\ e\ F}{2\pi(2m\ \phi)^{1/2} t((e^2F)^{1/2}/\phi)}$$

$t((e^2F)^{1/2}/\phi)$ and $v((e^2F)^{1/2}/\phi)$ are slowly varying, tabulated functions[35].

The supply function (number of electrons with total energy within the range E to $E+dE$ and normal energy W to $W+dW$ can be derived as

$$N(W,E)\,dW\,dE = \frac{4\pi m}{h^3}\,\frac{dW\,dE}{\exp((E-\mu)/kT)+1} \tag{2-13}$$

The total energy distribution can be expressed by

$$J(E)\,dE = e\int_{-W_a}^{E} N(W,E)D(W)dW\,dE \tag{2-14}$$

where the integrating limit is from $-W_a$ (about -10.3eV for tungsten) to E. When $W=-W_a$ the integrand is essentially zero and the integration is facilitated by setting the $-W_a$ limit equal to $-\infty$. Carrying out the integration one obtains the total energy distribution

$$J(E) = \frac{4\pi mde}{h^3}\, e^{(-c-\mu/d)} \frac{e^{E/d}}{\exp((E-\mu)/kT)+1}\, dE \tag{2-15}$$

The current density is at a finite temperature J_{TF} is given by[10]

$$J_{TF} = \int_{-\infty}^{\infty} J(E)dE = \frac{4\pi med}{h^3}\, e^{(c-\mu/d)} \frac{akT\ \Gamma(kT/d)\Gamma(1-kT/d)}{a^{(1-kT)/d}} \tag{2-16}$$

where $a = e^{\mu/kT}$, and where

$$\Gamma(P)\ \Gamma(1-P) = \frac{\pi P}{\sin(\pi P)} \tag{2-17}$$

Combining Eqs.(2-16) and (2-17) yields

$$J_{TF} = \frac{e^3F^2}{8\pi h\,\phi t^2}\, e^{\frac{-8\pi(2m)^{1/2}\phi^{2/3}}{3heF}\, v}\, \frac{\pi P}{\sin(\pi P)} \tag{2-18}$$

In the case of cold field emission (T $\rightarrow$ 0K) $\lim_{Z\to 0} \pi P/Sin(\pi P)=1$ and the Eq.(2-18) reduces to the well-known Fowler-Nordheim Equation

$$J_{TF} = \frac{e^3F^2}{8\pi h\,\phi t^2}\, e^{\frac{-8\pi(2m)^{1/2}\phi^{2/3}}{3heF}\, v} \tag{2-19}$$

Eq.(2-18) is valid only in the range for $0<P<0.7$.

2.3 Emission in transition region (extended Schottky emission)

Between Schottky and T-F emission, there is a transition region in which emission occurs both above and below the top of the potential barrier. It can be shown[10] that the current density J_0 given by

$$J_O = J_{OS} \frac{\pi q}{\sin(\pi q)} = \frac{4\pi me(kT)^2}{h^3} e^{-\phi/kT}\, e^{cF^{1/2}/kT}\, \frac{\pi q}{\sin(\pi q)} \tag{2-20}$$

where $q = C_{emu}/kT$, $C_{emu} = \frac{h}{2\pi^2}(e^{1/2}F^{3/2}/2m)^{1/2}$ (in emu unit). J_{0S} is the current density for Schottky emission given in Eq.(2-11). Eq.(2-20) is valid for $0<q<0.75$.

When q=0.5 one-half of the total emitted current is contributed by electrons escaping through the potential barrier by tunneling.

2.4 Range of validity of the various emission theories

The range of validity of the electron emission expressions mentioned above can be put in a diagram according to their cathode temperature and applied electron field to illustrate schematically the range of validity in the case of zirconiated tungsten cathodes where ϕ=2.5eV. As shown in Fig.2-3 there are four major boundaries: CC', AA', DD', GG'.

The first boundary CC' corresponding to the condition

$$F \leq F_1(T) = (2^{3/2}\pi^2 m^{1/2} kT/he^{1/4})^{4/3} \approx 1746\ T^{4/3} \quad \text{(V/cm)} \qquad (2\text{-}21)$$

F_1 depends on the temperature but not on the work function of the cathode. Below the CC', the emission is predominantly thermionic in character. Below the boundary AA' (i.e. for F<0.15 F_1) the simple Schottky formulae hold a good approximation, e.g. to within 10% for total emission current density. Between the boundaries AA' and CC', the current density is given by Eq.(2-20). The second important boundary DD' corresponds to the condition

$$F \geq F_2 \approx 6\pi(m\phi)^{1/2} T/he = 9.4\times10^3 \phi^{1/2} T \quad \text{(V/cm)} \qquad (2\text{-}22)$$

thus, F_2 depends on both temperature and work function. In this region Eq.(2-18) is the proper analytical expression for the current density. Above the boundary DD' the emission is of a field emission rather than thermionic character. Above GG', i.e. for $F > 4.2\ F_2$, the cold field emission (CFE) formulae Eq.(2-19) holds in a good approximation. The boundary EE' (corresponding to $F = 2F_2$) makes the separation between regions where the major fraction of the emitted electrons have initial total energies

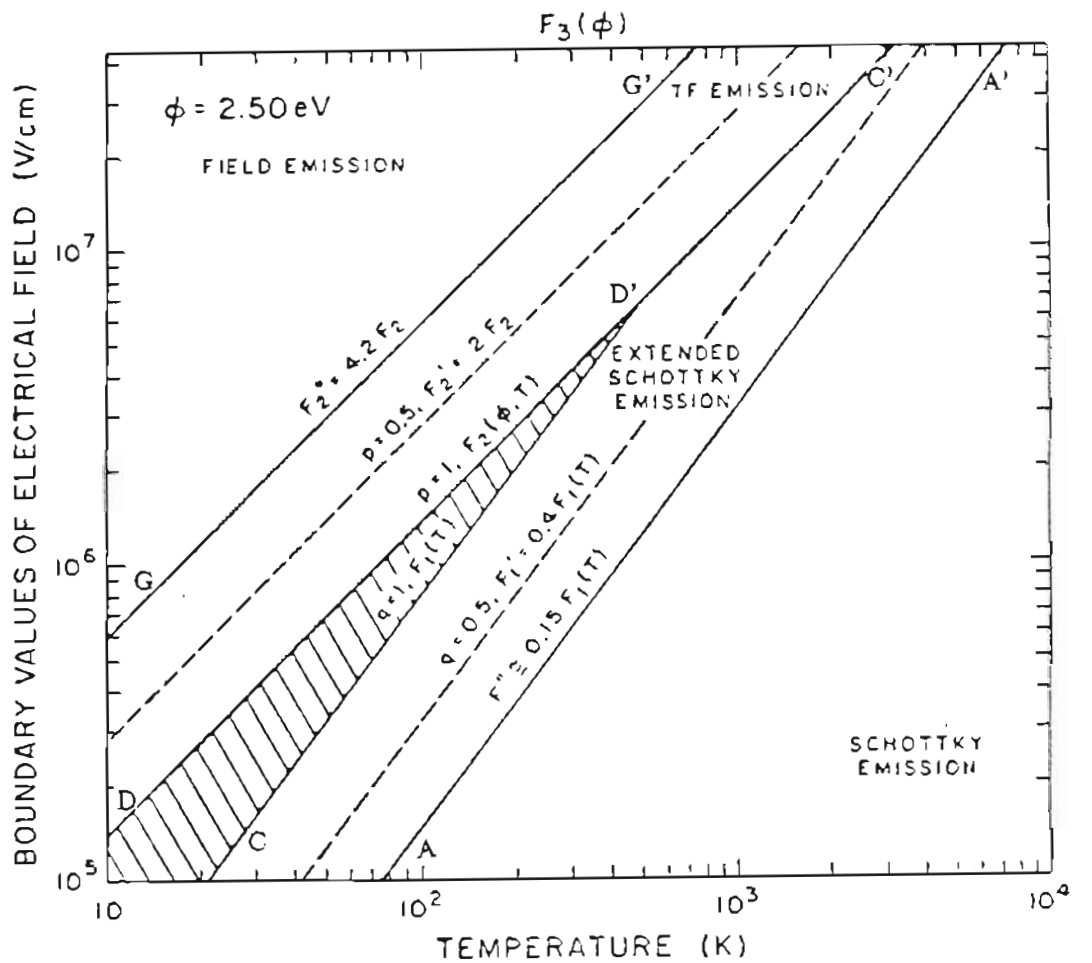

Fig.2-3 : Temperature-field domains for various electron emission mechanisms with ϕ=2.5 eV.

either above or below the Fermi energy.

Finally, the upper boundary HH' corresponds to an applied field

$$F_3 = \phi^2 / e^3 = 7\times10^6 \ \phi^{\ 2} \quad \text{(V/cm)} \tag{2-23}$$

Above this boundary Eq.(2-19) does not apply because the top of the potential barrier is reduced below the Fermi energy. There is no analytical expression between boundaries CC' and DD' (the shaded area) and the T-F emission and the extended Schottky emission equations of J both become inaccurate near the boundaries.

A similar case with ϕ=4.5 ev for pure tungsten cathodes[10] is shown in Fig.2-4.

2.5 Energy distribution for various emissions

The total energy distribution (TED) of emitted electrons is of considerable interest since it provides knowledge of the energy spread of the electrons. The energy distribution is given by[9,12]

$$J(E,W)\,dW\,dE = \frac{4\pi me\ D(W)dW\ dE}{h^3(\exp(E-W)/kT\ +1)} \tag{2-24}$$

where W is the normal energy and E the total energy. By integrating W over the entire possible ranges (numerically or by analytical methods) one can obtain the total energy distribution for the various emission regimes. All 5 emission regimes (thermionic, Schottky, extended Schottky, thermaml field and cold field) are depicted in Fig.2-5 to show the region where analytical approximate formulae exist. The TED for Schottky emission is obtained simply by shifting the zero reference by $E_0=(\frac{e^3F}{4\pi\epsilon_0})^{1/2}$ from the thermionic curve. The extended Schottky curve is shifts more because of the enhanced electric field (see Fig.2-6). The three energy curves show the similar energy spread about 0.4 to 0.5eV (FWHM). The TED's for CFE and TFE show very

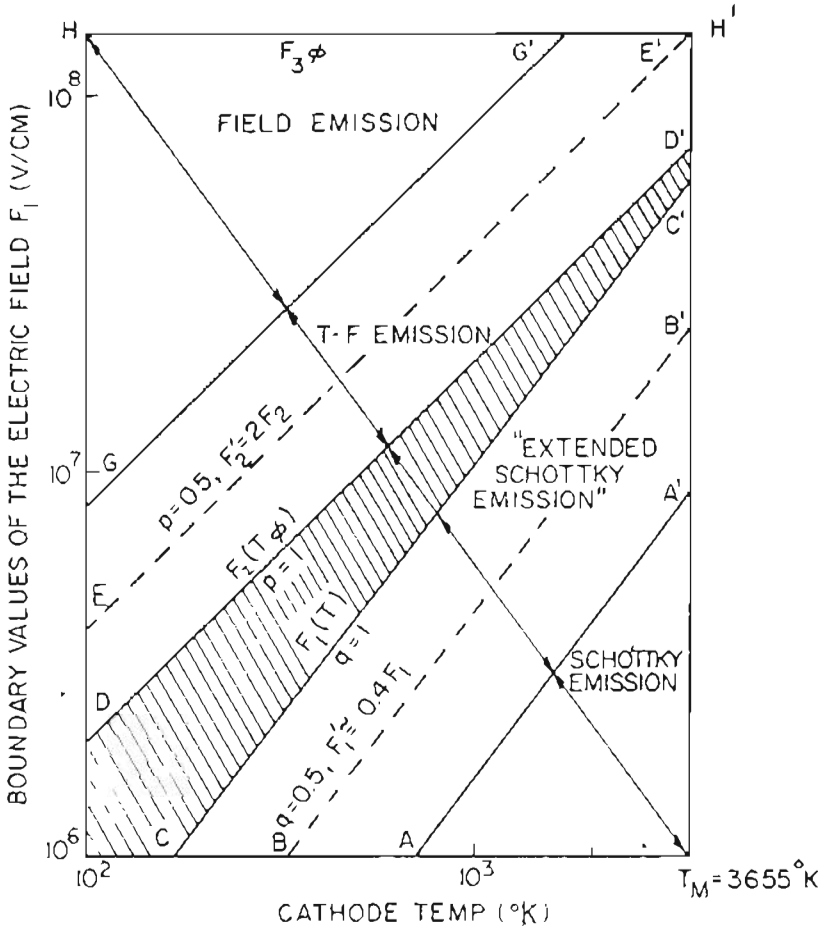

Fig.2-4 : Temperature-field domains for various electron emission mechanisms with ϕ=4.5 eV.

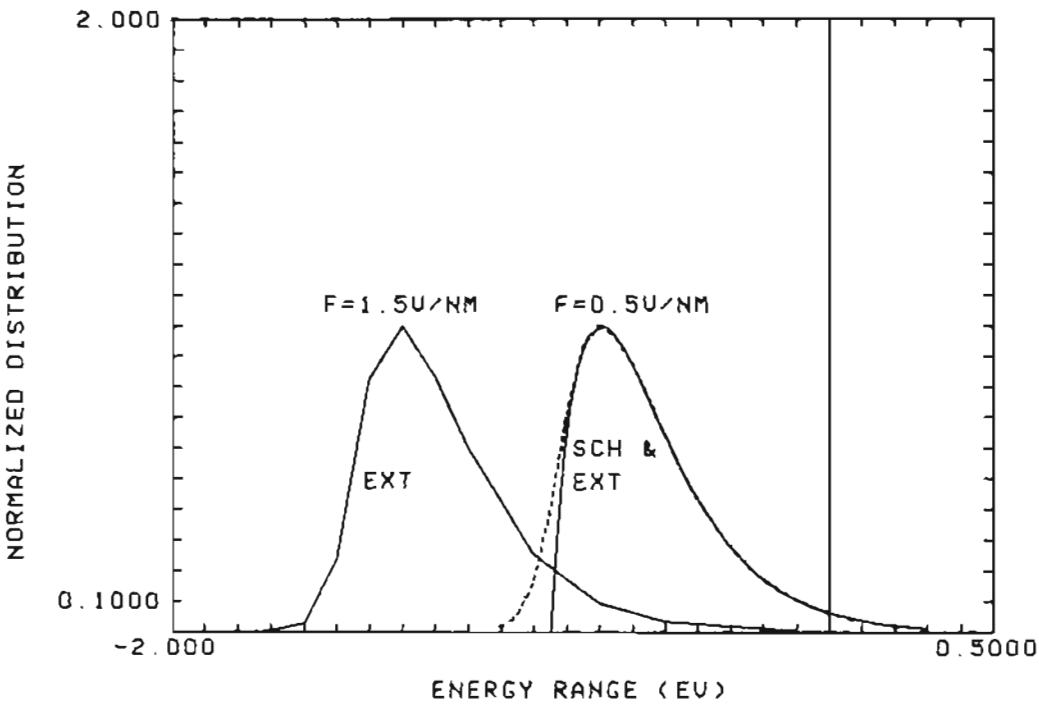

Fig.2-6 : The nearly overlapped solid and dotted curves show the Schottky and extended Schottky emissions at the same electric field respectively and ϕ=2.8eV. The curve at the higher field is the extended Schottky emission which shows shifted zero reference.

different shapes. The CFE has the smallest energy spread about 0.3 eV, but TFE gives a FWHM of $\sim$ 1eV for ϕ=4.5eV.

It must be emphasized that the theoretical energy distribution is not always obtained experimentally due to the well-known Boersch Effect[23]. At high cathode current densities the electrons interact stochastically because of mutual Coulomb repulsion and cause an increased energy spread. Although Boersch used a thermionic cathode this phenomenon has been experimentally verified for point source cathodes[13]. Usually the energy broadening term is added in quadrature with the emission energy distribution term to obtain the total beam energy width. In one theoretical formulation[36] the broadening term takes the form

$$\Delta E \propto \left[\frac{I}{r^{1/2}V^{1/2}\alpha^2}\right]^{2/3} \tag{2-25}$$

where I=emitted current, r=emitter radius, V=beam voltage and α=emission half angle.

If one maintains a relatively low current density this energy broadening effect is minimized and the electron beam contains only the energy distribution due to the emission process. Minimization of the energy spread is particularly important for low voltage beams since chromatic aberration is likely to be the main contributor to focused beam diameter.

Chapter 3

Thermal field emitter

3.1 General features

There are several advantages in operating a field emitter at an elevated temperature. One is the reduction of beam noise. The high emitter temperature desorbs the adsorbed residual gases immediately and maintain a low and constant coverage of the adsorbed gases on the emitter surface, thereby eliminating time dependent work function change which causes flicker noise. From Eq.(2-19) it is shown that $J = J_0 \exp(-b\,\phi^{3/2}/F)$, where b=$6.83\times10^7$, thus, $\frac{dJ}{J} = -\frac{3b}{2F}\phi^{3/2}\frac{d\,\phi}{\phi}$, thus if the work function ϕ changes by 1% it will result in 20% fluctuation of emission current for ϕ=4.5eV and F=5×10^7V/cm.

Another advantage of high temperature operation is a self-annealing effect to smooth the surface roughness as it is created by sputtering due to ions formed by electrons striking the anode. This minimizes the probability of emitter destruction by a vacuum arc and allows a relaxation of vacuum requirement (from 10^{-10} torr for cold field emitter to $2\text{–}3\times10^{-8}$ torr for thermal field emitter).

The third advantage is that the thermal field emitter can provide higher current density and much longer continuous working life (>5000 h). This is primarily because of the two above advantages.

Tungsten is normally used as the emitter material because of such properties as a high melting point, a low vapor pressure, relatively high electrical and thermal conductivity, and high mechanical strength (molybdenum is another choice).

As with any elevated temperature source, an increased flicker noise amplitude over that of a cold emitter is expected. The flicker noise can be related to stochastic processes due to surface diffusion and desorption of an adsorbate. On the assumption that the adsorbed molecule can exist in two states of life time τ_0 and τ_1, the noise spectrum density function W(f) can be given by[10]

$$W(f) = \frac{I^2 kTB^2 (tg^{-1}(2\pi f\ \tau_1) - tg^{-1}(2\pi f\ \tau_0))(\mu_0 N_0 + \mu_1 \tau_1)^2}{2\pi f\ (E_1 - E_0)} \tag{3-1}$$

where f is frequency, μ_0 and μ_1 are dipole moments, N_0 and N_1 are numbers of absorbed molecules for the two states, and $B = 3\pi b\, \phi^{1/2}/F$. It is clear that the flicker noise amplitude is quadratically related to current I and increases linearly with temperature T. However, one kind of thermal emitter (ZrO/W), discussed in detail in section 3.4, reduces this temperature related noise by its large physical emitting area relative to the built-up and cold field emitters.

3.2 Energy spread

According to the previous discussion the beam current I_P in a focused beam dominated by chromatic aberration is inversely proportional to $(\Delta V)^2$ in Eq.(1-6) (or in terms of $\Delta E = e\,\Delta V$). In addition to an intrinsic energy spread $\Delta E_i(\phi, T, F)$, it has been found that a current and emitter radius dependent contribution $\Delta E_C(I, r)$ occurs for all high field sources. That is

$$\Delta E = \Delta E_i(\phi, T, F) + \Delta E_C(I, r) \tag{3-2}$$

The origin of $\Delta E_C(I, r)$ term is believed to be due to the Boersch effect or more

specifically to the relaxation of initial Coulomb potential energy caused by random density fluctuation of charged particles[36].

From the numerical integration of Eq.(2-24) the theoretical energy distribution and, hence, $\Delta E_i(\phi, T, F)$, the FWHM of TED, can be obtained. The results of such a calculation are given in Fig.3-1 as a function of J for specified ϕ values[3]. For typical operating parameters of the ZrO/W TFE ($\phi \approx 2.8eV$, J=10^3 to 10^5A/cm^2, T=1800K) the value of $\Delta E_i < 0.6$eV. On the low temperature side of the maxima in Fig.3-1 curves the emission mode is primarily field emission, whereas on the high temperature side of the maxima the emission mode is primarily Schottky emission and ΔE_i again becomes small with increasing T.

Fig.3-2 shows experimental values of ΔE versus the angular intensity I' for ZrO/W emitters with different apex radii. For $I' \leq 0.1$ mA/sr. ΔE approaches the theoretical value of $\Delta E_i \leq 0.6$eV; however, as I' increases or as r decreases ΔE will increase due to the aforementioned stochastic Coulomb interactions. Thus, in order to reduce the chromatic aberration contribution at high values of I' the emitter radius should be made large.

3.3 Built-up emitter

"Built-up" is a term describing a process by which surface migrating atoms are directed by external electrostatic forces to regions of greatest curvature, eventually reshaping the emitter. In some cases a stable shape is obtained[12].

The condition that the applied electrostatic field stress just balance the thermodynamic dulling force is given by following[29]

$$F = \left(\frac{8\pi\gamma}{r}\right)^{1/2} \qquad (in\ esu\ unit) \tag{3-3}$$

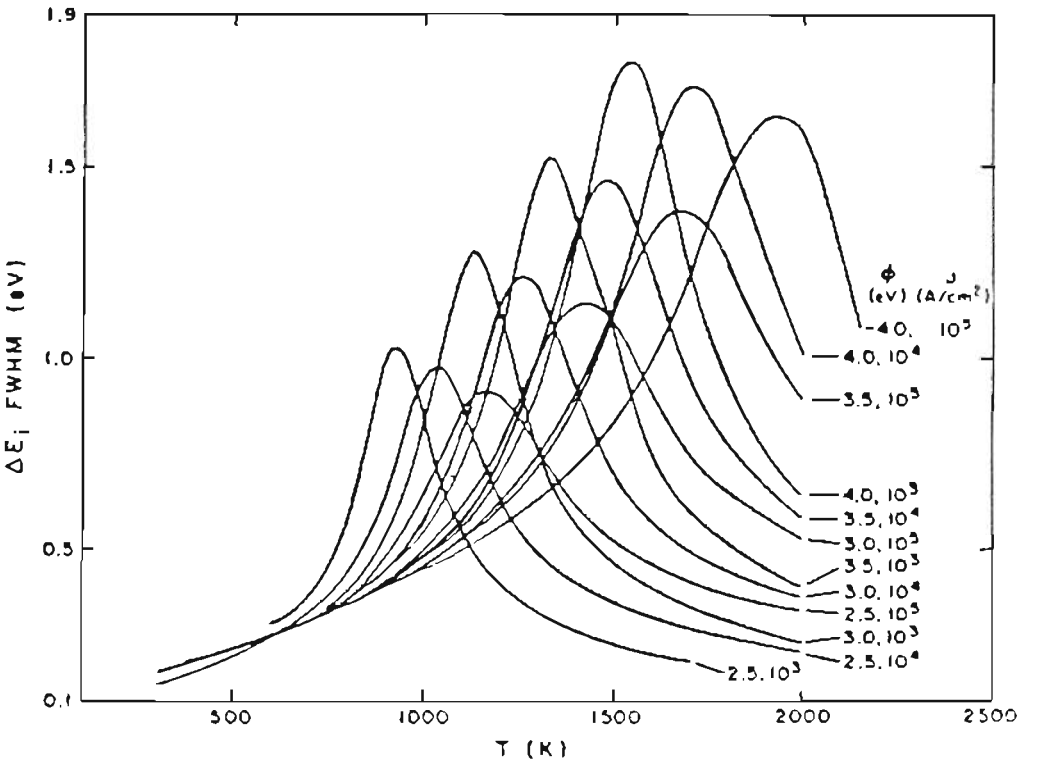

Fig.3-1 : Calculated values of the full width at half maximum of the total energy distribution curves as a function of temperature The plots are given for the indicated values of work function Φ and current density J

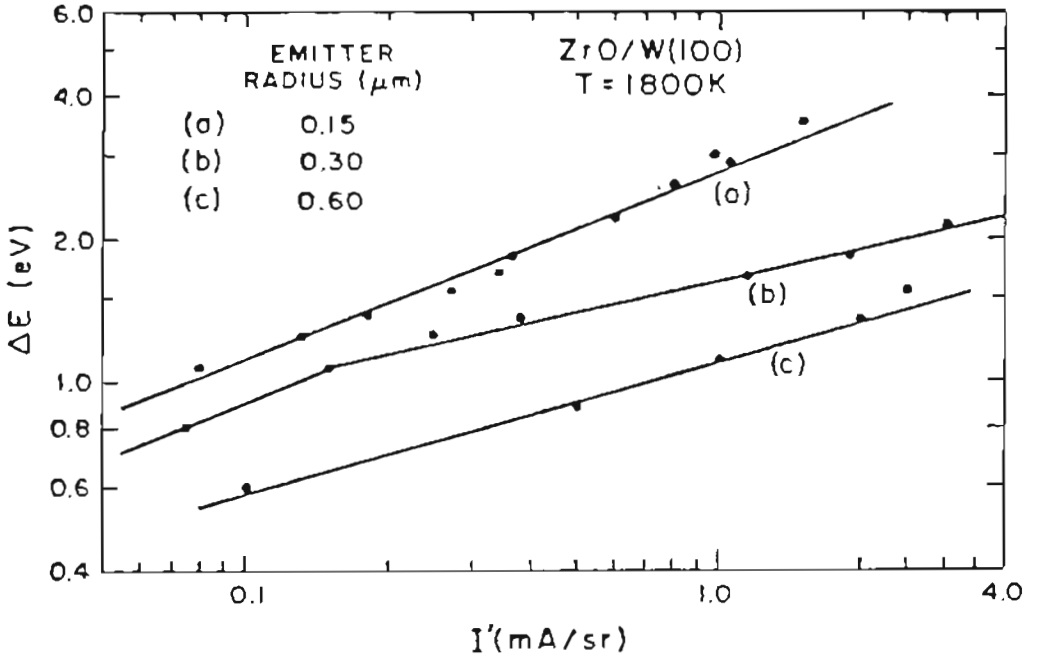

Fig.3-2 : Experimental values of the full width at half maximum of the energy spread ΔE versus angular intensity I' . The results are given for three values of emitter radius.

For tungsten γ=2900 dyne/cm and r is the radius of emitter (in cm). Fig.3-3 is an SEM photo of a W (100) built-up emitter. The built-up end form consists of a small spherical apex on a pyramidal structure with sides containing (100) faces and oriented along the <100> crystal direction. The pyramid can be viewed as being positioned on a large sphere of radius R as shown in Fig.3-4.

The basic mechanism which controls the mode of field build-up is the relative surface free energy of various exposed crystal faces on the emitter. The smallest carbon contamination, which is almost unavoidably present with operation at tip temperatures in excess of 1200 K, but below the temperature for thermal desorption of carbon, appears to preferentially lower the surface free energy of the (100) planes, but the presence of an oxide layer, observed with tip temperature below 1950 K, appears to preferentially increase the surface free energy in the (100) planes over that of the (112) and (310) planes, thereby promoting <100> build-up. Meanwhile, the oxide layer will remove the carbon impurities by forming the stable molecule carbon monoxide which desorbs from the surface at 1400 K, thus, enhancing the <100> build-up also. This is one reason to use oxygen processing[37] in field built-up emitter formation.

The "built-up" emitter is made by the following method: A tungsten wire (0.125 mm. dia.) is triple-pass zone refined in the (100) directions and is spot welded to a 0.25 mm tungsten filament. The end of the wire is then electrochemically etched to the desired radius[1,15]. There are two types of end forms which depend on whether a DC or AC voltage is used in the etching process (Fig.3-5).

The <100> crystal direction is a desirable emission direction because of the fact that for the bcc crystal structure the <100> direction has the largest (90°) angular separation between adjacent crystallographic directions. Thus , if the <100> direction is along the axis of the emitter, the field is sufficiently low at the four 90°

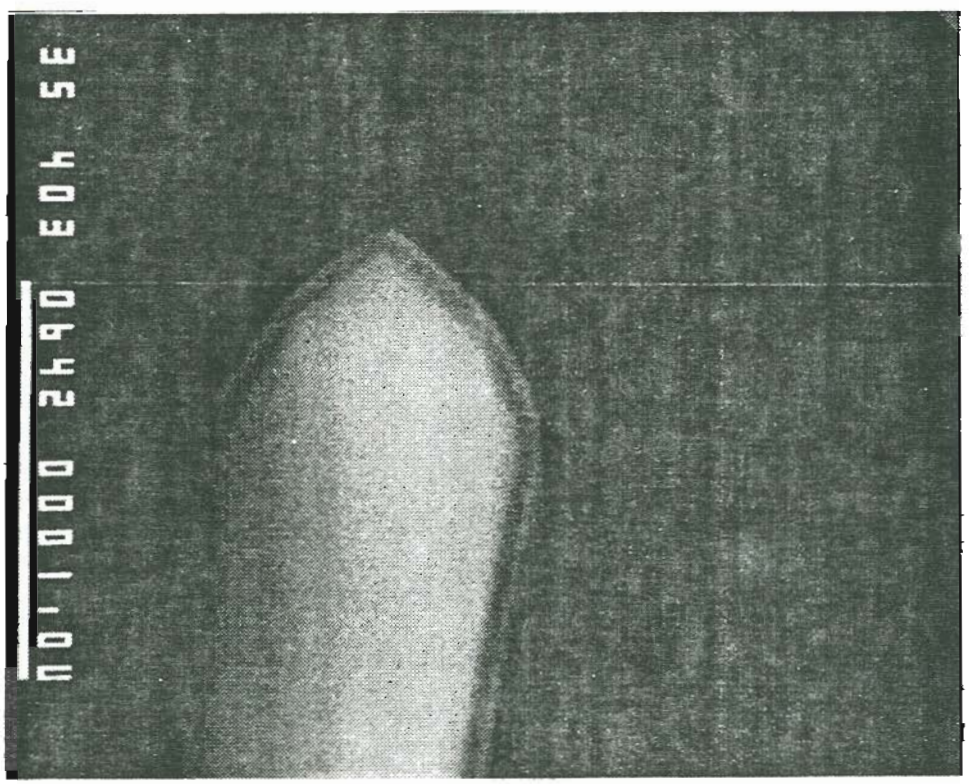

Fig.3-3 : The built-up emitter photo with <100> direction point apex after 1800K operation. Emitter radius is about 500Å.

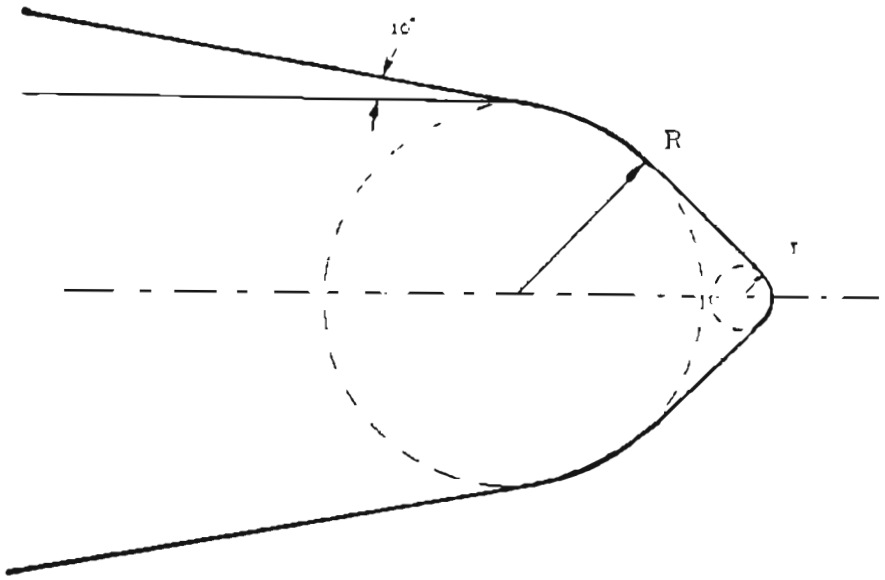

Fig.3-4 : The geometrical shape of the built-up emitter used in the SCWEM program.

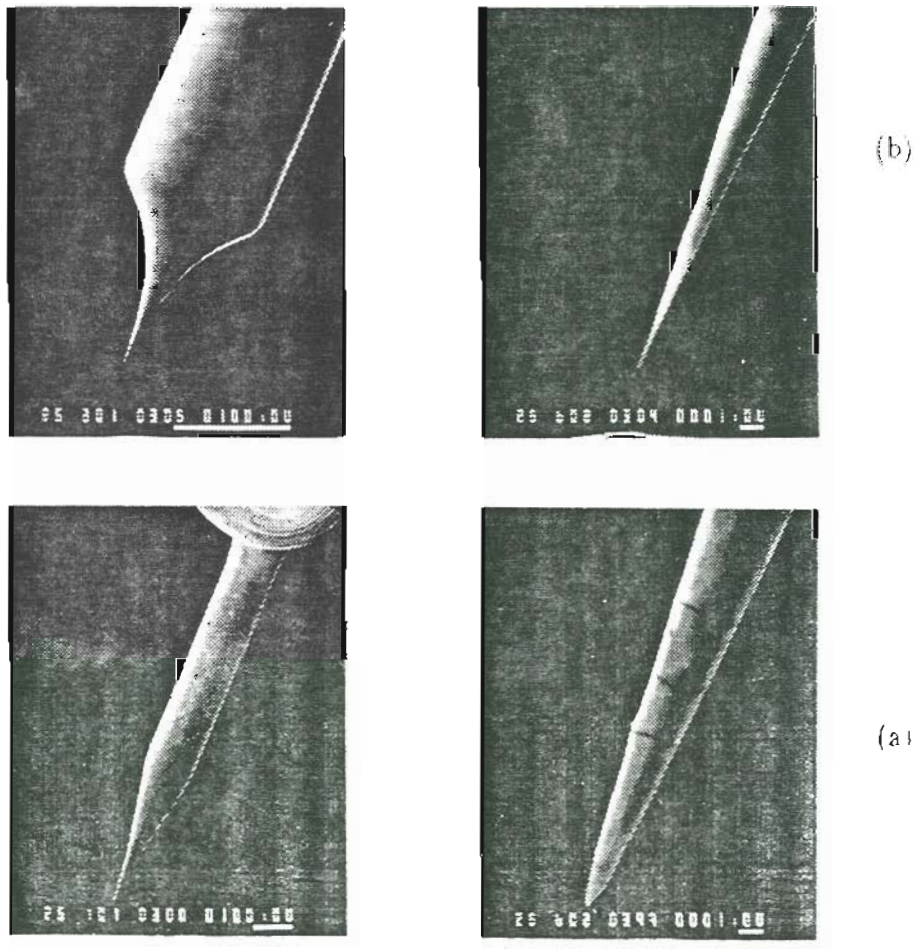

(b)

(a)

Fig.3-5 : Two types of W emitters: (a) DC etched emitter and magnified emitter tip. (b) AC etched emitter and magnified emitter tip.

displaced (100) crystal planes that negligible emission results from them. For example, the beam transmission is 3.0% for the (100) built-up emitter[16], but 0.51% for the cold (310) oriented emitter. which means that the angular confinement of the (100) built-up emitter is better. For the built-up emitter the beam angular confinement is about 18^{o} which greatly increases the current transmitted through a beam defining aperture.

As build-up proceeds, the emitter apex becomes smaller and total emission current increases due to field enhancement in accordance with the Fowler-Nordhiem equation. It is necessary to gradually reduce the field to hold the total current below a value at which catastrophic destructive vacuum arcing would occur.

At a background pressure of $\sim 10^{-8}$ torr the "built-up" emitter can operate continuously for hundreds of hours. However, for safety reasons we maintained a pressure $<1\times10^{-8}$torr in this study.

The thermal field ZrO/W emitter is a relatively dull (100) W emitter with a zirconium hydride ring attached to the emitter shank[17] (Fig.3-6). The emitter is heated to allow the zirconium to diffuse along the single crystal tungsten surface and form Zr-O complex in the presence of an oxygen partial pressure (10^{-6}torr) for about 48 hours[18]. Then, the emitter is put into the gun chamber to operate at 1800K under high field during which time a field induced thermal faceting takes place.

The emission pattern, which consists of a central bright spot surrounded by two or three concentric rings of emission, undergoes a cyclic variation. Fig.3-7 shows the sequence of the field electron pattern during emitter formation. The concentric ring structure is clearly shown for the zero field, thermal end form in photo (a). Upon application of the high voltage at T=1900K the two outer rings slowly disappear in

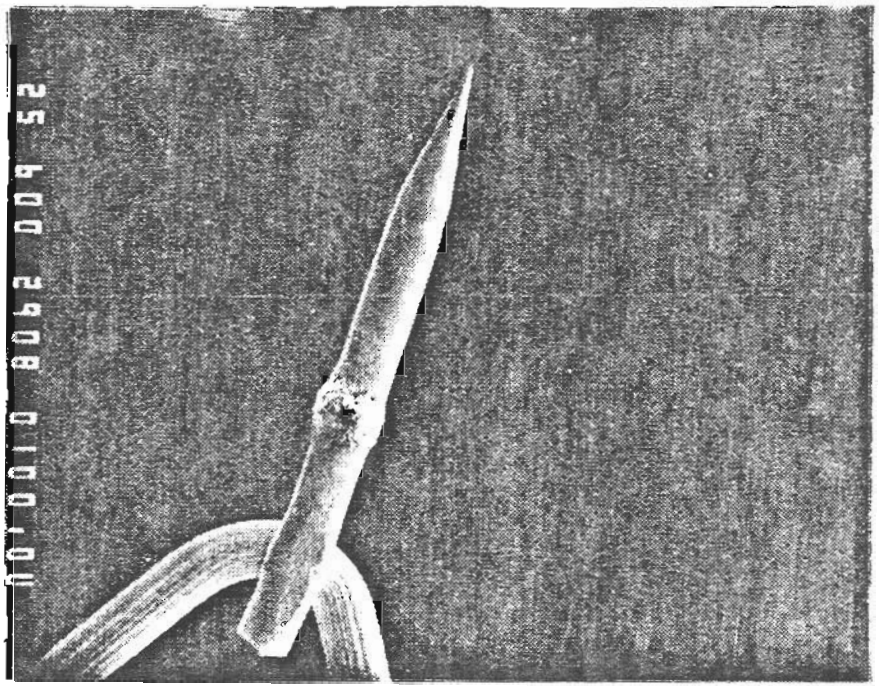

Fig.3-6 : ZrO/W (100) thermal field emitter showing zirconium on shank.

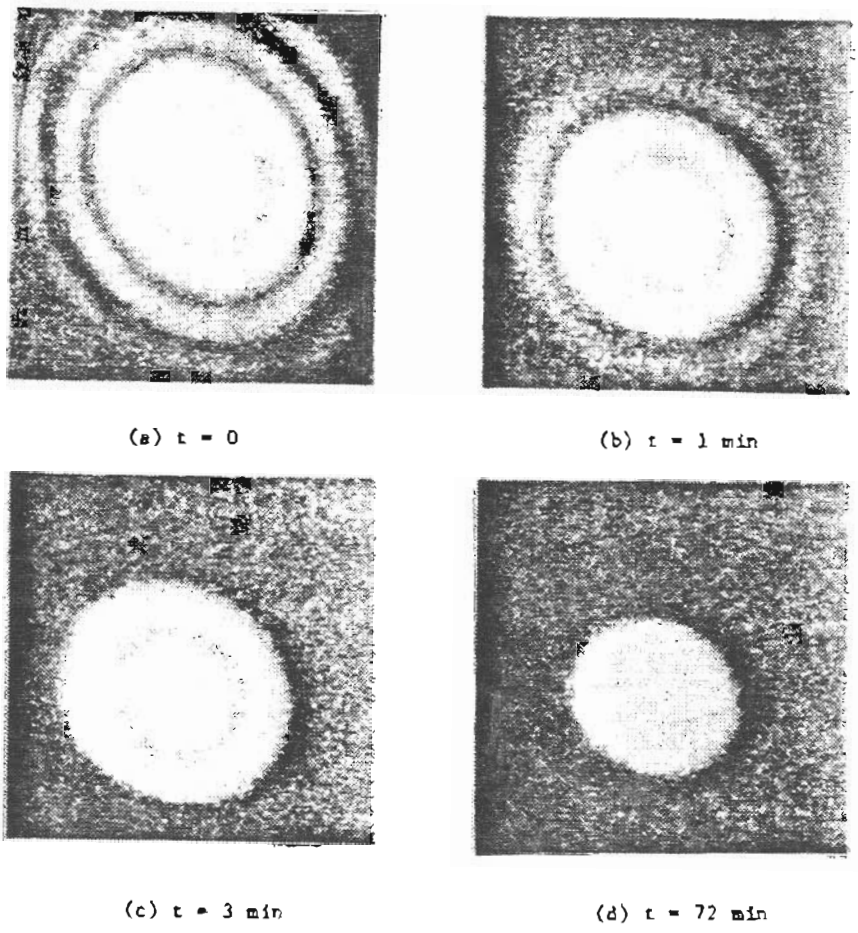

Fig.3-7 : Sequence of field electron patterns during faceting process of ZrO/W emitter operating at Y=1900K and V=5780V. Pattern (a) is the initial zero field, thermal emission. Patterns (b)(c) show the changes of concentric rings. Pattern (d) is the final bright spot.

photos (b)(c). The center bright disc of emission goes through several repetitive sequences of collapsing rings; finally, the single, bright emission spot shown in photo (d) is obtained and remains without further major change.

Fig.3-8 shows the anticipated geometric shape of the emitter that correlates with the Fig.3-7 emission contribution. Fig.3-9 shows the step shape of the emitter apex in a SEM photo. The process occurs by the outward diffusion of the surface atoms from the edge of each net plane; eventually, the final stable facet plane is achieved.

Fig.3-10 shows the end form of ZrO/W emitter before and after faceting. Fig.3-11 shows the orthogonal views at 60° tilt. The square facet plane is normal to the <100> emission direction. Previous considerations of the theoretical geometry of the final facet plane[38] have shown that the half diagonal b of the facet plane is related to the emitter radius r by

$$b = 0.268\, r \tag{3-4}$$

Examination of several micrographs, such as Fig.3-11, has given an experimental value of $b = 0.30\, r$. Based on these SEM photos and analysis, the end form of the ZrO/W emitter is shown in Fig.3-12.

That bulk diffusion of a ZrO complex readily occurs in tungsten can be explained qualitatively by a consideration of atomic radii[19]. The atomic diameter of the zirconium atom ($\approx 3.2\mathring{A}$) is approximately equal to the lattice spacing of W (100) surface ($3.16\mathring{A}$), thus, the diffusion of pure zirconium is negligible due to its relatively large atomic diameter. However, the Zr-O bond is largely ionic according to analysis using Pauling's correlation of electronegativity with ionic character of a bond. The ionic character of bond provides two important advantages. First, it reduces the size of zirconium atom, as indicated in Fig.3-13, so the zirconium and oxygen atoms

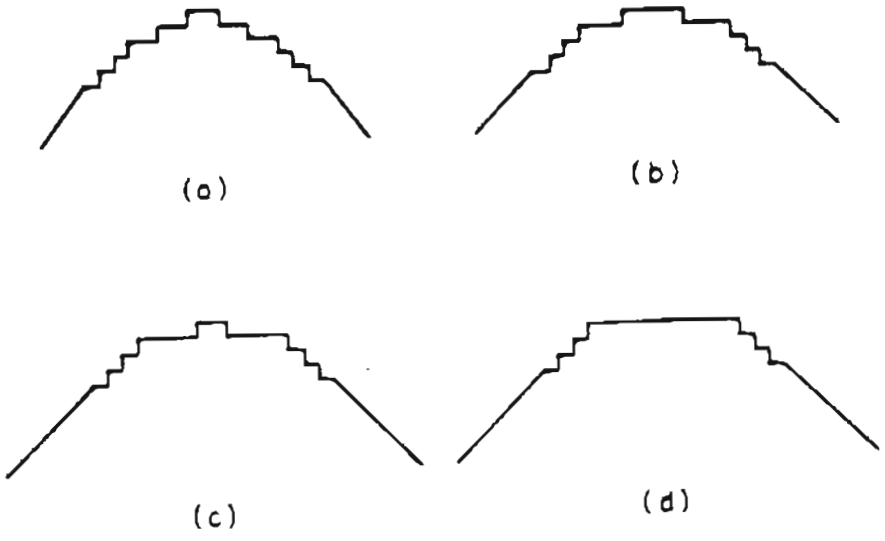

Fig 3-8 : Schematic of arrangement of (100) net plane during faceting where (a)(b)(c)(d) correlate with Fig 3-7 emission distribution (a)(b)(c)(d) .

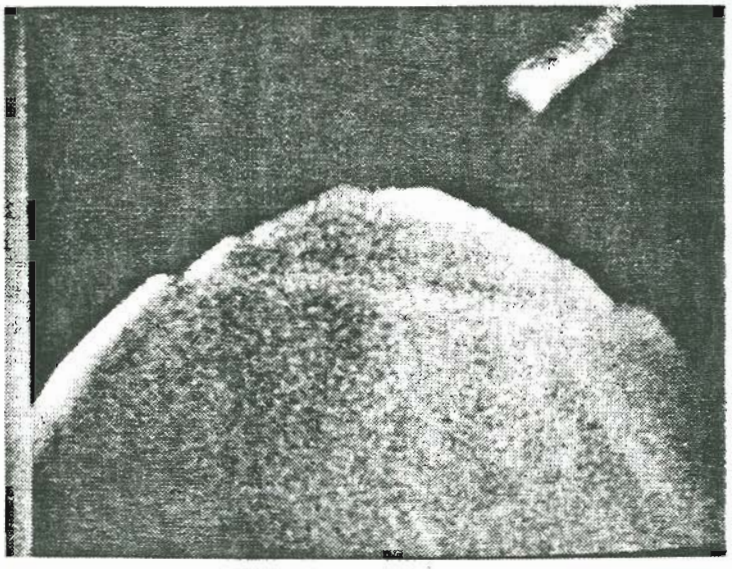

Fig.3-9 : Micrograph of ZrO/W emitter showing the step shape at the emitter apex during faceting

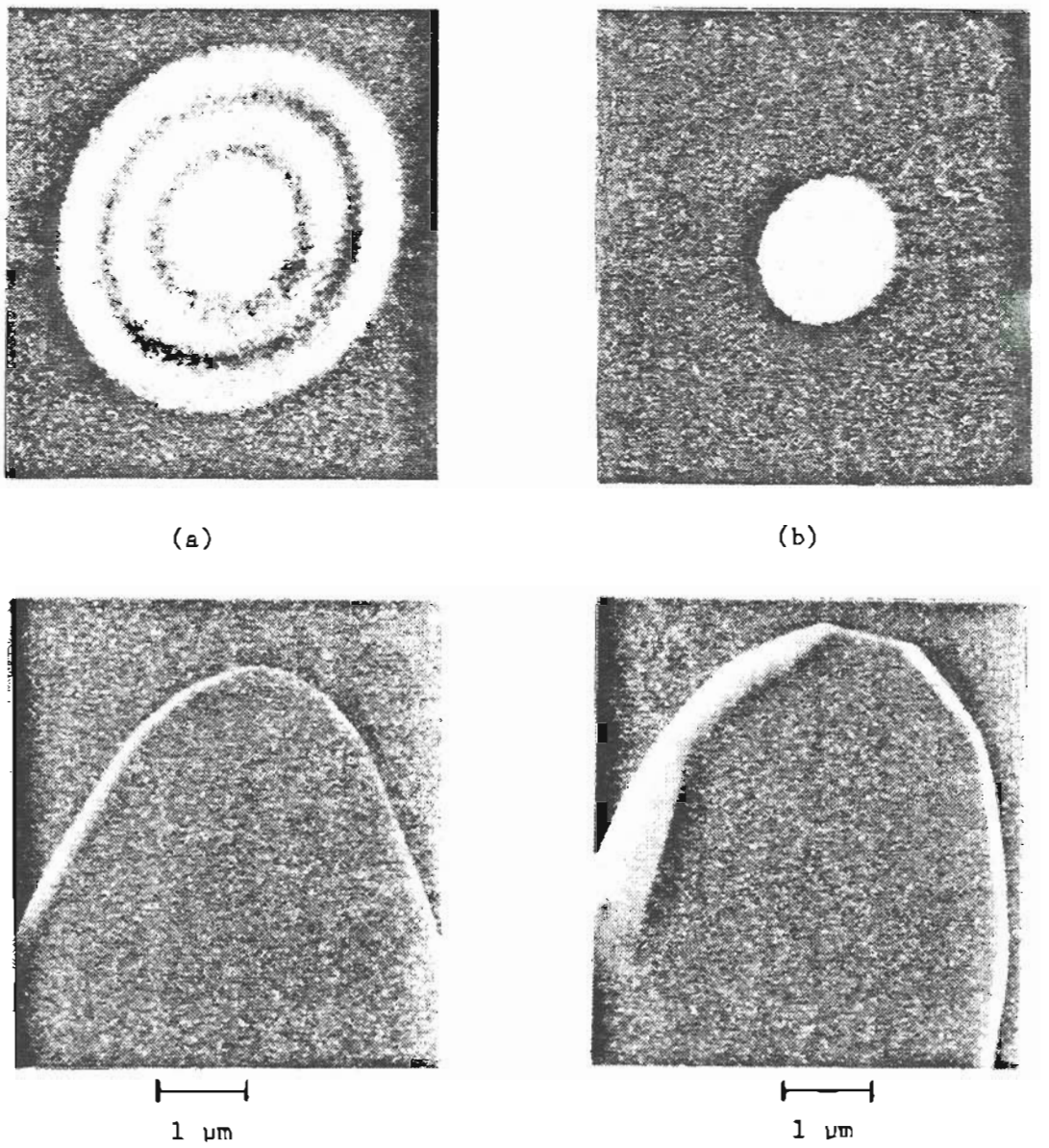

Fig.3-10 : Micrographs and field electron pattern (a) before and (b) after faceting

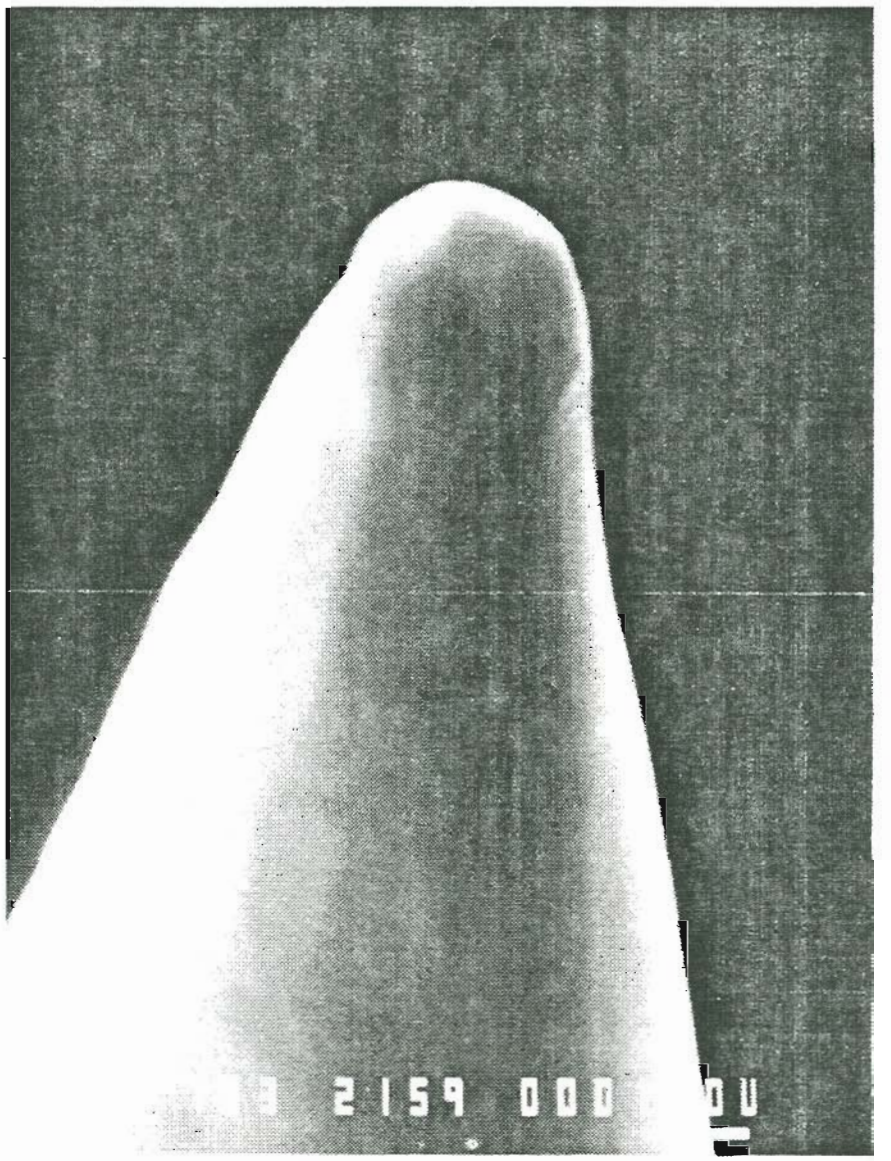

Fig.3-11 : Micrograph of ZrO/W emitter tilted 60^0 from SEM axis showing the end facet.

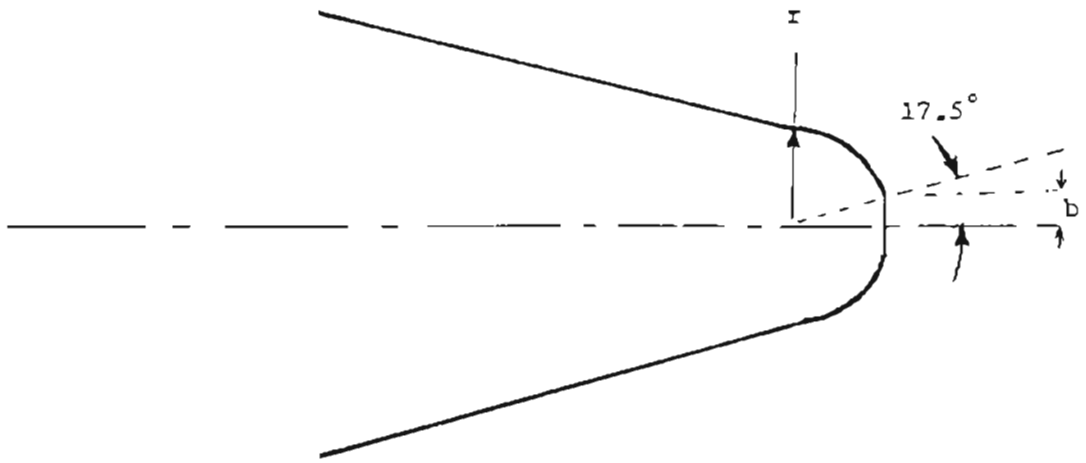

Fig.3-12 : The geometrical shape of the ZrO/W emitter used in SCWIM program

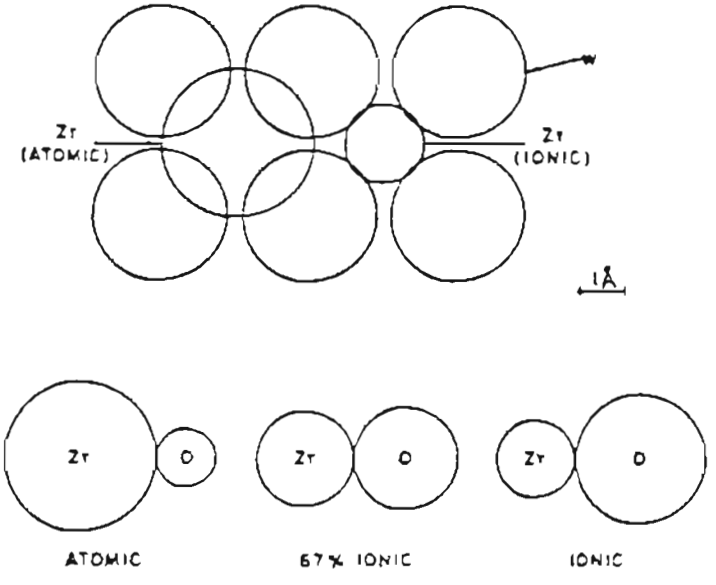

Fig 3-11 : Diagram showing the relative ionic, atomic and partial ionic diameters of zirconium and oxygen. Adsorption of both atomic and ionic zirconium on the 4-fold W(100) sites are depicted.

diffuse through the tungsten lattice with relative ease[14]. Second, the electronegative oxygen atom has an atomic radius of roughly $1.2\mathring{A}$, thus allowing it, on the basis of a hard sphere approximation, to be adsorbed in the voids on a (100) plane of tungsten. Evidently it is positioned below the zirconium atom with sufficient orbital overlap that the resultant dipole moment (Zr-W-O) is larger than dipole moment (Zr-W), so it enhances the work function lowering according to the Helmholtz equation, which relates the work function change $\Delta\phi$ to adsorbate coverage σ and dipole moment μ,

$$\Delta\phi = g\ \pi\ \mu\ \sigma \tag{3-5}$$

where g is a constant varying from 2 to 4 and $\Delta\phi$ is the change in work function.

The work function is reduced to about 2.6eV from 4.7eV for the clean (100) plane. This dramatic and selective reduction results in an important advantage for the thermal ZrO/W field emitter. In the Fowler-Nordheim equation the dominant factor has the form: $\exp(-const.\ \phi^{3/2}/F)$. If the work function is reduced to 2.6eV the field required for a given current density will be 44% of that required for a work function of 4.7eV. Since the geometry factor, $\beta = F/V$, is inversely proportional to the emitter radius the low work function emitter's radius can be increased by a factor $(0.44)^{-1} = 2.3$ without reduction in current density at a given extraction voltage.

A large emitter radius r has three additional advantages. First, it is more rugged and resistant to transient voltage pulses that destroy emitters of smaller radii. Second, the larger emitter reduces the anomalously high beam energy spread observed at high emission current (see Fig.3-2). Third, the larger emitter improves the noise/signal ratio because the averaging effect of larger emission area reduces current fluctuation. These advantages will be described in more detail in the following sections.

Chapter 4

Experimental approach

4.1 SEM Column

A modified CWIK-100 SEM as in Figs.4-1 and 4-2 has been used for all experiments. Briefly, the SEM was modified as follows:

An additional 20 l/s ion pump was added on the gun chamber and the sublimator pump was removed. A high current, high voltage power supply was built to handle the much higher emission current of the TF emitter and to supply the DC heating current and suppressor voltage. A newly designed gun assembly was installed which had a suppressor electrode to restrict the emission from emitter shank as in Fig.4-3. Two more apertures were added on the column, one variable aperture with radii 76.2, 152.4 and 203 μm, was located just below the electrostatic lens, and another fixed aperture with radius 0.5mm was inserted above the gun chamber isolation valve to differentiate the vacuum pressure in the column. Two wobbler circuits were added to the stigmator and beam deflection voltage supplies to aid in beam alignment. A heating and timing device was built for periodically baking the gun chamber and ion pump during initial evacuation. After these modifications the column performed quite well with the TF electron sources used in this study.

Although the electron optical system (in Fig.4-2), which uses a two-element immersion lens, was not designed for use as a deceleration system, there is a range of extraction voltage V_E to beam voltage V_B ratios where reasonably good resolution

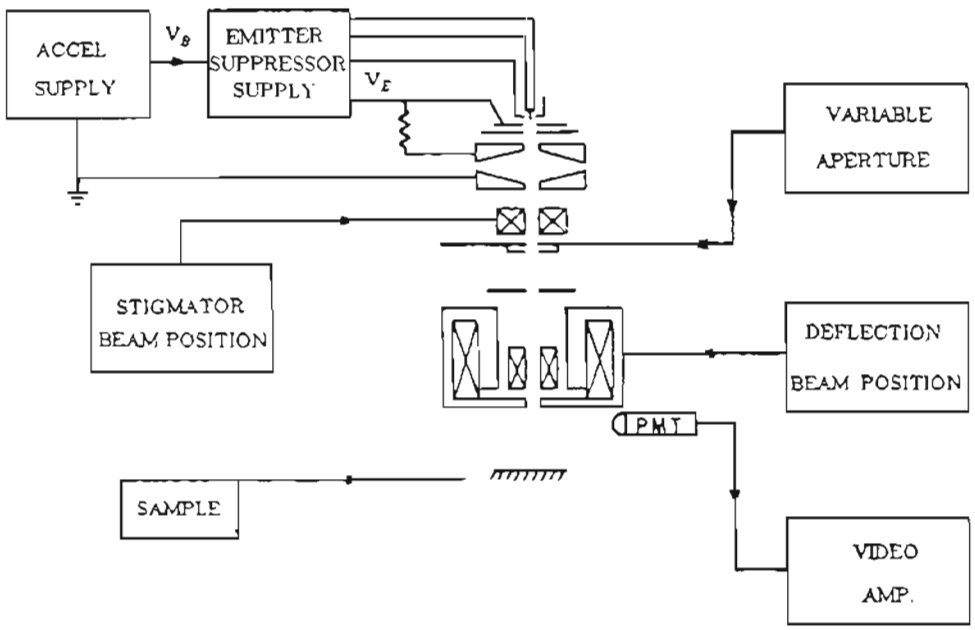

Fig.4-1 : A modified SEM column. Mainly, one suppressor, one varying aperture, one fixed aperture and one more ion pump(not indicated) were installed.

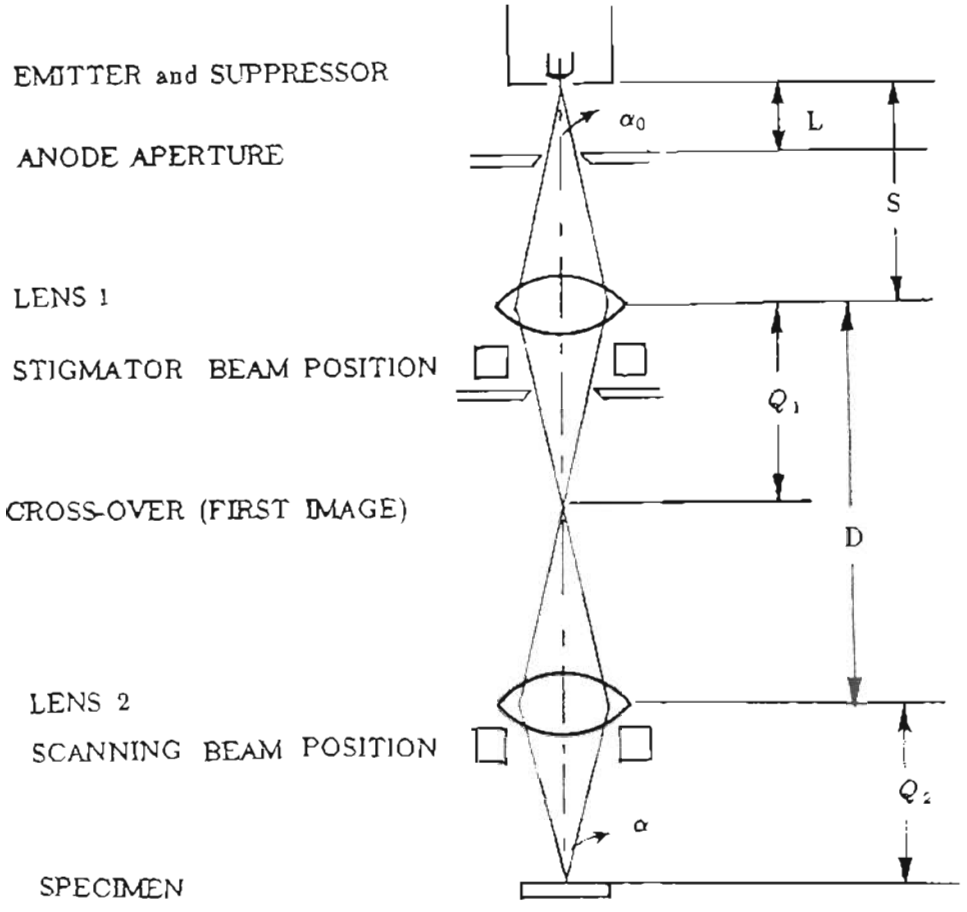

Fig.4-2 : Schematic diagram of the SEM column and calculation parameters L represents the distance between the initial aperture and emitter, S the object distance, Q_1 the image distance of the first lens, D the fixed length between the two lenses, Q_2 the final image distance. All these are used to calculate the column optical properties.

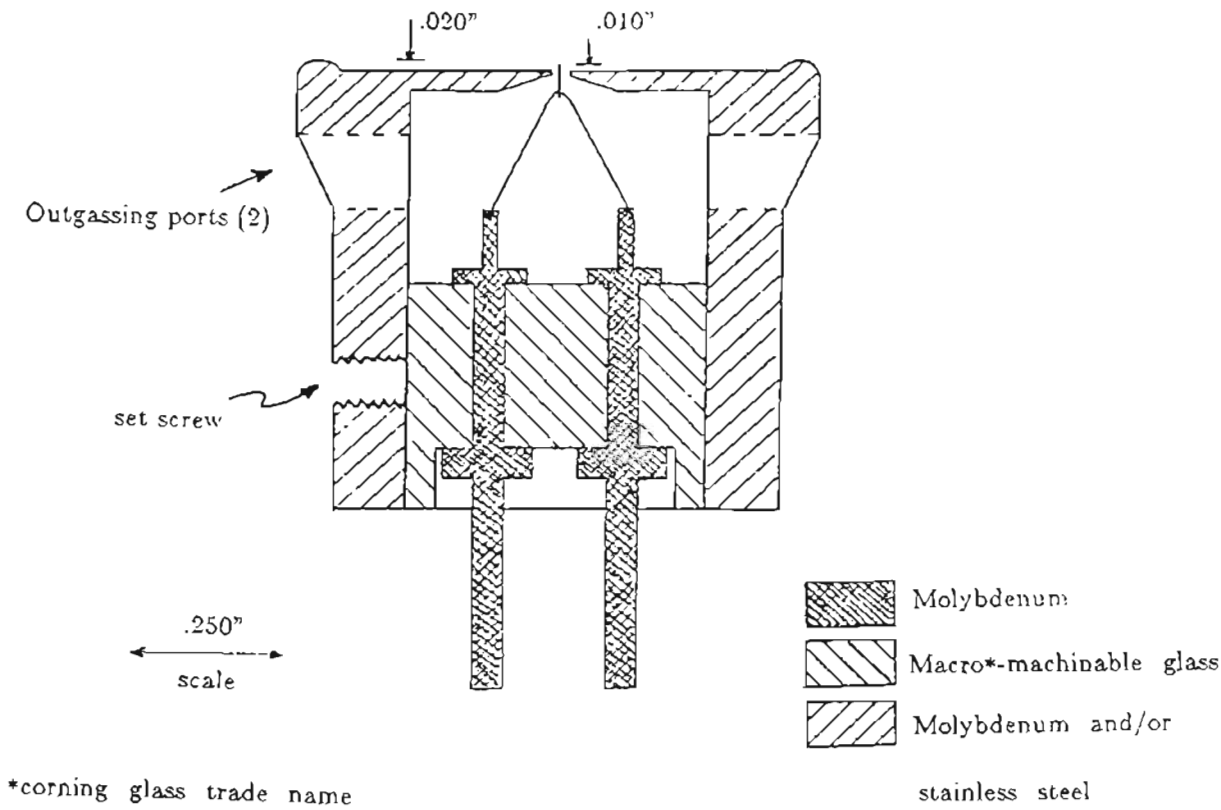

Fig 4-3 : Emitter and suppressor assembly

could be attained. This will be discussed in detail below.

The emitter temperature was controlled by the filament current and measured by a "Micro Optical Pyrometer" through a side port containing a window. The gun chamber pressure was measured by a "Granville-Phillips" gauge controller. The differential aperture mentioned above kept the gun chamber pressure two orders of magnitude lower than the specimen chamber. The suppressor and ion pump in the gun chamber sometimes required "High-Potting" which involves the use of high reversed voltage to desorb the contamination.

4.2 Focused beam size measurements

The method used to evaluate the beam spot size involved the measurement of the rise time of the beam current $I_P(t)$ when swept across a knife edge. If one assumes a Gaussian current distribution exists, the most convenient way is to measure the full width at half maximum (FWHM) of the peak of the Gaussian density function, which can be obtained from the derivative of the front edge of the $I_P(t)$ plot as the beam is scanned across the knife edge.

In our experiment a 125μm square hole etched in a single crystal silicon chip and coated with gold was used as the knife edge. A positively biased Faraday cup made of molybdenum was positioned below the hole to collect the incoming transmitted beam current.

In most cases, the FWHM method and the distance between 10 and 90% amplitude points on the waveform measurement as shown in Fig.4-4 gave a good agreement. But, on occasions these two methods disagreed because the assumed Gaussian current distribution was seriously deformed with long tails. One explanation for the

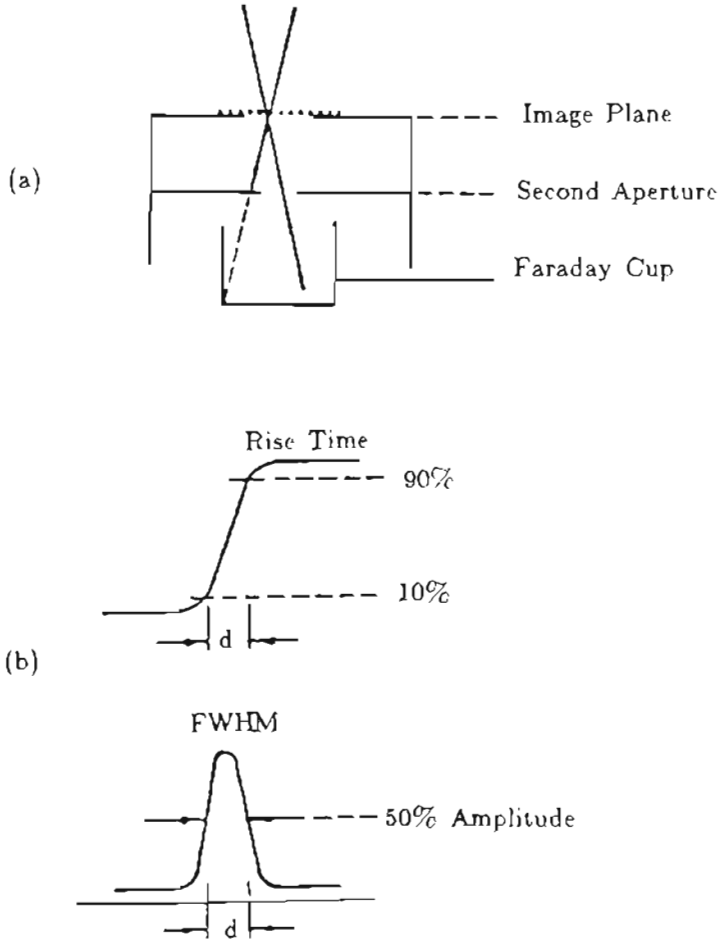

Fig.4-4 : (a) Beam spot size measurement device. (b) spot size measurement conventions: Rise Time and FWHM methods

non-Gaussian current distribution is due to the interplay of the non-Gaussian energy distribution and chromatically aberrated beam[20]. The energy distribution varies for the different kinds of emission, e.g. TF, Schottky and CF. When the lens system's aberrations are mainly chromatic, the electrons with different energies will cross the optical axis at different positions, $Z_0+\Delta Z$, instead of one focus point Z_0. The shift distance is

$$\Delta Z = C_C \frac{\Delta E}{E} \tag{4-1}$$

where ΔE is the energy spread of emitted electrons. It means that the image plane current distribution depends on the Z position of the image and is only Gaussian when the TED is Gaussian.

4.3 Beam current fluctuation measurements

The current fluctuation measurements were made with a HP-5423 Dynamic Signal Analyzer with a frequency band width from 0.8Hz to 25.5k Hz. The frequency resolution automatically varied from 0.016mHz to 100Hz with band-width selection.

In order to measure the low frequency noise components in the beam current for ZrO/W emitter it was necessary to cancel the D.C. component in the beam. For this we used a very stable DC reference voltage generator with thermal compensation shown in Fig.4-5. Some low frequency measurements required more than ten hours.

We found it necessary to break the 25kHz range into several (e.g. 8) band-widths to make measurement for the optimum sensitivity in every band, and in order to have a smoothly connected power spectrum density curve. Such results were quite different from a curve measured in only one large band-width (e.g. 0 to 25kHz). Because the frequency resolution is poor for a large frequency range , e.g. 100Hz resolution for a 25kHz range, detail is lost at the low frequencies, which is an important

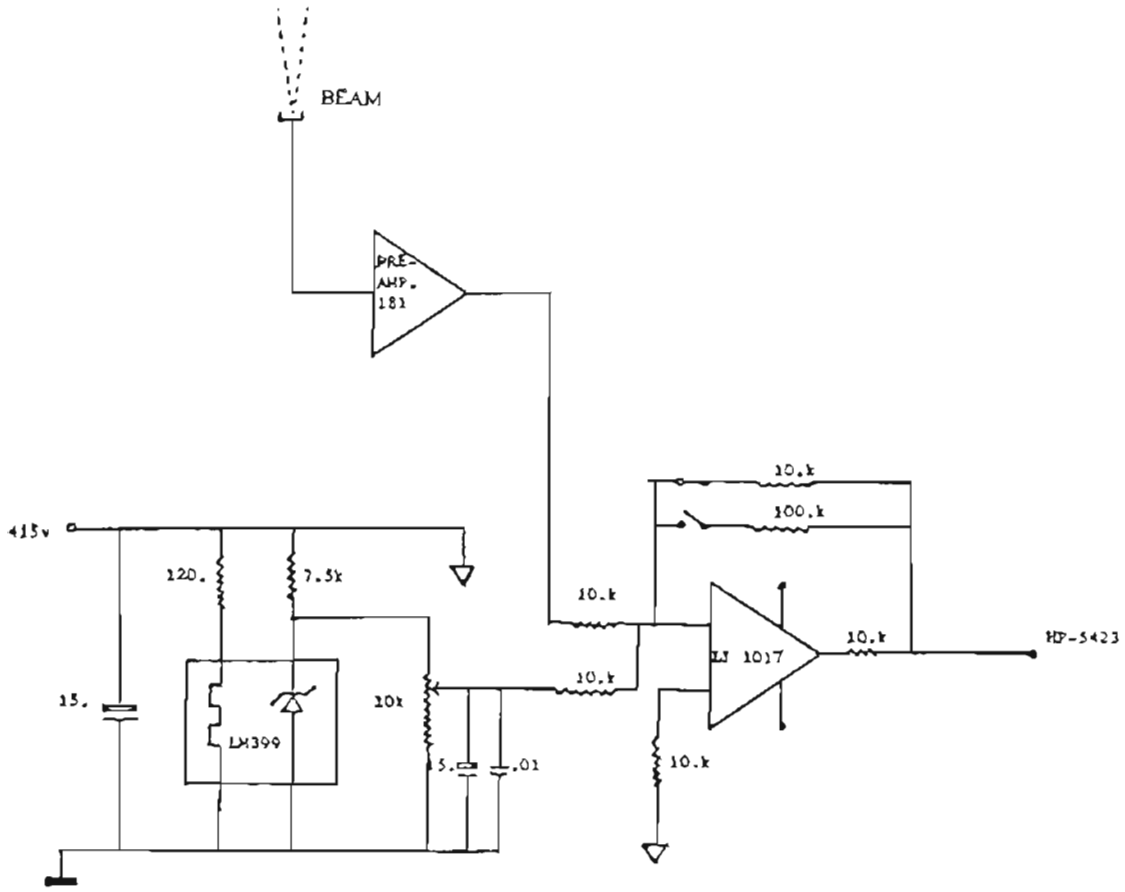

Fig.4-5 : Circuit for canceling the DC component from beam current in the measurement of noise power spectrum.

part of the noise spectrum. Each measurement included an average of about 60 to 100 samples. The results were stored in HP-5423 magnetic tapes and then via HP Interface Bus entered into a computer. Eventually, the power spectrum was plotted and integrated to obtain the current fluctuation.

Chapter 5

Experimental results and discussion

5.1 Beam spot size

The predicted value of the focused beam size d was calculated according to

$$d = \left[(0.5 C_S^t \alpha_0^3)^2 + (C_C^t \alpha_0 \Delta V / V)^2 + d_d^2 + d_v^2\right]^{1/2} M_t \qquad \text{(mm)} \qquad (5\text{-}1)$$

where C_S^t and C_C^t represent the total spherical and chromatic aberration coefficients respectively, the diffraction aberration term $d_d = 14.9694 \times 10^{-7}/(V^{1/2}\alpha)$ (mm), the virtual source size $d_v = 200\,\text{Å}$, the total magnification is M_t and the initial aperture angle is α_0. For a two lens system C_S^t and C_C^t are given by[24]

$$C_{So}^t = \frac{C_{S1}^{(1)}}{M_1^4 \left(\frac{V_i^{(1)}}{V_o^{(1)}}\right)^{3/2}} + \frac{M_2^4}{M_t^4} \left(\frac{V_o^{(1)}}{V_o^{(2)}}\right)^{3/2} C_{So}^{(2)} \qquad (5\text{-}2)$$

$$C_{Co}^t = \frac{C_{C1}^{(1)}}{M_1^2 \left(\frac{V_i^{(1)}}{V_o^{(1)}}\right)^{3/2}} + \frac{M_2^2}{M_t^2} \left(\frac{V_o^{(1)}}{V_o^{(2)}}\right)^{3/2} C_{Co}^{(2)} \qquad (5\text{-}3)$$

where $M_t = M_1 M_2$, the superscripts (1) and (2) represent the lens number 1 or 2, subscripts s and c represent spherical and chromatic, i and o represent image side and object side of the lenses.

To calculate C_C, C_S and M, a program using finite element method written by Munro[18] was used. The ray path and parameters are shown in Fig.4-2 where the object distance S, the final image length Q_2 and the distance between two lenses D, are kept

constant as 43mm, 30mm, and 144mm respectively. According to the lens geometry and operating voltage the individual aberration coefficients, C_{Si}^1, C_{Ci}^1, C_{So}^2 and C_{Co}^2 can be calculated, then Eq.(5-2) and (5-3) are used to obtain the total aberration coefficients, C_{So}^I and C_{Co}^I.

The shapes shown in Figs.3-4 and 3-12 were used in the SCWIM computer program. The structure of field emission guns may vary. Among them, a triode-type gun of Fig.5-1 is common and was used in this study.

The focused beam size was measured for several different cases of the beam voltage ratio V_B/V_E. Usually the low beam voltage was the case of main interest, say $V_B/V_E < 1.0$. The spot sizes vary drastically with V_B/V_E. For the (100) ZrO/W emitter typical results are shown in Fig.5-2, where the dotted line is experimental data and the solid line represents the theoretical data based on Eq.5-1 where d_g=200A and ΔV=.8eV.

From Fig.5-2 one can see that good agreement exists between experiment and prediction except for the voltage ratio range 0.15 to 0.4. This discrepancy persisted throughout all measurements using various emitter sizes. A possible explanation for the Fig.5-2 discrepancy might be that the value of ΔV=1.0eV is too small even though from the experimental values of ΔV given in Fig.3-2, the latter value of ΔV, if anything is too large for the experimental values of emitter radius and I' . This analysis can be carried further by examining the region where the chromatic aberration term d_C in Eq.(5-1) makes the dominant contribution to d. Fig.5-3 shows that d_C does in fact become the dominant contribution in the voltage ratio 0.15 to 0.3 which is the range where the Fig.5-2 discrepancy occurs.

In order to investigate the possibility of a chromatic aberration origin to the above mentioned discrepancy experiments, with two other ZrO/W emitters were

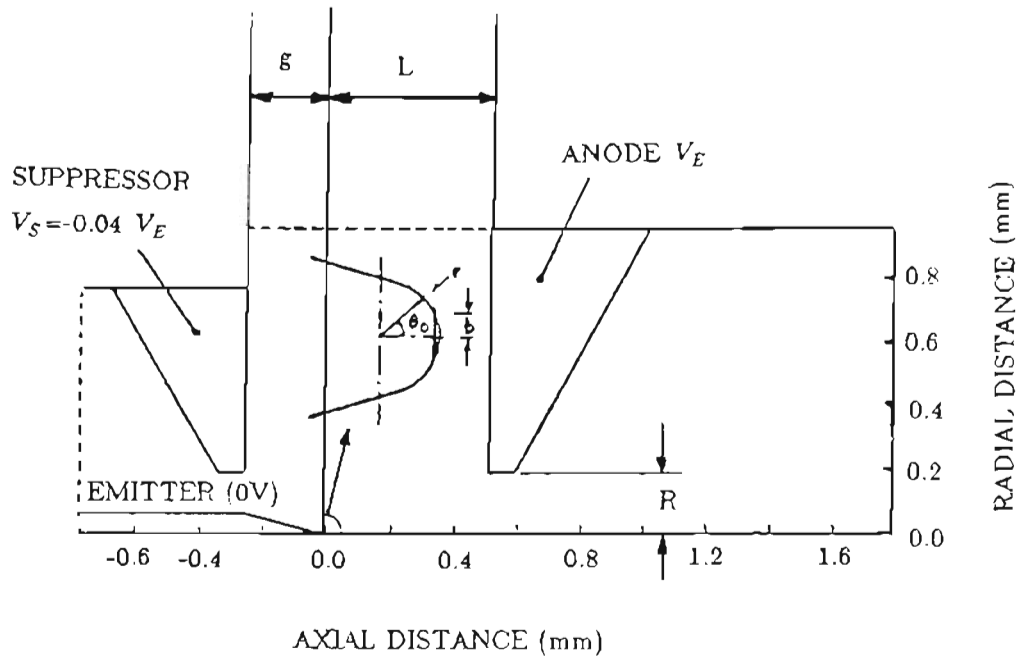

Fig.5-1 : Diagram of electrode configuration used in the gun structure analyzed in this study. Insert shows an expanded view of the emitter apex for the round and faceted cases with radius r. The flat radius is b, the launch angle for electron trajectories is $\theta_0 = 17.5^\circ$.

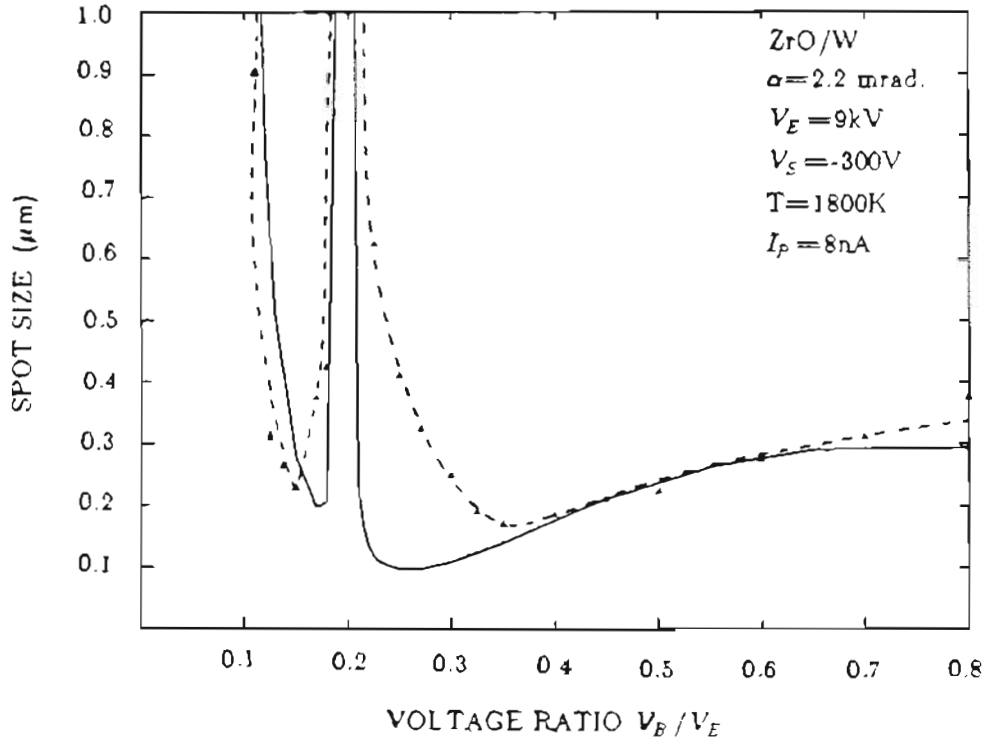

Fig.5-2 : Beam spot size versus voltage ratio in range $V_B / V_E < 8$

The broken line is experimental and solid line is theoretical curve for ZrO/W emitter. Source radius and angular intensity were 1 μm and 0.53 mA/sr respectively. Value of $\Delta V = .8$ eV was assumed

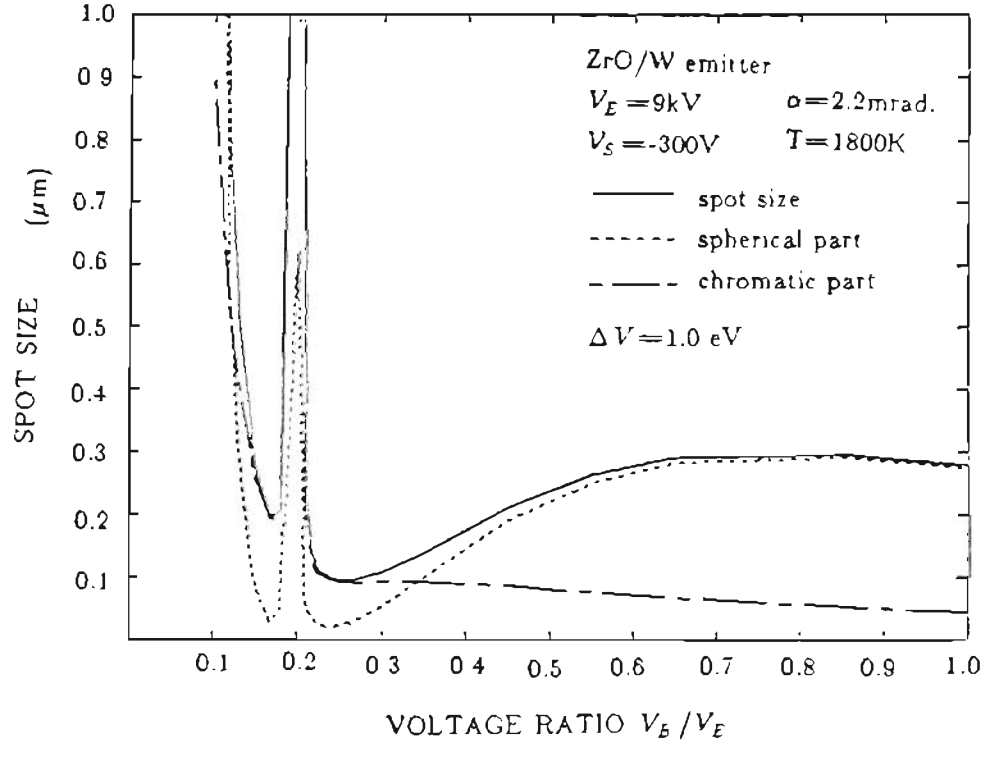

Fig.5-3 : Curves show the calculated relative contributions of spherical and chromatic aberrations to the beam size.

carried out in the column. In these experiments d was carefully measured as a function of I' at the voltage ratio V_B/V_E=0.4 and α_o=0.8mrad (see Fig.5-4), which means that chromatic was the only meaningful aberration (for r=0.35μm, ΔV=1eV and V_e=5.3kV, from Eq.(5-1) d_C=500Å; for r=0.8μm, ΔV=0.77eV and V_E=7.3kV, from Eq.(5-1) d_C=350Å). Thus, for I' <.2mA/sr both emitters show close good agreement to the predicted d using reasonable values of ΔV.

In Fig.5-5 the Fig.5-4 data for the r=.35μm emitter has been used in conjunction with Eq.(5-1) to calculate a value of ΔV. At I' =1mA/sr the Fig.5-4 data yields a predicted value of ΔV=3.2eV. If we examine the experimental V(I') results in Fig.3-2 we see that the value ΔV can not exceed 1.5eV for this this condition. Based on the Fig.3-2 results we expect that a larger ΔV for a specific value of I' for the smaller radius emitter; thus we expect a difference in ΔV can explain the difference in the two Fig.5-4 curves but not the absolute magnitudes of ΔV.

A similar result was also obtained for the built-up emitter results as shown in Fig.5-6 where the experimental d versus voltage ratio results are compared with the Eq.(5-1) predictions using three values of ΔV. From previous measurements[13] of ΔV for the built-up emitter we conclude that for the value of I' used in the Fig.5-6 results it is unlikely that ΔV>2.eV. Again we see a similar discrepancy between experimental and predicted results as was observed for the ZrO/W emitter.

Thus we must conclude that, although for I' <.2mA/sr Eq.(5-1) appears to agree with experimentally measured values of d at a voltage ratio of 0.4 using experimentally obtained values for ΔV, nevertheless for larger values of I' this agreement seriously breaks down. We must therefore look for an answer elsewhere than the d_C term in Eq.(5-1).

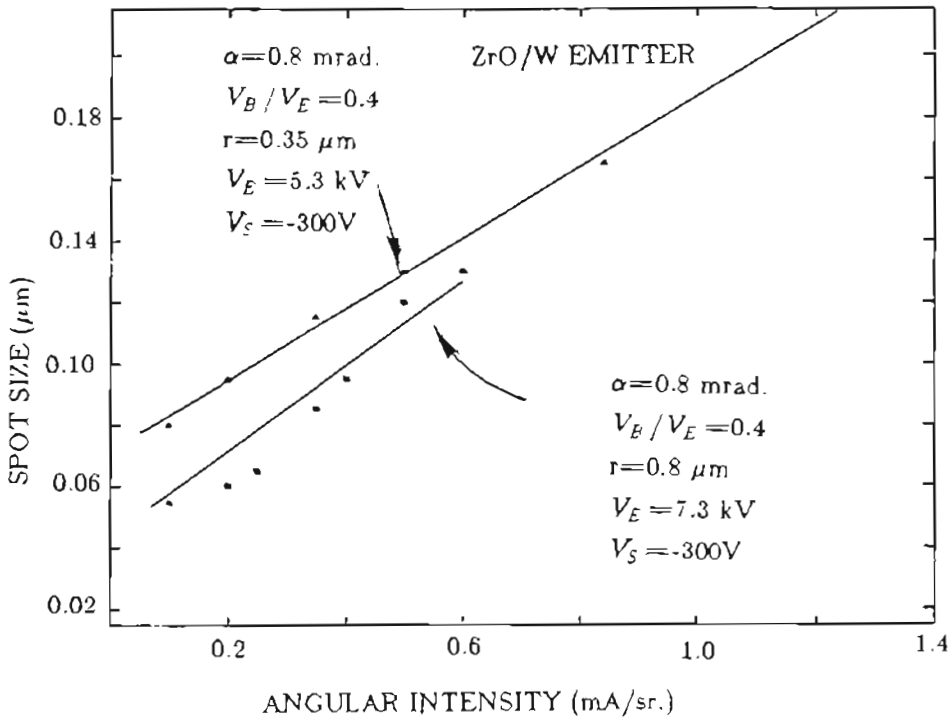

Fig.5-4 : The effect of measured angular current intensity I' upon spot size for the ZrO/W emitter with radii r=0.35 and r=0.8 μm I' was varied by adjusting V_S.

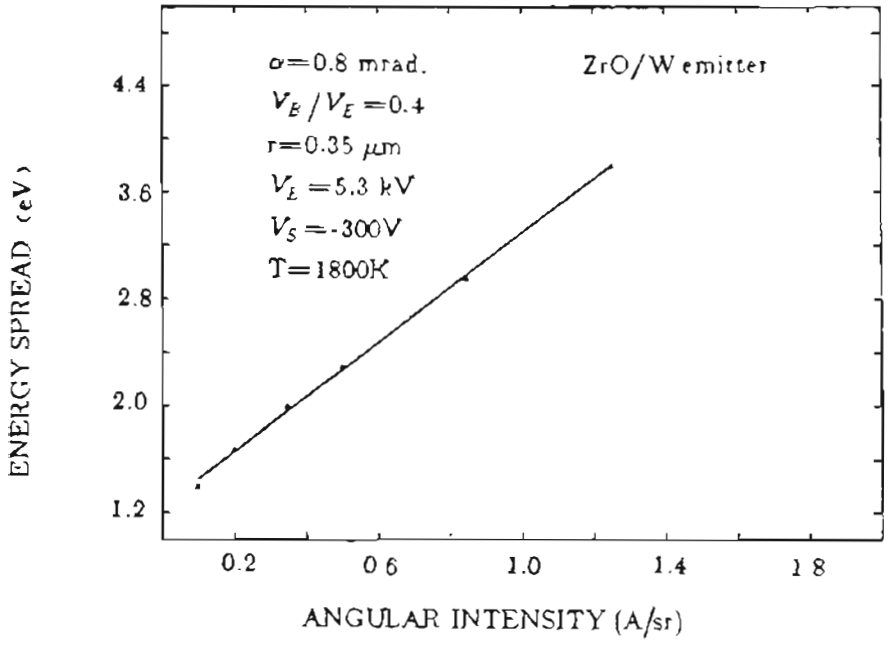

Fig.5-5 : The calculated energy spread ΔV versus the angular intensity I' according to Eq.(5-1) and data from Fig.5-4. It shows a linear relationship between ΔV and I' .

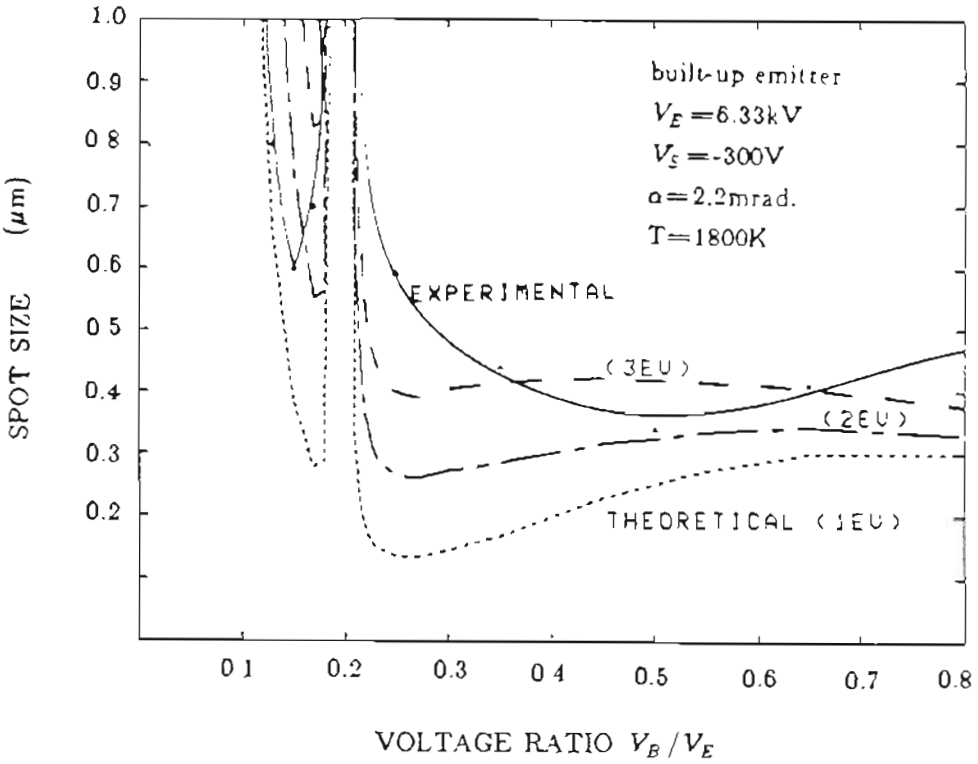

Fig.5-6 : Beam spot size versus voltage ratio for W (100) built-up emitter (solid line) and comparison with the theoretical calculations. The three dotted curves correspond to energy spread in values of 1eV, 2eV and 3eV. Source radius and angular intensity were 0.076μm and 0.66 mA/sr respectively.

As discussed below we believe that a contribution to d not heretofore considered, namely radial broadening, is the cause for the discrepancy observed above. Radial broadening due to stochastic Coulomb interactions during the electron flight path is well known in conventional thermionic source focusing columns when large beam currents are employed such as in shaped beam lithography systems. Groves, et al[39], were the first to show from a Monte-Carlo analysis that even in a single lens field emission column, when the beam current exceeds several hundred nA at 20kV, radial broadening of the focused beam spot occurs. The reason for the latter is that for field emission column the overall column linear magnification M typically is greater than 1. From the Lagrange-Helmholtz relation the angular magnification m is given by

$$m = \frac{1}{M}\left[\frac{V_E}{V_B}\right]^{1/2} = \frac{\alpha}{\alpha_o} \tag{5-4}$$

where α and α_o are the image and object side beam angles respectively. Thus with increasing value of M, m decreases for a fixed voltage ratio. Unfortunately, one of the intrinsic advantages of field emission columns, i.e., the small value of the image side α due to the large M which, in turn, leads to small deflection angles for a fixed scan field, will be shown to become a disadvantage if large beam currents are required at low voltages.

The Monte-Carlo investigation by Groves, et. al[39], was carried out for a single lens column of length Z_g, constant electron potential V_B and image side convergence angle α. The resultant expression obtained for the broadening of the focused spot in the image plane was

$$d_b = \frac{c\ Z_g\ I}{V_B^{3/2}\ \alpha} \tag{5-5}$$

where c is a constant. It is readily seen from Eq.(5-4) that for a fixed α_o the convergent angle α is directly proportional to m. In Fig.5-7 the values of both M and m for

the two lens column used in this study are plotted versus lens voltage ratio. At V_B/V_E=0.20 the value of m=0.08 whereas at V_B/V_E=0.15 and 0.35 the value of m are 4.34 and 5.25 respectively. Thus at V_B/V_E=0.20 the image side beam has a convergent half angle of 0.176mrad. thereby maximizing the contribution of d_b according to Eq.(5-5).

For $V_B/V_E>0.24$ no crossover occurs in the column. However, for $V_B/V_E<0.24$ a crossover is formed in the column as shown schematically schematically in Fig.4-2. According to an analytical result by Van Leeuwen and Jansen[42] the radial broadening at a crossover between two lenses is given by

$$d_b' = \frac{c' I^{1/2} Z_l^{2/3}}{V_B^{13/12} \alpha} \tag{5-6}$$

where c' is a constant and Z_l is the interlens distance. The Eq.(5-6) result is very similar to the empirical result given in Eq.(5-5) and , again, predicts a large radial broadening effect for low voltage beam with small α.

Using Eq.(5-5) for $V_B/V_E>0.20$ with Z_φ equated to the total column lengths and adding d_b in quadrature with Eq.(5-1) aberrations, modified theoretical curves describing the ZrO/W and built-up results are given in Figs.5-8 and 5-9. A value of c was chosen in each case to fit the curves at V_B/V_E=0.25. The experimental and modified theoretical curves are in good agreement with the inclusion of the radial broadening term in Eq.(5-1) for $V_B/V_E>0.20$. For $V_B/V_E<0.20$ a combination of Eqs.(5-5) and (5-6) was used where the lengths (see Fig.4-2) were $Z_\varphi = D - Q_1 + Q_2$ and $Z_l = D$. The value of c' in Eq.(5-6) is given by the following

$$c' = 0.0344 \frac{e^{1/12} m_e^{1/4}}{\epsilon_o^{5/6}} = 0.126 \tag{5-7}$$

where m_e is the electron mass and ϵ_o is the permittivity (MKS system used). In the

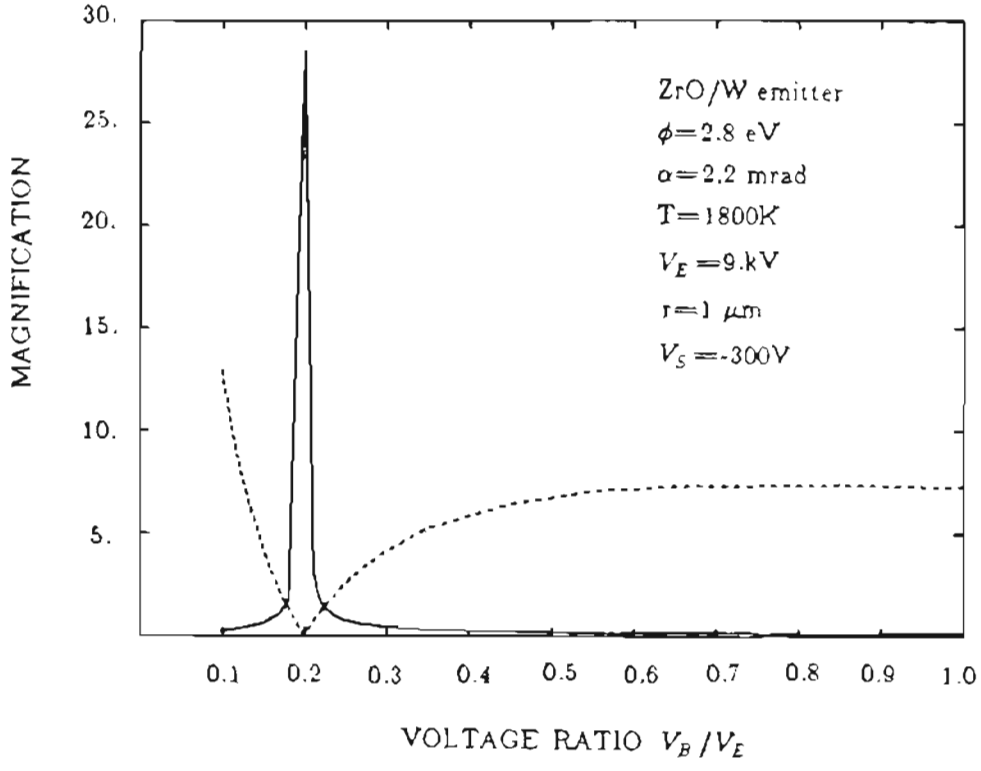

Fig 5-7 : The total magnification M (solid curve) and angular magnification m (dashed line) versus voltage ratio V_B / V_E .

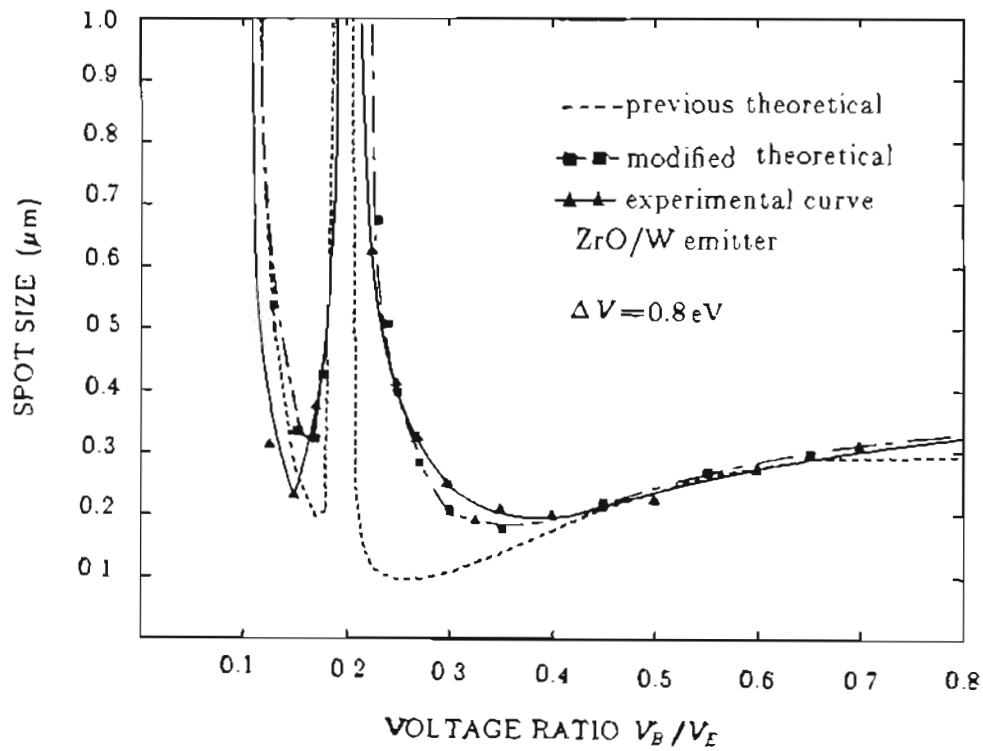

Fig.5-8 The spot size versus voltage ratio V_B / V_E for the ZrO/W emitter the ▲ line is experimental curve with r=1μm, I_P =8nA, α=2.2mrad and T=1800K. At the same condition the dotted line is the previous theoretical curve (Fig.5-2), the ■ line is a modified theoretical curve incorporating d_b where $c = 1.1 \times 10^5$ ($volt^{3/2} rad^{-1} A^{-1}$)

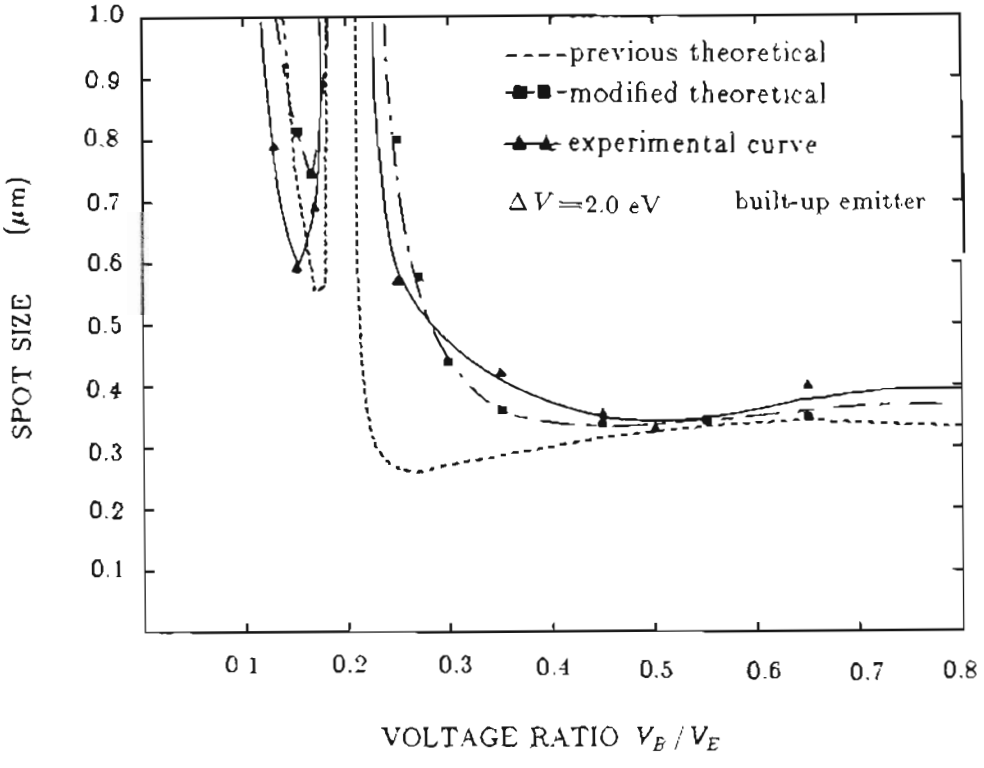

Fig 5-9 : The spot size versus voltage ratio V_B / V_E for the built-up emitter the solid line is the experimental curve (in Fig 5-6) with r=.07μm I_P=10nA, α=2.2mrad and T=1800K. At the same condition the dotted line is the previous theoretical curve (Fig.5-6). -■- line is a modified theoretical curve incorporating d_b where $c = 1.1 \times 10^5$ $(volt^{3/2} rad / Am)$.

low voltage range where the crossover forms in the column the radial broadening effect is much smaller and the correlation with experiment and prediction is again quite good.

A further prediction of the radial broadening is an increase with beam current. In Fig.5-4 is shown the increase in beam size with I' for V_B/V_E=0.40. In this range we expect Eq.(5-5) to govern d_b. Using the experimental results in Fig.3-2 and Eq.(5-1) the predicted values of d for the Fig.5-4 results were determined. Subtracting in quadrature the predicted from the experimental values of d for the r=0.35μm results we show in Fig.5-10 the difference which we ascribe to the radial broadening contribution. In accordance with the Eq.(5-5) expectations the radial broadening appears to increase linearly with beam current. From the slopes of Fig.5-10 curves the value of c was calculated to be 1.1×10^5 $(volt^{3/2}rad/A)$ which is in good agreement with the value used in Figs.5-8 and 5-9.

We conclude that radial broadening in field emission focusing columns is an important effect that must be considered when high current and low voltage focused beams are desired in conjunction with large column magnification. For a two lens collimated beam column using a field emission source we can quantify the previous statement by stating that when

$$\frac{I\ Z_g}{V_B^{3/2}\,\alpha} < 4.5\times10^{-13} \qquad (Am/volt^{3/2}rad) \tag{5-8}$$

one can expect less than a few hundred angstroms of radial broadening.

In light of condition (5-8) radial broadening problems could be greatly reduced if the C & W column optics were reversed. That is, by placing the decelerating electrostatic lens at the bottom of the column Z_g could be greatly reduced, thereby allowing

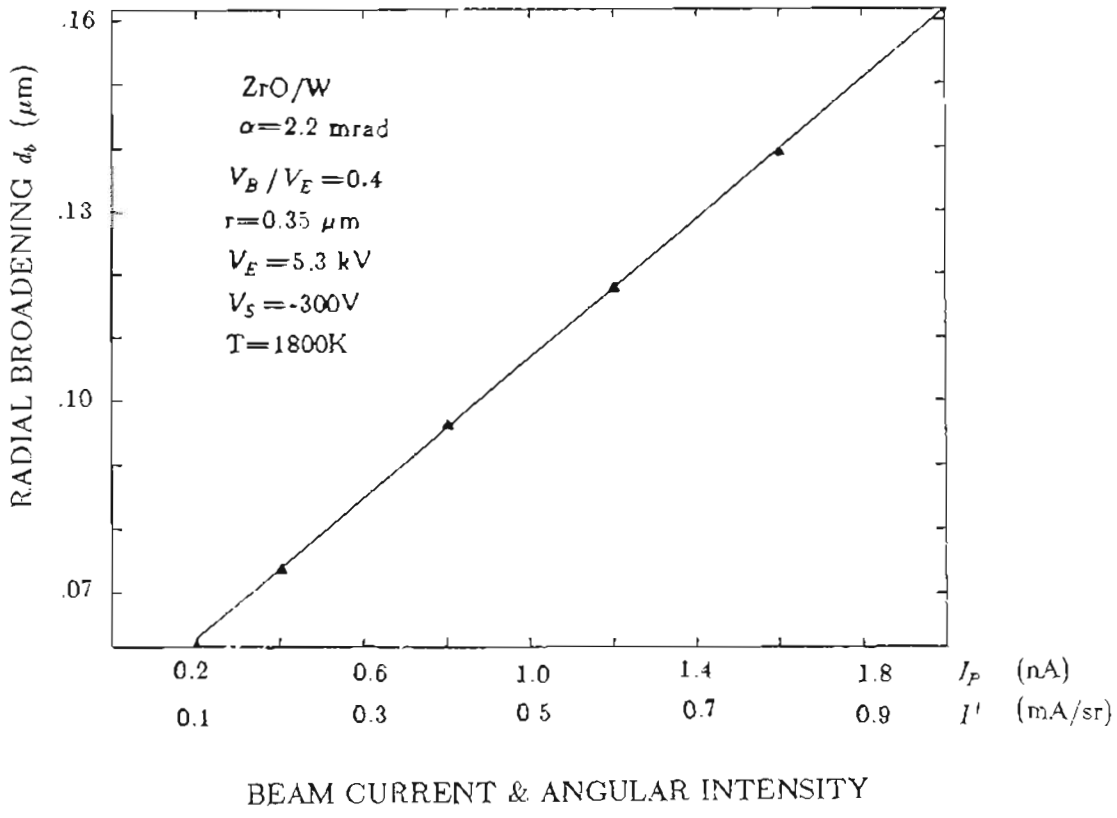

Fig.5-10 : The radial broadening d_b versus angular intensity I' (mA/sr) and beam current I (nA) based on the experimental data in Fig.5-4 and Eq.(5-1) for the ZrO/W emitter with r=0.35μm, α_o =.8mrad V_B / V_E =0.4 and V_E =5.3kV. The energy spread varies from Fig.3-2. The slope is 5495.9(cm/A) and $c = 1.1\times10^5$ ($volt^{3/2} rad$ /A)

a proportionate increase in I.

Finally, in Fig.5-11 a plot of the theoretical beam size versus V_E is given for two fixed voltage ratios. From these results one can conclude that if both low beam voltage and beam size are desired it is probably best to work at the minimum occurring at V_B/V_E=0.15 with V_E in the range of 7 to 9kV. This will allow one to realize the lower noise and energy broadening effects associated with larger radii emitters.

5.2 Current transmission

For practical reasons it is desirable that the emitter exhibits a large transmission, i.e. $I'\ \Omega/I_T$, where I_T is the total current and Ω the solid angle of beam defining aperture. In general, the effect of electrode geometry and V_S and V_E on I' or transmission can be derived by

$$I' \approx \frac{J r^2}{m^2} \tag{5-9}$$

From the Helmhotz-Lagrange relation

$$m = \frac{\alpha}{\theta} = \frac{1}{M}\left[\frac{V_o}{V_E}\right]^{1/2} \tag{5-10}$$

where θ is launch angle, V_o the initial energy of the electron. Combining Eq.(5-9) and (5-10) yields

$$I' = J\ r^2\ M^2\ \frac{V_E}{V_o} \tag{5-11}$$

Thus, we see that $I' \propto V_E$ for fixed V_o, J, M, and r. Therefore, if we increase V_S or L (spacing between emitter and anode) at fixed J, r, and M, we can expect V_E and hence I' to increase. This assumes the M is not changing much.

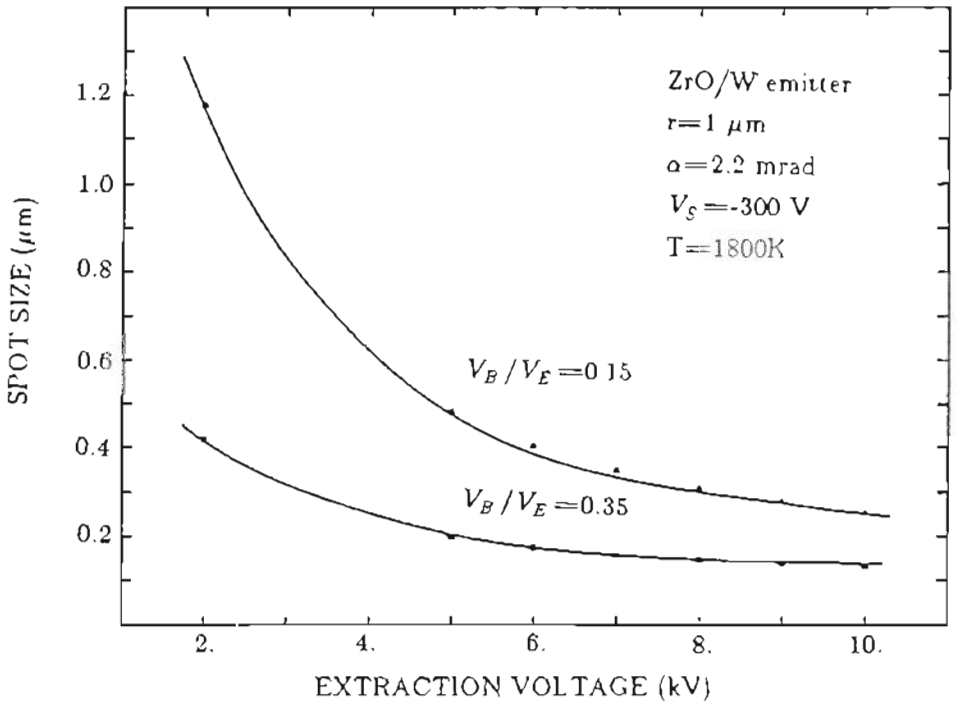

Fig 4-7 : The predicted influence of extraction voltage V_E upon spot size values at voltage ratio 0.15 and 0.35.

Fig.5-12 and Fig.5-13 show the variation of beam transmission with V_S. As expected the transmission increases due to a decrease in the angular magnification when V_E increases and V_S decreases. For the ZrO/W emitter the current transmission is in the range 0.4 to 1 (rad^{-2}) while for the W (100) built-up emitter the value is in the range 25 to 40 (rad^{-2}). Thus, there is a significant difference in transmission between the two TFE cathodes.

The main reason for the large transmission for the W (100) built-up emitter is that it operates in the T.F. regime, not in the Schottky regime like the ZrO/W emitter. This is due to its high work function ϕ=4.5eV (Fig.2-3 only applies to low ϕ(2.5eV)). Because of the low ϕ emission occurs from the emitter shank of ZrO/W but not in the case of the built-up W (100). A negatively biased suppressor reduces the emission from the shank, resulting in a lower transmission for the ZrO/W emitter.

Another difference is that for the ZrO/W emitter the current transmission shows a strong dependence on V_E. From the experimental data shown in Fig.5-14 we observe that

$$I_P / I_T \Omega \propto (V_E)^{1.0} \qquad \text{for } V_E \leq 5.5kV \tag{5-12}$$

$$I_P / I_T \Omega \propto (V_E)^{2.8} \qquad \text{for } V_E \geq 5.5kV \tag{5-13}$$

where I_P is beam current and $\Omega=\pi\alpha^2$ the emission solid angle.

In contrast, the built-up emitter current transmission shows a nearly uniform values in different extraction voltages because of the lack of electron emission from the emitter shank as shown in Fig.5-15.

Fig.5-16 shows the effect of emitter-to-anode spacing on transmission where V_E was varied to keep I_P constant. Transmission tends to increase with larger spacing.

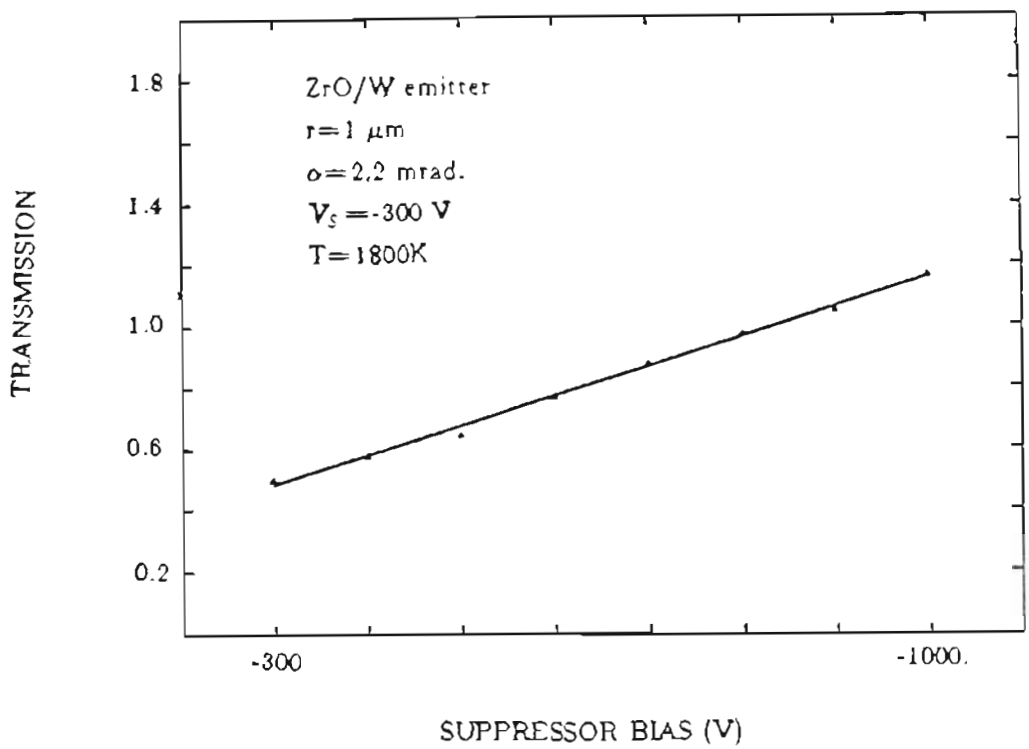

Fig.5-12 The influence of bias voltage upon transmission for the ZrO/W emitter. V_E was varied to keep constant beam current I_P=2nA.

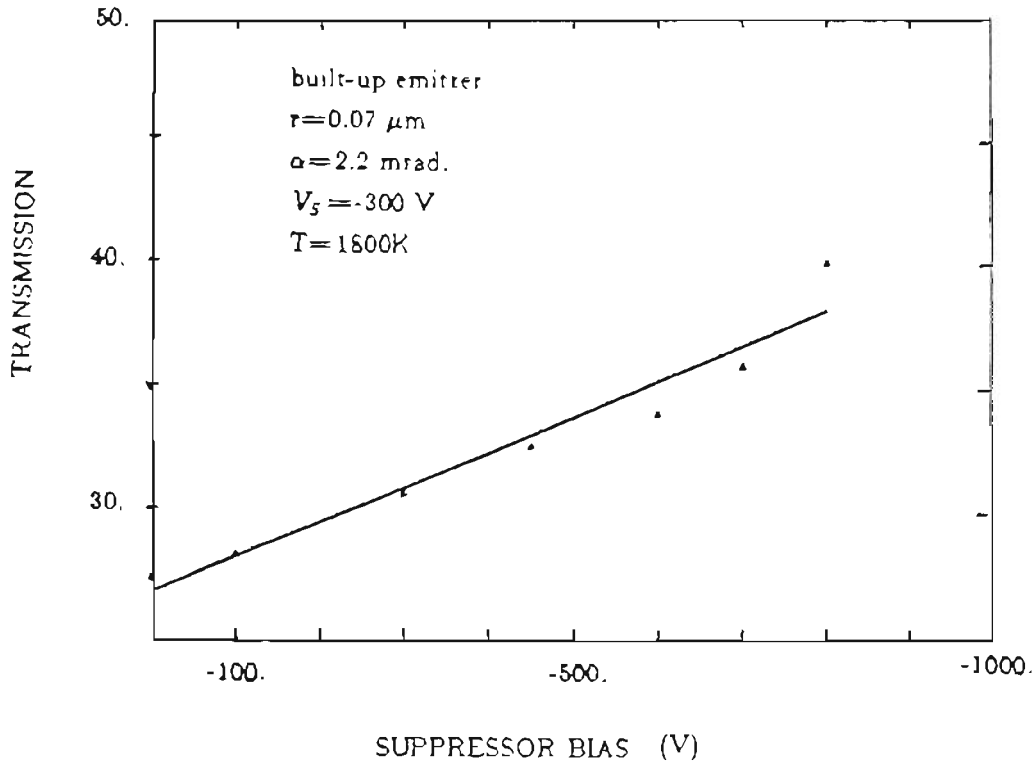

Fig.5-13 : The influence of bias voltage upon transmission for the W (100) built-up emitter. V_E was varied so as to maintain a constant beam current I_P =5nA.

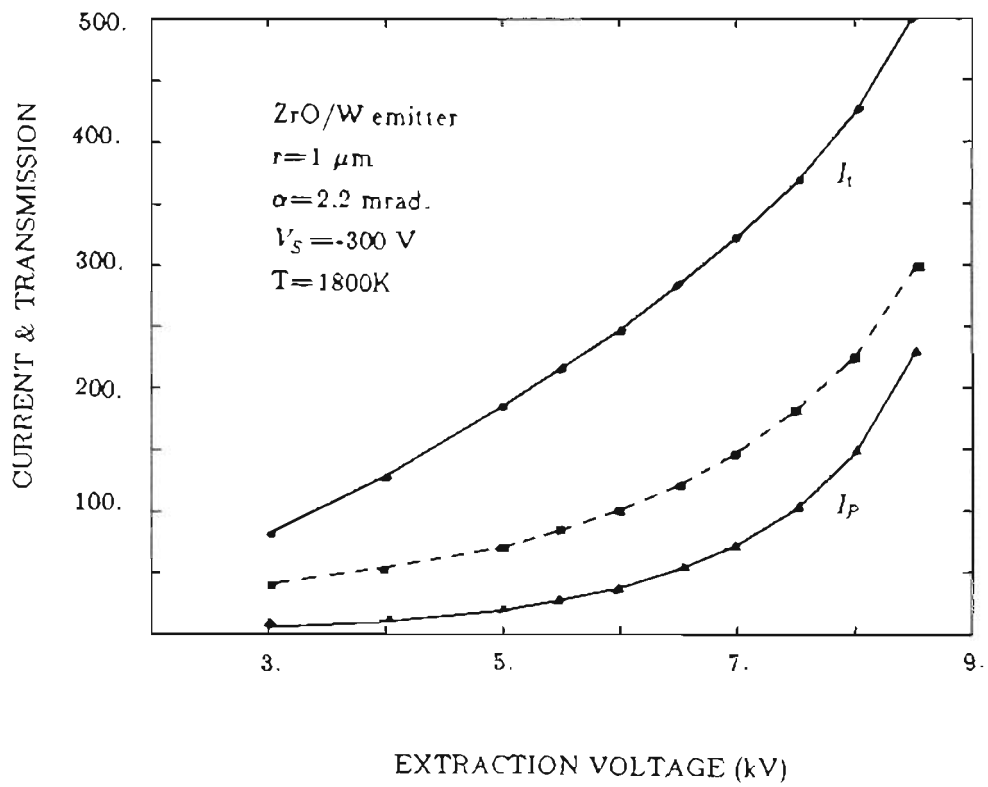

Fig 5-14 : The influence of extraction voltage upon transmission for the ZrO/W emitter with V_S =-300V. The three curves use the same scale, I_t is total emission current with unit (μA). I_P is beam current with unit (10^{-1}nA) and the dotted line is the transmission coefficient with unit (10^{-2}).

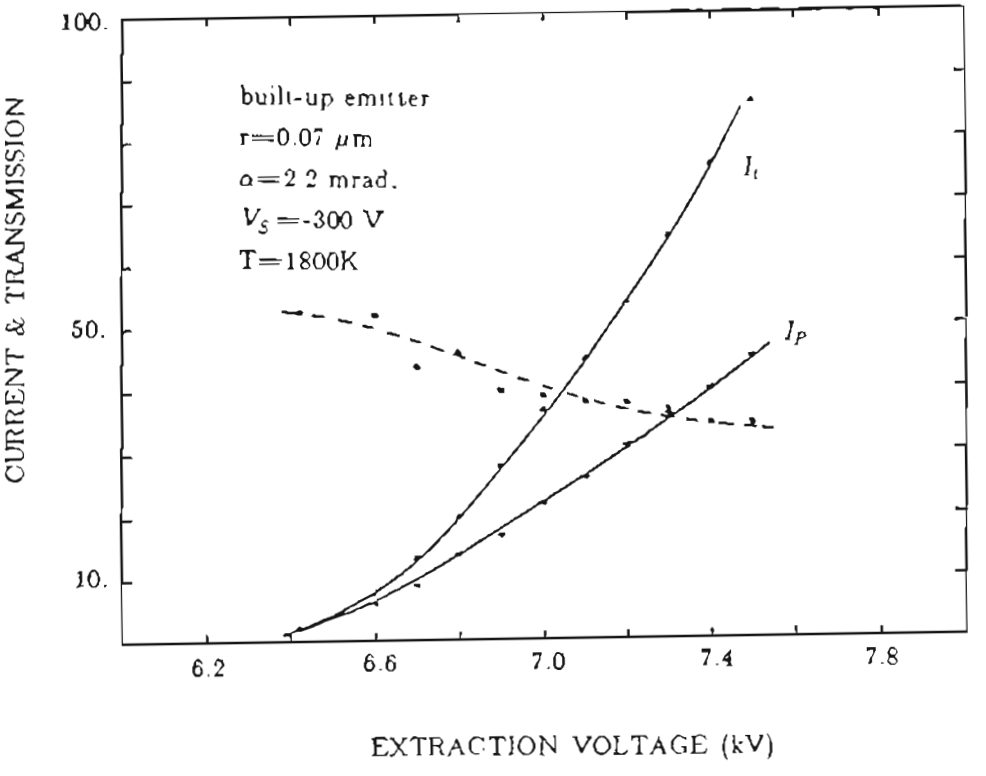

Fig.5-15 : The influence of extraction voltage for W (100) built-up emitter with V_S=-300V. The three curves use the same scale. I_t is total emission current with unit (μA), I_P is beam current with unit (nA) and the dotted line is the transmission coefficient.

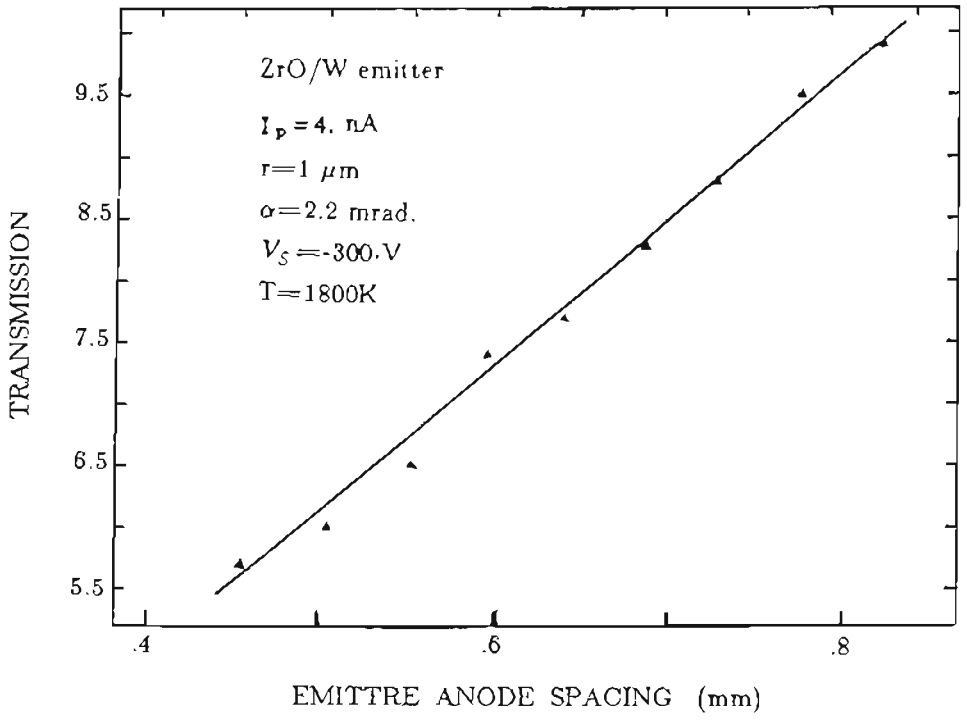

Fig.5-16 : The influence of emitter to anode spacing on transmission for the ZrO/W emitter. V_E was varied from 4 to 6kV so as to maintain a constant beam current of I_P =4nA.

The change of transmission with r, emitter to anode spacing, V_S and V_E mentioned above, can be generally related to the source optics and has a simple physical explanation. The angular magnification m is a parameter describing the convergence of the emitted beam from the emitter apex. If m is larger, the beam is more divergent. A divergent beam means that the beam spreads more and results in a lower transmission coefficient, and vice versa.

From Table 1 to Table 4, which are calculated results by using computer program SCWIM (see appendix A), one can see that m decreases with emitter radius, but with increased V_S, V_E and spacing. Fig.5-17 and 5-18 show the dependence of m on the V_S and V_E. The vertical height between two curves gives the m value.

A suppressor usually operating at -300V is used for both built-up and ZrO/W emitters to prevent thermal emission from emitter shank and outgassing at emitter apex vicinity by the incoming ion bombardment. It also provide an easy way to adjust the total emission current at fixed extraction voltage.

5.3 Noise level

Due to the low work function of the ZrO/W emitter its radius can be made larger (0.3-1.5 μm) than the built-up emitter (about 0.01-0.15 μm). If one assumes that current fluctuations are due to mobile adsorbed atoms contributing coverage fluctuations and thus causing local work function fluctuations, one can show that[26]:

$$\Delta I_P / I_P \propto A^{-1/2} \tag{5-14}$$

where $\Delta I_P = <\Delta I^2>^{1/2}$ and A is the emitting area seen by the probe. Thus, a larger emitter radius can greatly reduce the noise level.

The noise power spectrum for the ZrO/W emitter is shown in Fig.5-19 from 0.001Hz to 25kHz. The total mean square amplitude of the noise can be calculated

Table 1

The effect of emitter radius upon the angular magnification m (V_S =-300V and L=0.500mm)

	ZrO/W (100) (ϕ=2.8eV)			W (100) built-up (ϕ=4.5eV)		
r (μm)	0.3	1.0	3.0	0.01	0.05	0.07
V_E (kV)	4.3	6.0	7.0	3.5	6.0	6.8
m	0.216	0.248	0.257	0.244	0.331	0.343
I' (mA/sr)	1.05	0.974	1.01	0.966	1.01	0.986

Table 2

The effect of spacing between emitter and anode upon angular magnification m (V_S =-300V)

	ZrO/W (100) (ϕ=2.8eV, r =1.μm)			W (100) built-up (ϕ=4.5eV, r =.07μm)		
L (mm)	0.254	0.508	0.762	0.254	0.508	0.762
V_E (kV)	4.5	6.2	7.8	4.6	6.8	8.9
m	0.291	0.248	0.219	0.400	0.343	0.310
I' (mA/sr)	1.10	1.09	1.11	0.909	0.986	0.905

Table 3

The effect of V_S and V_E upon the angular magnification m at costant surface field F=0.069 (V/Å) for ZrO/W emitter (T=1800K, r=1μm, L=.500mm) (for the first trajectory)

V_S (kV)	-0.30	-0.40	-0.70	-1.10	-1.30	-1.50	-1.70	-2.00
V_E (kV)	6.00	6.20	6.60	7.10	7.35	7.65	7.95	8.35
m	0.223	0.221	0.215	0.207	0.203	0.200	0.197	0.192
I' (mA/sr)	0.97	1.03	1.08	1.13	1.16	1.18	1.27	1.36

Table 4

The effect of V_S and V_E upon the angular magnification m at constant surface field F=0.54 (V/Å) for built-up emitter (T=1800K, r=0.07μm, L=.500mm)

V_S (kV)	-0.30	-0.50	-0.70	-0.90	-1.10	-1.40	-1.70	-2.00
V_E (kV)	6.80	7.10	7.40	7.70	7.95	8.40	8.80	9.25
m	0.343	0.336	0.330	0.325	0.319	0.312	0.305	0.299
I' (mA/sr)	0.987	1.04	1.09	1.16	1.12	1.20	1.19	1.27

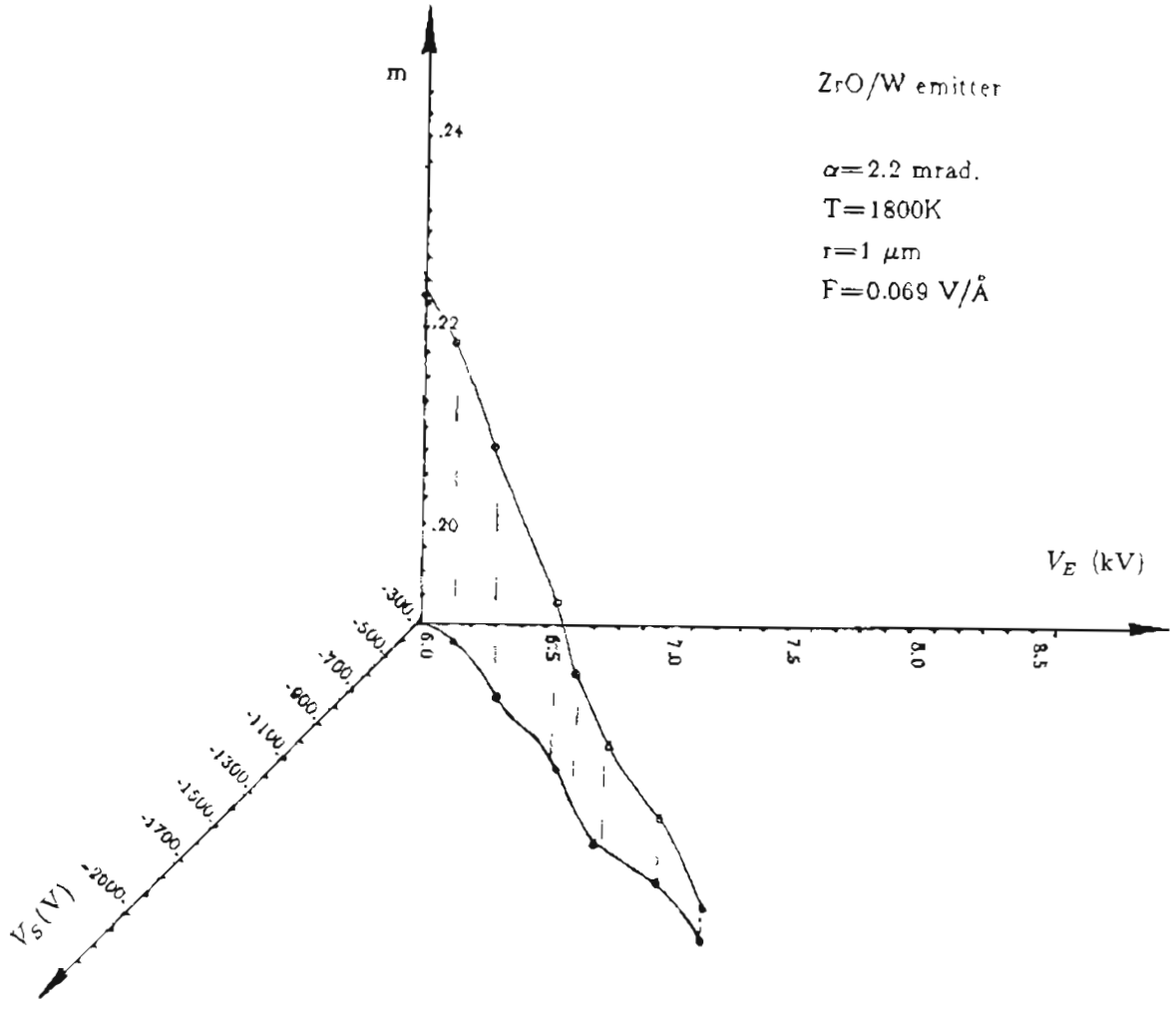

Fig 4-17 Angular magnification m versus V_S and V_E values in a fixed surface field F=0.069 V/Å for the ZrO/W emitter with r=1 μm, ϕ=2.8 eV and T=1800K.

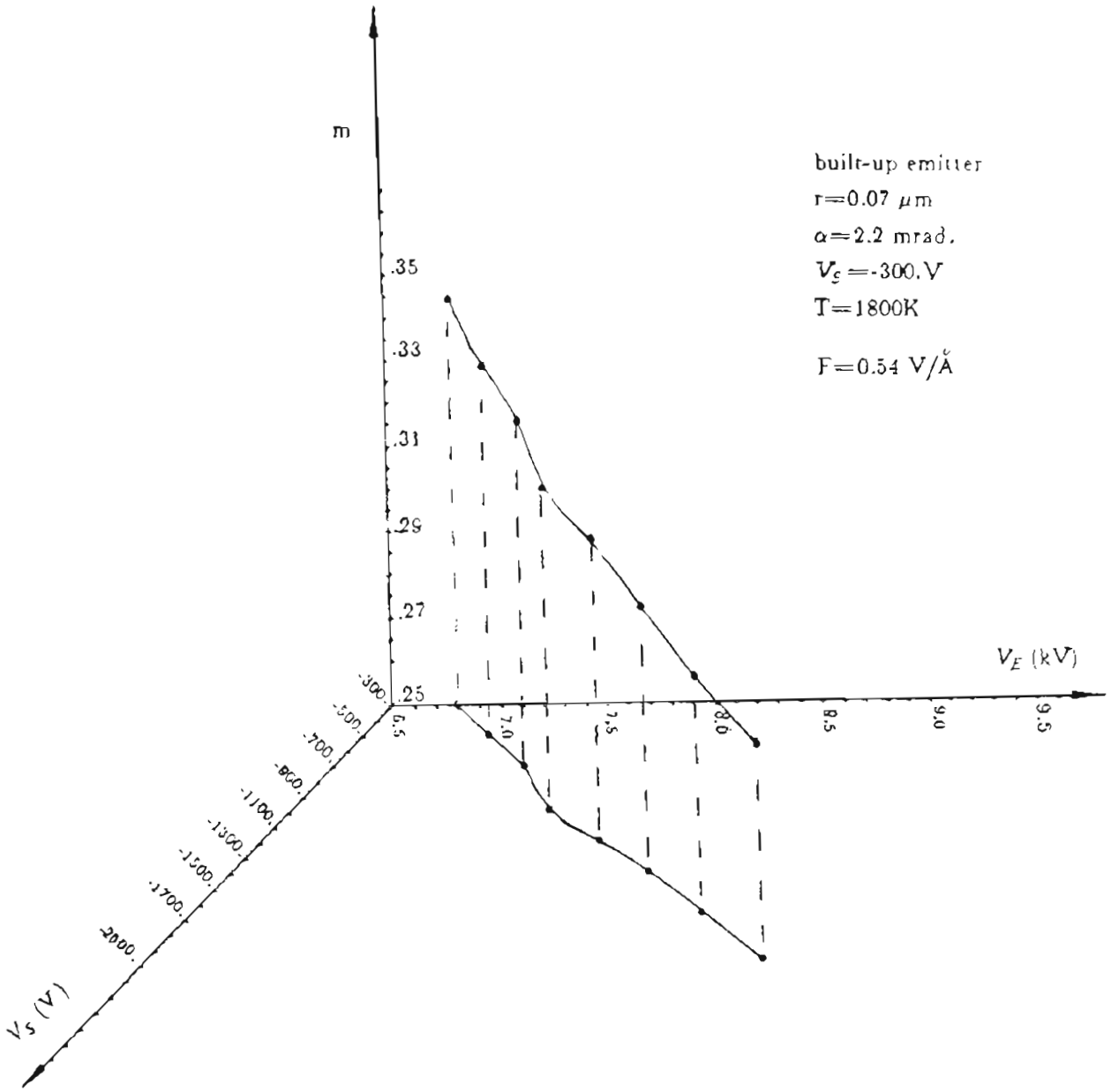

Fig 4-18 . Angular magnification m versus V_S and V_E values in a fixed surface field F=0.540 V/Å for the built-up emitter with r=0.07 μm, ϕ=4.5 eV and T=1800K

according to

$$<(\Delta I)^2> \; = \; \int \; S(f\,)\,df \tag{5-15}$$

where the S(f) is noise power density function. It is seen that for f> 10kHz the power spectrum follows $S(f\,) \propto 1/f$ relation. If we assume a 1/f relation for f> 10kHz, the shot noise level given by

$$<\Delta I^2> = 2\ e\ I\ \Delta f \tag{5-16}$$

is reached at about 190k Hz. Below 1Hz S(f) increases due to random thermal fluctuations which are confined to low frequencies[28].

The measured noise/signal ratio is $\sim 0.54\%$ in a band-width from 1×10^{-3}Hz to 25kHz for a typical ZrO/W emitter with r=1 μm as shown in Fig.5-19 which is about ten times less than the corresponding value for the built-up emitter ($\sim$5.0%) as shown in Fig.5-20. The effect of α, r and T on beam noise has also been investigated for the ZrO/W emitter and the results are depicted in Fig.5-21 to 5-25. From these results we determined the following empirical relationship:

$$(\Delta\ I_P\,/I_P\,)^2 \; = \; k\ \alpha^{-1}\ r^{-2} \tag{5-17}$$

where α is the aperture half angle (varied from 0.8 mrad to 2.2 mrad) and r is the emitter radius (varied from 0.35 μm to 2.3 μm) in our experiments. Thus Eq.(5-17) is consistent with Eq.(5-14). Combining Eq.(5-16) and Eq.(5-17) one can obtain the following empirical relation for the ZrO/W emitter:

$$(\frac{\Delta I_P}{I_P})^2 = \frac{k}{\alpha r^2} + \frac{2e}{I}\,(f\ - 190{,}000) \qquad \text{for } f\ > 190kHz \tag{5-18}$$

where k=$2.\times10^{-16}$ $(rad^{-1}cm^{-2})$ from our experimental data.

However, such an empirical relation does not hold for the built-up emitter which has a noise/signal (n/s) value that is independent of the aperture size as shown in

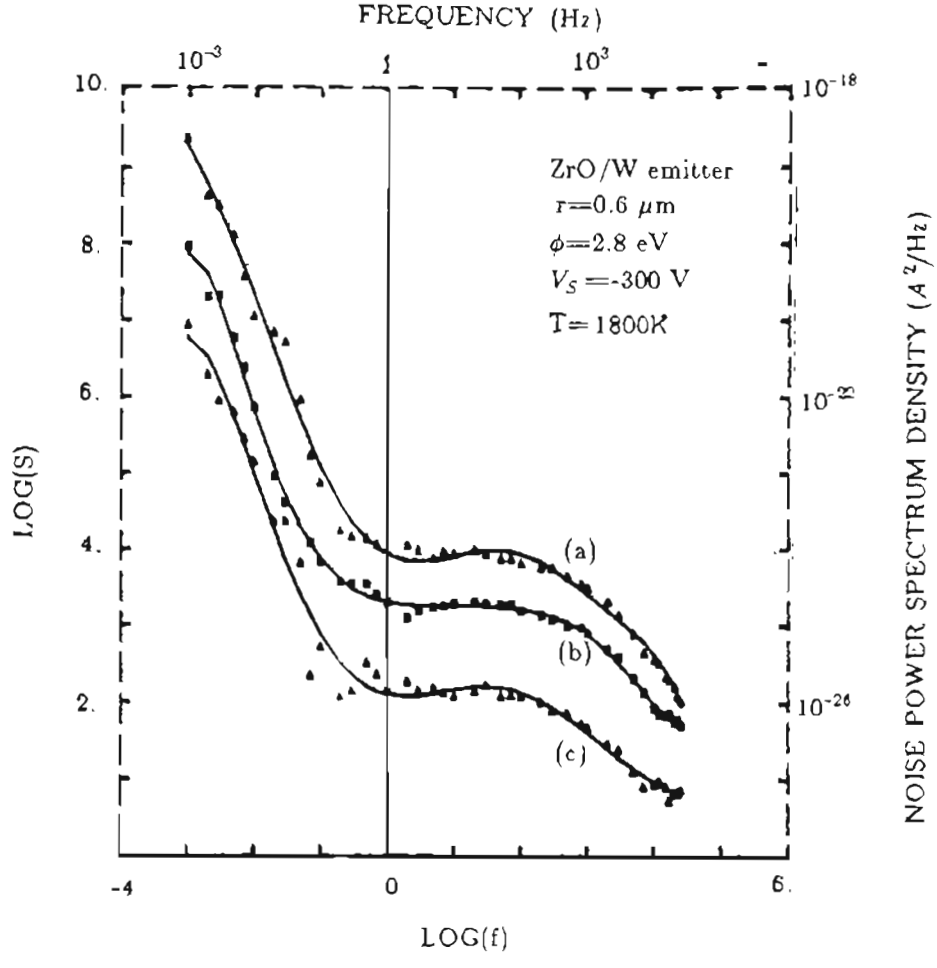

Fig.5-19 : Noise power spectrum for a ZrO/W emitter in a band-width from 10^{-3} to 25k Hz: (a) aperture half angle α=2.2 mrad, I_P =8.75nA and n/s=0.54% (b) α=1.67 mrad. I_P =3.6nA and n/s=0.60% (c) α=0.8 mrad. I_P =0.94nA and n/s=0.88%.

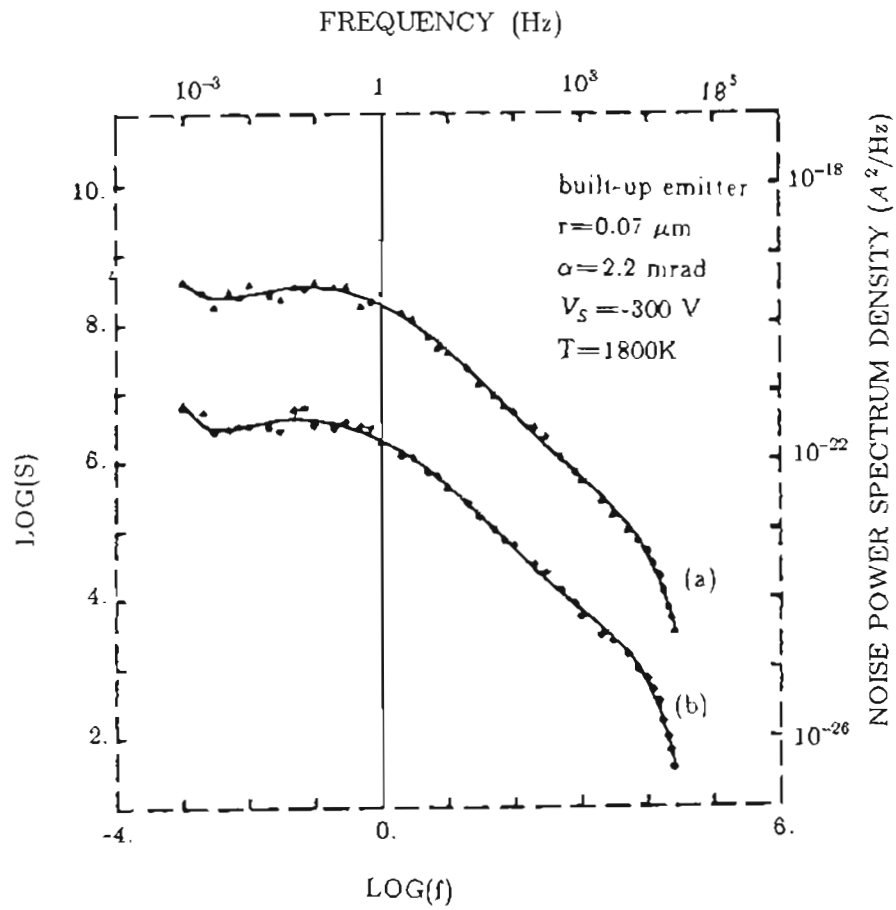

Fig.5-20 : Noise power spectrum of built-up emitter. (a) I_P =14.3nA and α_0=2.2mrad. (b) I_P =1.5nA and α_0=0.8mrad

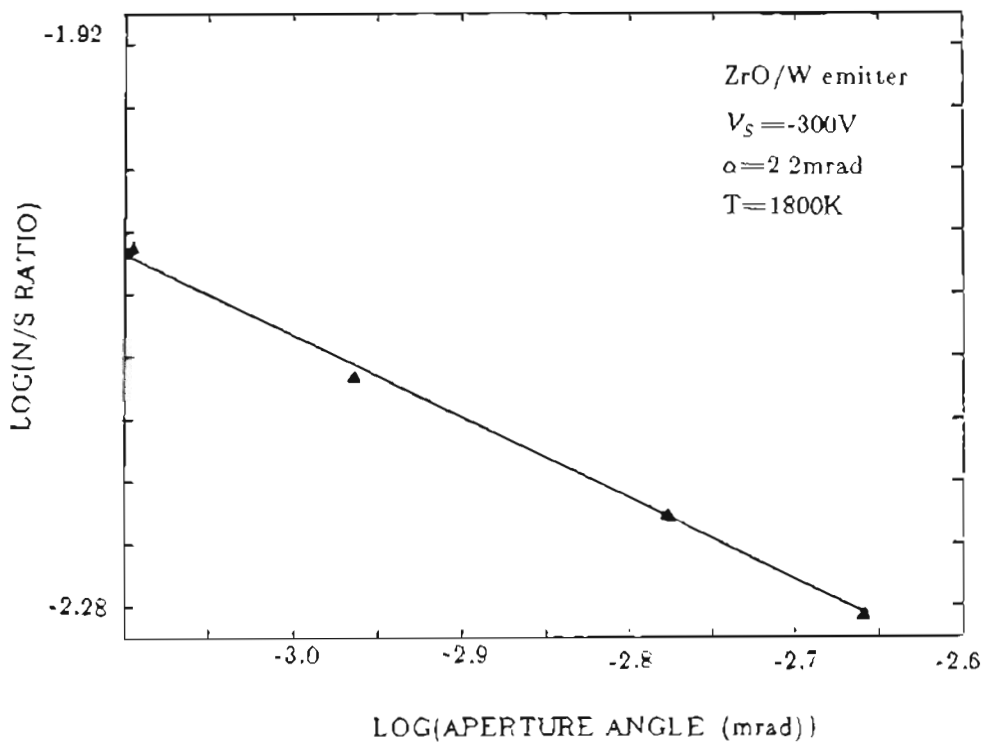

Fig.5-21 : Plot shows the measured relationship between aperture half angle α and noise to signal ratio over the frequency range 0.001Hz to 25kHz

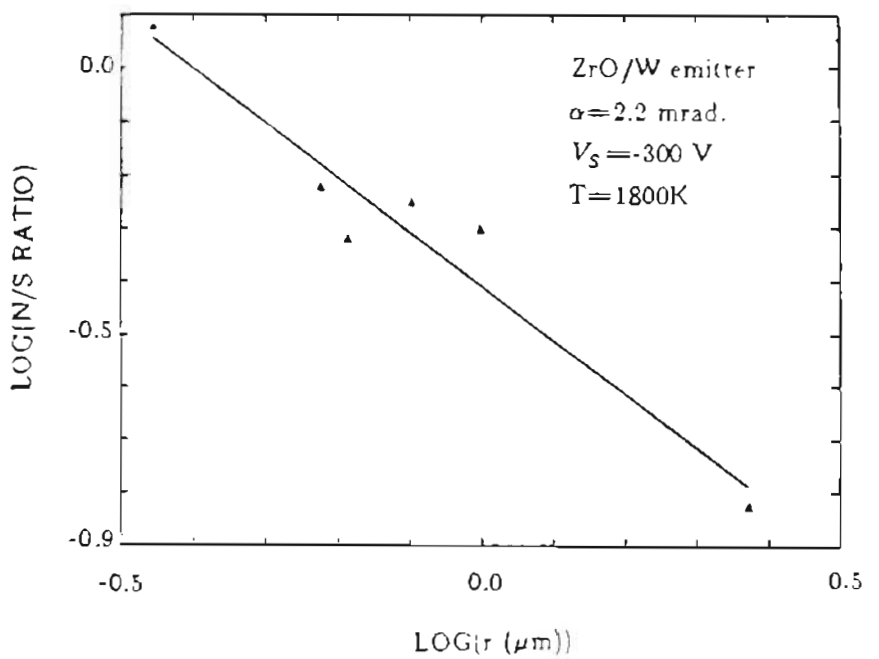

Fig.5-22 : The plot shows the exponential relationship between noise to signal ratio and emitter radius for the ZrO/W emitter. It shows $N/S \propto r^{-1}$

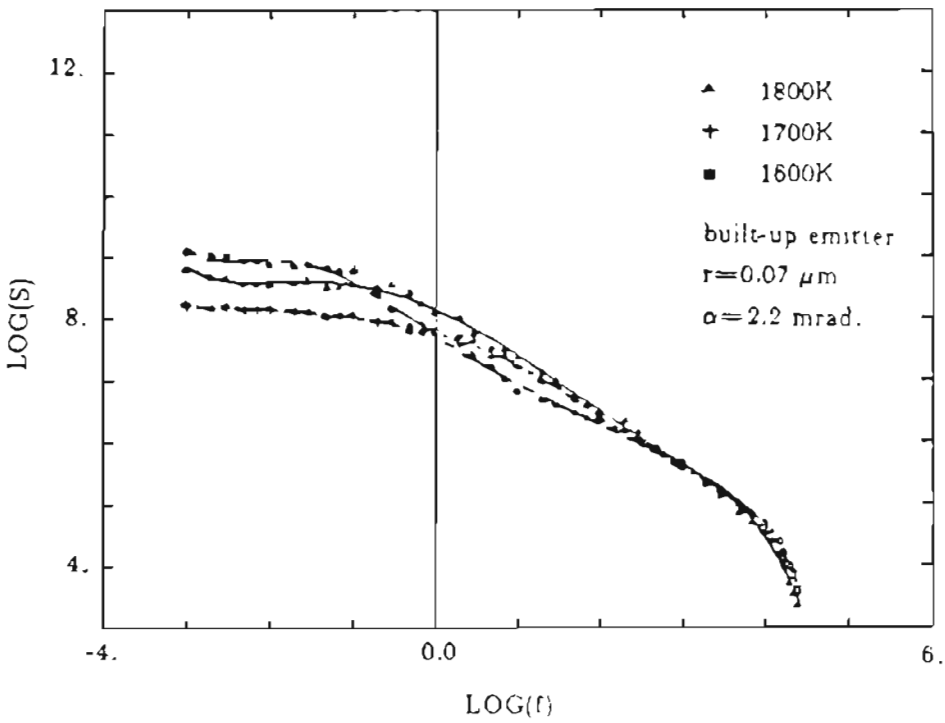

Fig 5-23 : Plots show S(f) vs f for three different temperatures for the built-up emitter with noise to signal ratio 5.55%(1800K), 5.18%(1700K) and 5.10%(1600K) from 10^{-3} to 25k Hz.

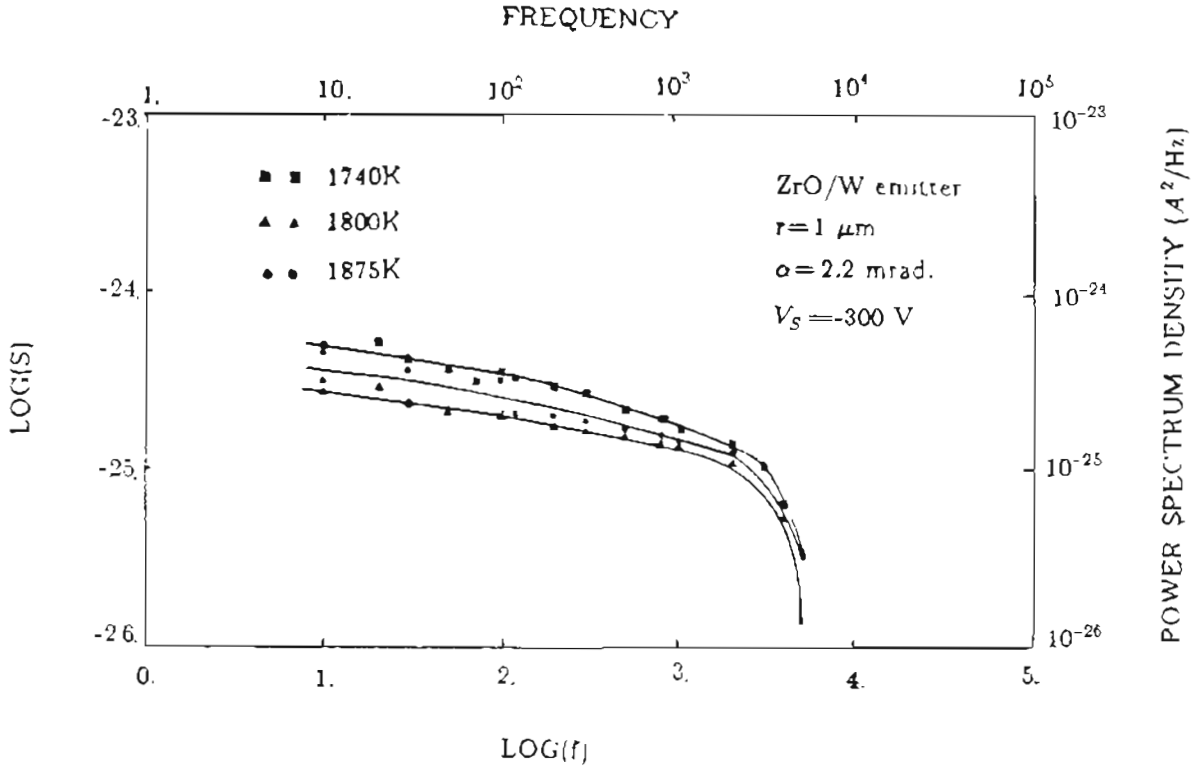

Fig.5-24 : Plots show S(f) vs f for three different temperatures for the ZrO/W emitter with the noise to signal ratio 0.65%(1740K), 0.60%(1875K) and 0.55%(1800K) from 1 to 5.k Hz.

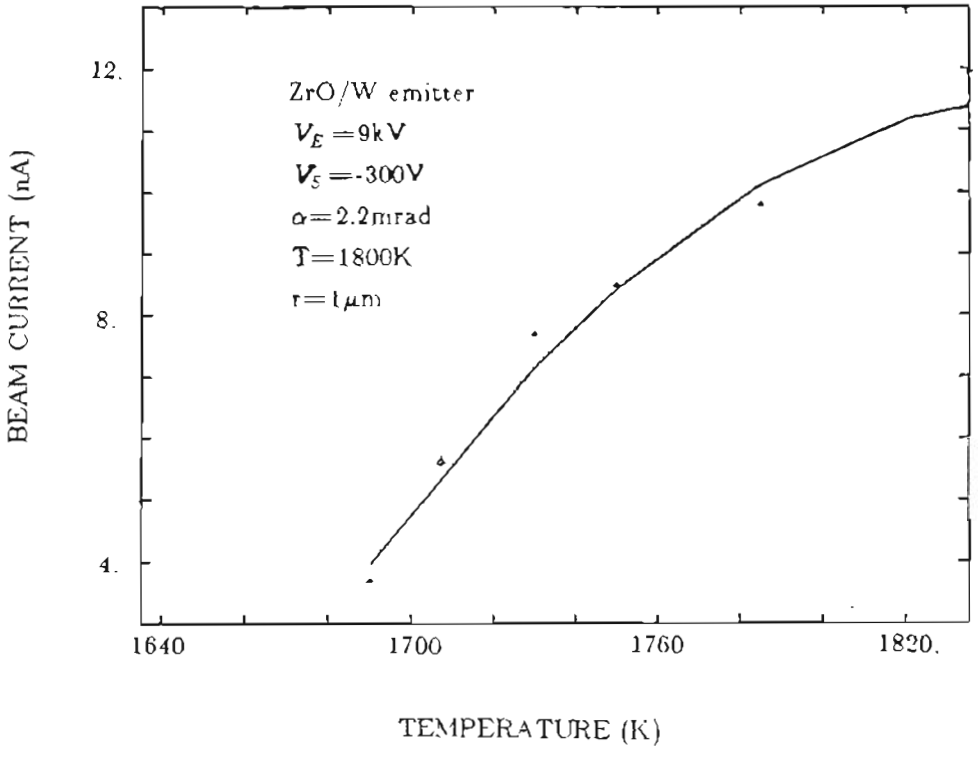

Fig.5-25 : Beam current versus operation temperature for ZrO/W emitter.

Fig.5-20 in which two curves with different aperture angles (2.2 and 0.8 mrad) and beam currents yield similar (n/s) ratios, 4.73% and 4.94%, respectively. The reason may be that the emission area for the built-up emitter can be written as

$$A = 2\pi r^2 (1 - cos\,\theta) = 4\,\pi r^2 \sin^2\frac{\theta}{2} \approx \pi r^2\theta^2 = \frac{\pi r^2\,\alpha^2}{m^2} \qquad (5\text{-}19)$$

For the built-up emitter, r≈500$\mathring{A}$, m≈0.3 and α=2.2 mrad., one can calculate the emission area $A \approx 4.2\times10^{-15}$ cm^2 and the emission radius $r_o = 3.6\mathring{A}$. This is on the order of one atom size and indicates that the emission region is too small to result in any averaging effects which determine the noise level. This explains the independence of (n/s) on α and r for the built-up emitters.

Because of the nearly constant value of (n/s) for the built-up emitter, we assume that Eq.(5-18) has an expression as follows

$$(\frac{\Delta I_P}{I_P})^2 = \frac{2\times10^{-16}}{A_o + \bar{A}} + \frac{2e}{I}\,(f - 190{,}000) \qquad (5\text{-}20)$$

where $A_o = 1.0\times10^{-13}$ cm^2, which relates to the largest possible (n/s) value (~5%), and $\bar{A}$ is an apparent emission area with the value, $\bar{A} = \alpha\, r^2$, in our experimental range. Once $\bar{A} \le A_o$, the (n/s) will take on the largest possible value as observed for the built-up emitters. Eq (5-22) holds over the working range for the ZrO/W emitters ($0.8<\alpha<2.2$ (mrad.) and $0.3<r<2.3$ (μm)), and is consistent with the results of the present built-up emitters ($0.8<\alpha<2.2$ (mrad.) and r~500$\mathring{A}$). But, it seems that more theoretical and experimental work is required to describe the relationship among the (n/s), α and r since on geometrical grounds we would expect $\bar{A} \propto (\alpha r)^2$ instead of αr^2.

As mentioned previously the elevated temperature is one of the key factors in thermal field emission. A suitable temperature range with high beam current and low noise level can be chosen experimentally. Fig.5-25 shows the beam current versus temperature. Because ZrO/W emitter works in the intermediate region between

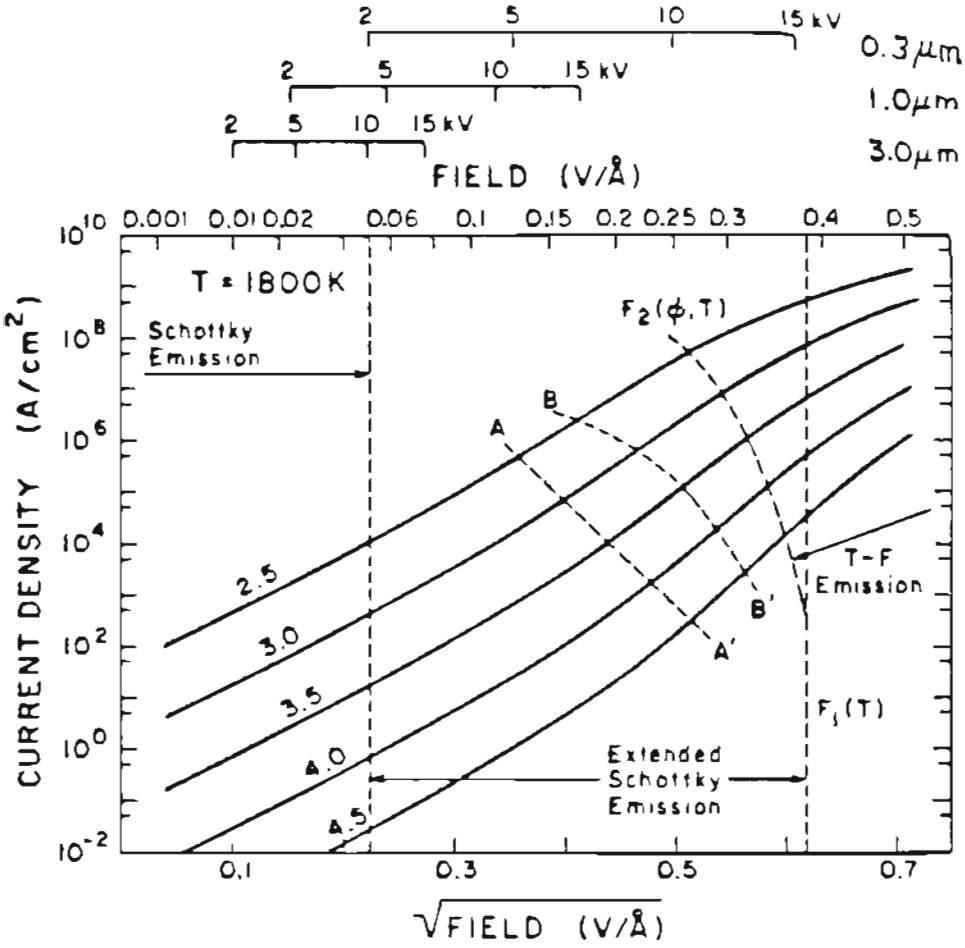

Fig.5-26 : Theoretical Schottky plot based on Eq.(5-20). The value of V_E for various emitter radii are indicated at the top of the graph.

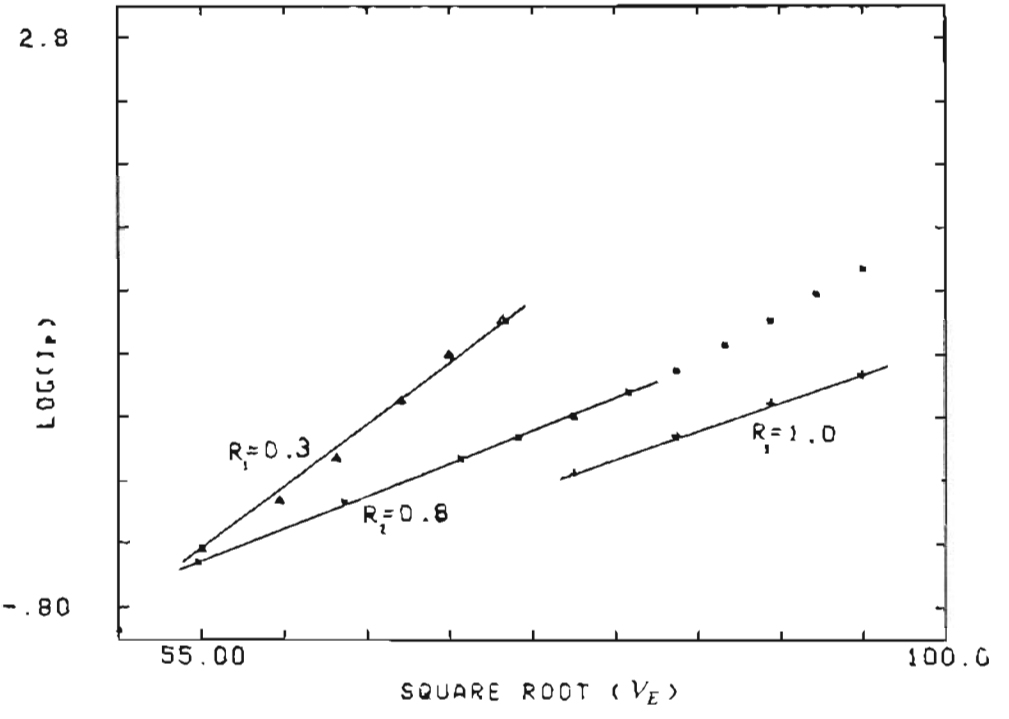

Fig.5-27 : I-V characteristic for four ZrO/W emitters taken at T=1800K and α_0=2.2mrad. The emitter radius obtained from SEM inspection is indicated in μm.

Table 5

Summary of emitter radius and work function and β values where

β is the geometra factor from the Schottky equation;

β_C is the corrected geometry factor;

r_{ES} is the estimated tip radius;

Φ_{ES} is the estimated emitter work function;

r is the emitter radius from SEM photos;

β (1/cm)	2804.	1478.	1177.
β_C (1/cm)	2540.	1321.	1047.
r_{ES} (μm)	0.30	0.75	1.05
Φ_{ES} (eV)	2.98	2.95	3.12
r (μm)	0.34	0.80	1.0

thermionic and field emission, it shows certain dependence of temperature. The operating temperature should be high enough to anneal ion sputtering damage and to cause desorption of chemisorbed contaminations[27]. Fig.5-23 shows that the temperature has only a small effect on the noise level of a built-up emitter. The noise signal ratios are 5.55%, 5.18%, 5.10% for temperature 1800K, 1700K, 1600K, respectively. A similar small effect of temperature occurs for the ZrO/W emitter as shown in Fig.5-24, where the three curves for the noise spectra at 1800K, 1875K and 1740K give corresponding noise signal ratios of 0.55%, 0.60% and 0.65%.

5.4 Method for estimating emitter radius

In this section we show how one may use the $I_P(V)$ characteristic to obtain a value of r and ϕ when the emission mode is the Schottky or extended Schottky mode[43]. The cathode current J_S is expressed by Schottky equation (see Eq.2-11) as

$$J_S = 120\ T^2 e^{(-\phi + cF^{0.5})/kT} \tag{5-21}$$

The Schottky equation is valid only for field low enough so that no significant tunneling current contributes to the value of J_S. A measure of the tunneling current is given by

$$q = \frac{(h/2\pi)e^{1/4}F^{3/4}}{\pi(2m)^{1/2}kT} \tag{5-22}$$

For q=0.25, emission is still basically described by Schottky equation. For q=0.5, half the current is due to tunneling, and the current density J_{ES} is given by

$$J_{ES} = J_S \frac{\pi q}{\sin \pi q} \qquad (q < 0.75) \tag{5-23}$$

Theoretical J_{ES} relationships for various work functions at T=1800K are shown in Fig.5-26. By use of the SCWIM computer program we can obtain a relationship

between the field factor β (=F/V) and the geometrical parameters[43]: emitter radius r and emitter-anode spacing L as

$$beta = 0.322\,(1-x)\,r^{0.689}\,L^{0.635} \qquad (\mathrm{cm}^{-1}) \tag{5-24}$$

where $x = V_S / V_E$.

To proceed one makes a Schottky plot (i.e. $\log(I_P)$ vs. $V_E^{1/2}$) of the data as shown in Fig.5-27. Then, according to Schottky's equation we get geometrical factor β as follows

$$\text{slope} = 3.8\,\beta^{1/2}/kT \tag{5-25}$$

where β is in cm^{-1} and k in eV/deg. This value of β is higher than the true value because the emission is usually beyond Schottky's regime. Thus, we substitute the measured value of β into an iteration program to obtain the true value of β. From the true β value and Eq.5-23 the emitter radius is obtained.

Finally, from the calculated F, J, and m value which can come from SCWIM program or the empirical expression[43]

$$m = 0.04733\,(1-x)\,/r^{0.0645}L^{0.338} \tag{5-26}$$

the work function is easily calculated from Eq.(5-21). Table 5 summarizes the values of β, ϕ and the calculated and measured values of r. The close agreement between the experimental and calculated r values supports the validity of this method for obtaining r values.

5.5 Emitter life

It is found in experiments that emitter life termination usually occurred with a vacuum arc initiated by excessive local values of the emitted current density due to either a sudden local increase in electric field or a sudden decrease in work function,

which may result from causes internal or external to the cathode. Two main external causes have been previously recognized: sputtering of the emitter surface by ion bombardment or contamination by low work function materials. For temperatures high enough ($>$1800K) sputtering and contamination have little effect due to rapid evaporation of contamination and rapid smoothing by surface migration. So life termination may caused by agents within the cathode[29]. It is assumed that the cathode life is independent of environment and closely related to the degree of purity of the cathode material. But in practical operation most emitters were destroyed due to carelessness with too high a pressure or mechanical misalignment. The intrinsic life time is very long ($>$5000 hours). For the ZrO/W emitter, the life is usually longer than the built-up emitter because of its larger emitter radius making it more resistant to transients.

Chapter 6

The gun structure and virtual source size calculations

6.1 Virtual source size

The primary cause of the high brightness of field electron sources is a very small virtual source size d_V. It is of great importance to determine whether the non-spherical shape of the ZrO/W and built-up emitter greatly alters d_V. Because of its expected small size (<200Å) d_V is very difficult to measure experimentally. Using a sphere on orthogonal cone model of the emitter Wiesner[30] was able to calculate d_V and found a minimum value of $\sim$30Å. In this section we use the SCWIM computer program and analysis techniques similar to that of Wiesner to carry out calculation of d_V for a non-spherical emitter.

The virtual source of a field emitter in the electron gun configuration is the waist of the crossover formed by the backward projection of all electron trajectories which pass through the beam defining aperture. This is not a point, however, due mainly to the fact that electrons can be emitted with lateral velocity due to their thermal motion. There is a statistical distribution for their momenta. One straightforward method of obtaining d_V is to project the tangent of the calculated trajectories with all possible conditions in field free space and obtain the intersections as shown in Fig.6-1. The minimum of the intersections represent the virtual source size.

Another method of obtaining d_V is that given by Wiesner. His method treats the emitter-anode region as an electron optical lens with the cathode emitting surface

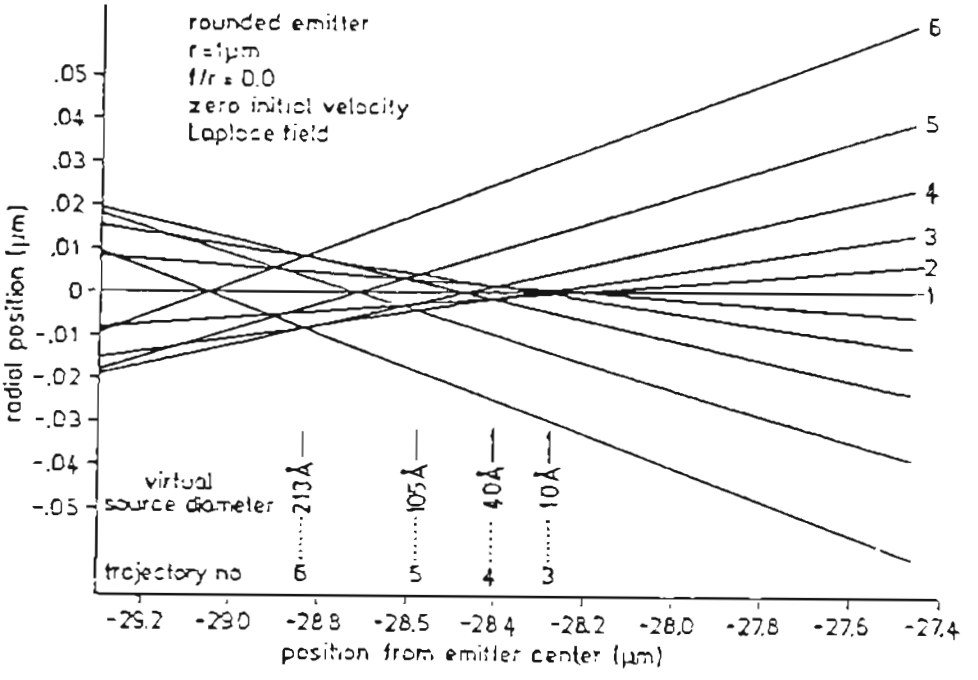

Fig 6-1 : Diagram showing extrapolated tangents of trajectories launched with increasing distance from spherical emitter axis. Values of d_s are observed to increase with increasing aperture angle.

being the object and the virtual source being image. This permits an evaluation of the virtual size from the quadrature sum of the calculated Gaussian, spherical, chromatic aberrations and diffraction disk diameters. This is the method we used in the present study.

6.2 Calculation model and program

A sphere-on-cone (SOC) model of the emitter shape is shown in Fig.6-2. This model provides an analytical expression for the electric field and potential at all points between emitter and anode. Wiesner used these analytical fields and potentials to calculate trajectories of electrons from emitter to anode. The trajectories were all calculated in the meridian plane of the system, i.e. no skew trajectories were considered. The launch conditions of the electrons were divided into three groups:

1) cold-electron : zero initial velocity; various initial positions on cathode surface;

2) α-electron : fixed initial velocity; various initial directions; initial position on cathode apex;

3) v-electron : various initial velocities; initial direction tangent to apex; initial position on cathode apex. These three groups of electrons are shown in Fig.6-3.

According to the Abbe sine law:

$$v_0 \sin \alpha_0 = M \ v \ \sin \alpha \tag{6-1}$$

where v_0 is the initial velocity, α_0 is the initial angle, v is the final velocity and α is final angle (slope). From α–electron data we can determine the linear magnification M from Eq.(6-1). The spherical aberration coefficient C_S was calculated by fitting the α or cold electron results to the longitudinal spherical aberration equation:

$$\Delta Z \ = \ C_S \ \alpha^2 \tag{6-2}$$

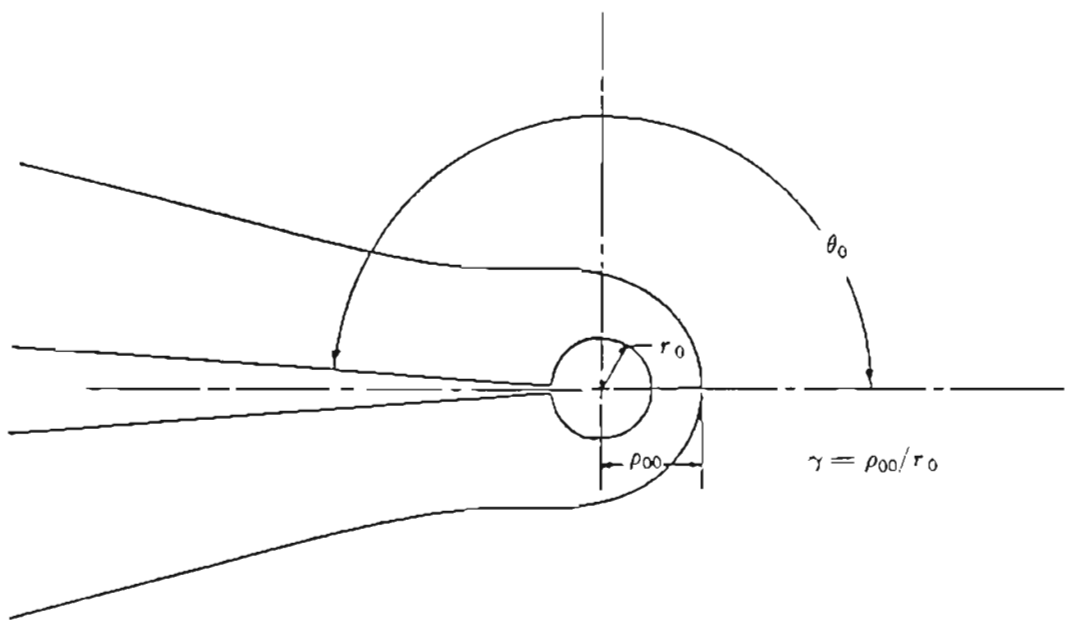

Fig.6-2 : Point cathode modeled as an equipotential of a sphere-on-orthogonal cone (from Wiesner)

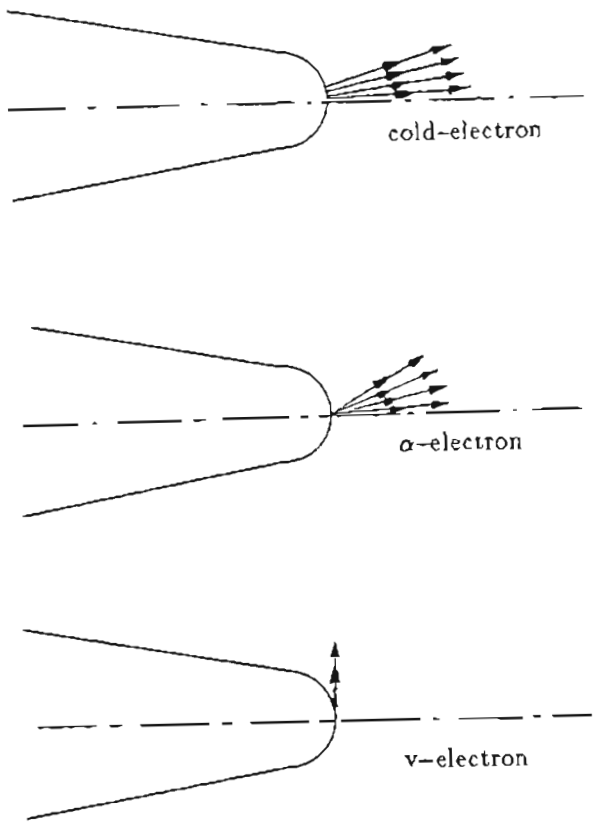

Fig.6-3 : Three of the electrons defined in the calculation of virtual source size by Wiesner's method.

where ΔZ is the difference in the axis crossing coordinates for the paraxial and marginal (slope= α) trajectories, α is the trajectory angle with the axis. Having calculated C_S the spherical blur disk diameter d_S obtained from

$$d_S = 2\ C_S\ \alpha^3 \tag{6-3}$$

Eq.(6-3) holds in the Gaussian image plane, however, in the plane of the circle of least confusion d_S is given by

$$d_S = 0.5\ C_S\ \alpha^3 \tag{6-4}$$

To calculate the effective chromatic aberration coefficient C_C we make use of the V-electron data to obtain a value of C_C from the longitudinal chromatic aberration equation

$$\Delta Z = C_C\ \Delta V / V \tag{6-5}$$

where ΔV is the longitudinal thermal energy of the electrons. The chromatic aberration disk diameter d_C is given by

$$d_C = C_C\ \alpha\ \Delta V / V \tag{6-6}$$

The diffraction disk diameter is given by

$$d_d = \frac{14.9694 \times 10^{-4}}{\sqrt{V}\ \alpha} \qquad (\mu m) \tag{6-7}$$

where V is extraction voltage.

The cold-electron trajectories are used to determine the Gaussian image disk size by fitting the data to

$$\alpha = m\ \theta_0 \tag{6-8}$$

where α is final trajectory slope, m is the angular magnification and θ_0 is the initial angular position on the cathode. For the spherical emitter the radius of the

corresponding Gaussian image disk r_g is given by

$$r_g = M\ r\ \sin\theta_0 \tag{6-9}$$

Substituting Eq.(6-8) into Eq.(6-9) one can obtain r_g as

$$r_g = r\ \alpha\ sin\,(\frac{M}{m}) \approx M\ r\ \frac{\alpha}{m} \tag{6-10}$$

For the ZrO/W faceted emitter the formula for r_g is slightly modified and is given as

$$r_g^F = 0.9539\ M\ r\ tan\,(\frac{\alpha}{m}) \tag{6-11}$$

It is worth noting that in a field emission gun, it is usually the Gaussian image of the cathode that is imaged by the subsequent focusing system. This is different from the situation in an ordinary thermionic gun, such as an LaB_6 gun, in which the crossover is imaged. This is because the cathode image is smaller than the crossover, in the case of a field emission gun.

The quadrature sum

$$d = (d_S^2+d_C^2+d_d^2+d_g^2)^{1/2} \tag{6-12}$$

gives the diameter of the apparent or virtual source. However, before Wiesner's procedure can be performed a method to get precise trajectory data has to be developed. The method used in this study was a finite difference scheme using a spherical coordinate with increasing mesh (SCWIM)[31]. With this simulation the field calculation can be done on arbitrary shaped electrodes regardless of the very large geometrical difference between the emitter and other electrodes.

A schematic representation of the SCWIM model is shown in Fig.6-4. The radial mesh size increases from the emitter outward according to a geometrical series with a term ratio $(1-h_\theta)^{-1}$, where h_θ is angular mesh size, in radians. If one takes h_θ on both sides to be same, then a quasi-equi-distance central difference scheme occurs (i.e.

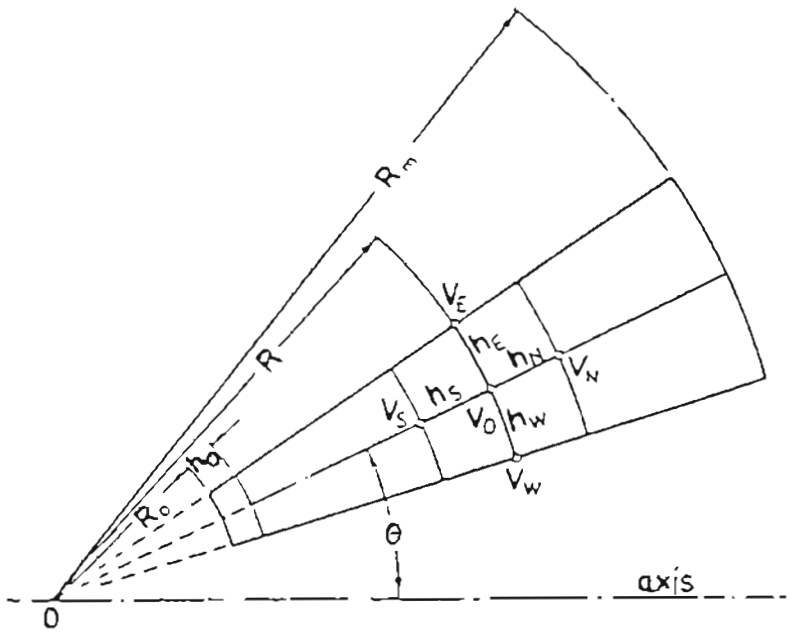

Fig.6-4 : Schematic representation of the mesh arrangement used in the SCWIM method. The minimum and maximum electrode dimensions are R_0 and R_m, respectively.

$h_S = h_W = h_E$ in Fig.6-4) which leads to a truncation error between that of nonequidistance schemes, approximately proportional to h_θ^3. In order to realize this scheme the radial mesh interval h_n (along a radial vector) is

$$h_n = h_0/(1-h_\theta)^n \tag{6-13}$$

where n is the radial mesh point number. The required number along a radial vector can be calculated by

$$n = \frac{ln\,(R_0/R_m)}{ln\,(1-h_\theta)} - 1 \tag{6-14}$$

where R_0 is the apex radius and R_m is the maximum dimension of the gun. Generally, the number of the radial mesh points approximately doubles when the ratio of geometrical sizes increases by two orders of magnitude. Because of this unique feature of SCWIM one is able to treat the entire gun at once without unreasonable demand on computer storage capacity. At the same time, the inaccuracy and complexity connected with the "successive magnification" approach are eliminated. In areas remote from the emitter the mesh size appears too large; however, the field in such remote areas are fairly weak, therefore, the mesh arrangement in SCWIM matches the feature of field emission guns very well.

6.3 Emitter surface field and current density

There are several emission parameters used to describe thermal field emitters. They are emission current density J, source brightness β , and angular current intensity I' . The Fowler-Nordheim theory can be used to obtain J. Average brightness is given by $\beta = J/\Omega = J/(\pi\alpha_0^2)$, where α_0 is the aperture half angle subtended to the emitter. Angular current intensity is given by $I' = I_p/\Omega$, where I_p is the current transmitted through an aperture Ω. The beam intensity I' is held constant as we

compare various properties of the emitters. For the study we take I' =1mA/sr.

Table 6 shows the standard geometry and voltages used in this study. Only the values being varied will be mentioned in the following calculations, experiments and graphs. For a fixed I' , the extraction voltage V_E, surface field F and J are functions of emitter radius as shown in Table 7. It is apparent that as r decreases F and J increase while V_E decreases as shown in Fig.6-5 and 6-6. It can be shown that

$$I' = K\ J\ r^2 = \frac{J\ r^2}{m^2} \tag{6-15}$$

where $K \sim$ 23.8, 20.3, 17.7 for r=0.3, 1.0, 3.0 μm respectively for the ZrO/w emitter with V_E=6kV and V_S=-300V and $K \sim$ 15.7, 11.4, 8.4 for r=100Å, 500Å, 700Å respectively for the built-up emitter with V_E=6kV and V_S=-300V.

6.4 Aberration coefficients and virtual source size

Using the longitudinal aberration equations we calculated the spherical and chromatic aberration coefficients for emitters with different radii. The virtual source size was obtained by assuming that the energy spread $\Delta E \approx 1eV$ as obtained from previous experimental results[32] .

For the built-up emitters the C_S values obtained from cold-electron and α-electron calculations are quite similar. However, they differ for ZrO/W emitters (i.e. C_S=.0182mm for cold-electron, but C_S=.0513mm for α-electron at r=1μm and V_E=6kV). One reason for this may be that the faceted shape of the ZrO/W emitter has off axis geometrical aberrations. Table 8 and Figs.6-7 and 6-8 show the general trends of C_S and C_C versus emitter radius for the two emitter end forms.

The virtual source size versus aperture angle results are shown in figs.6-9 and 6-10. Only the chromatic aberration coefficient is sensitive to the emitter radius. The

Table 6

Standard geometrical parameters used in all following calculations except that specially mentioned

	ZrO/W (100) (ϕ=2.8eV)	W (100) Built-up (ϕ=4.5eV)
r (μm)	1.	0.070 (R=.50μm)
V_E (kV)	6.0	6.8
V_S (V)	-300.	-300.
Protrusion (mm)	0.250	0.250
Spacing (mm)	0.508	0.508
Bore radius (mm)	0.190	0.190
Initial aperture angle (mrad.)	2.2	2.2
Temperature (K)	1800.	1800.
F (V/Å)	0.069	0.739

Table 7

Extraction voltage V_E, surface field F and current density J values for a constant angular intensity $I' = 1$mA/sr for the two emitter shapes as a function of r (at T=1800K)

	ZrO/W			W Built-up		
r (μm)	0.3	1.0	3.0	0.005	0.010	0.070
V_E (kV)	4.0	6.0	7.0	2.8	3.5	6.8
F (V/Å)	0.111	0.069	0.036	0.84	0.74	0.54
J(A/cm^2)	3.85×10^4	0.53×10^4	0.10×10^4	1.67×10^8	0.60×10^8	0.024×10^8
β (cm^{-1})	2.78×10^3	1.16×10^3	5.14×10^2	3.0×10^4	2.1×10^4	7.9×10^3
m	0.216	0.248	0.257	0.217	0.244	0.343

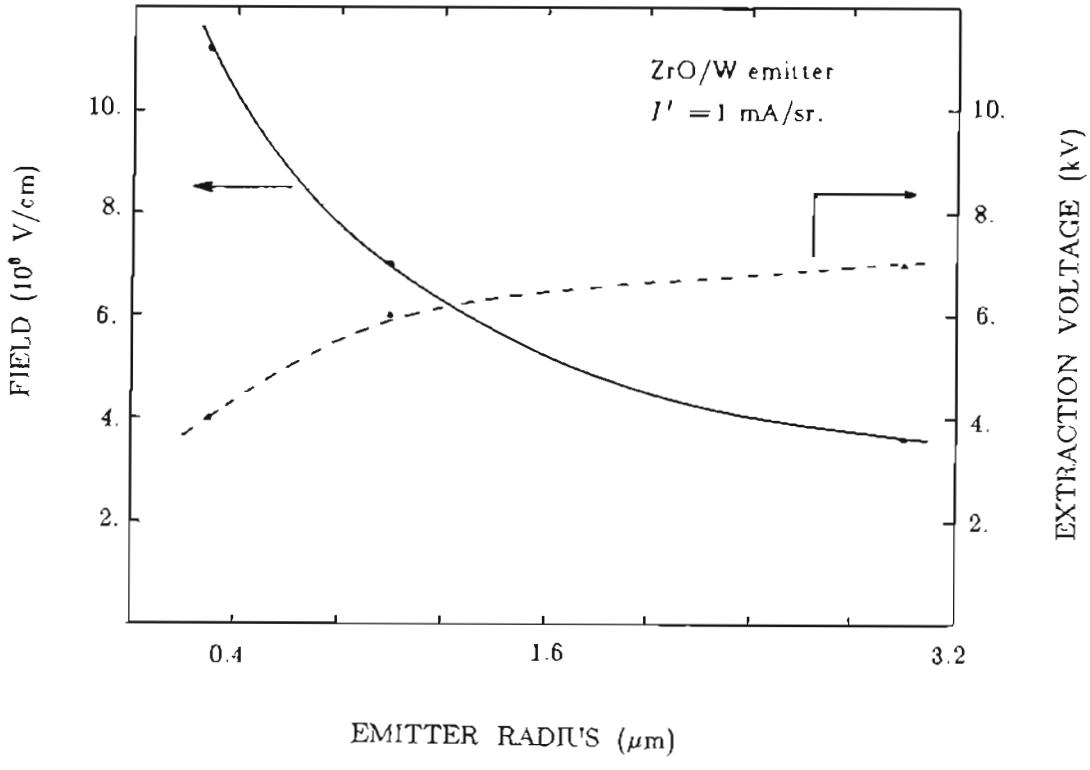

Fig.6-5 : Emitter surface field strength and applied extraction voltage versus the emitter radius at I' =1mA/sr. for the ZrO/W emitter.

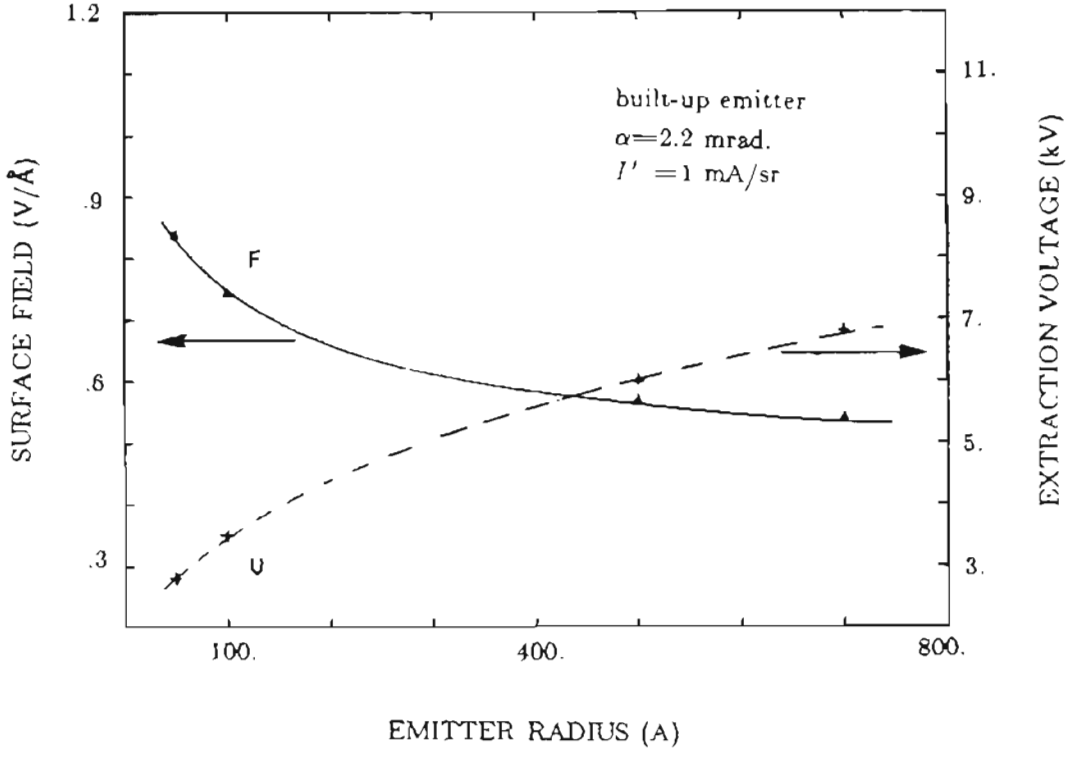

Fig.6-6 : Emitter surface field strength and applied extraction voltage versus the emitter radius at $I' = 1$mA/sr. for the built-up emitter.

Table 8

Effect of emitter radius on aberration parameters

	ZrO/W			W Built-up		
r (μm)	0.3	1.0	3.0	0.005	0.010	0.070
V_E (kV)	4.0	6.0	7.0	2.8	3.5	6.8
C_S (mm)	0.057	0.051	0.062	0.050	0.055	0.034
C_C (mm)	0.241	0.147	0.090	1.255	1.012	0.283
d_g (Å)	18.2	58.0	170.2	0.30	0.54	2.8
d_C (Å)	1.3	0.53	0.28	4.06	3.27	0.91
d_S (Å)	0.003	0.0027	0.0032	0.0026	0.0029	0.0018
d_d (Å)	108.	88.	81.	120.	91.	82.
m	0.216	0.248	0.257	0.217	0.244	0.343

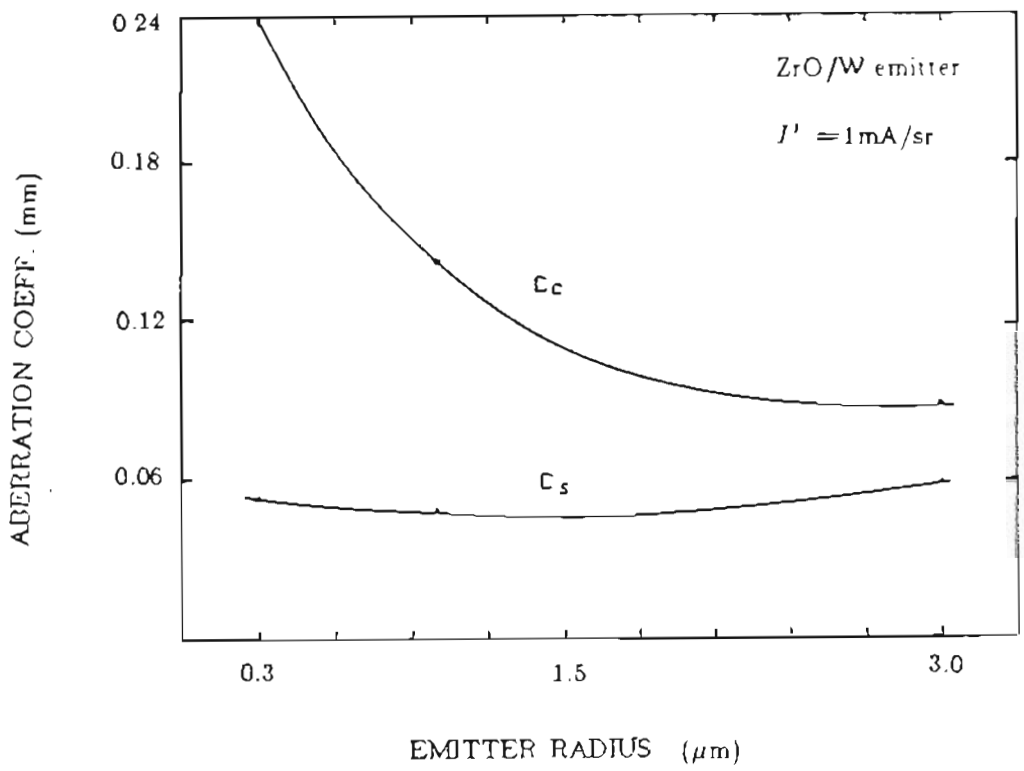

Fig.6-7 : Cathode aberration coefficients C_C and C_S versus emitter radius r for the ZrO/W emitter.

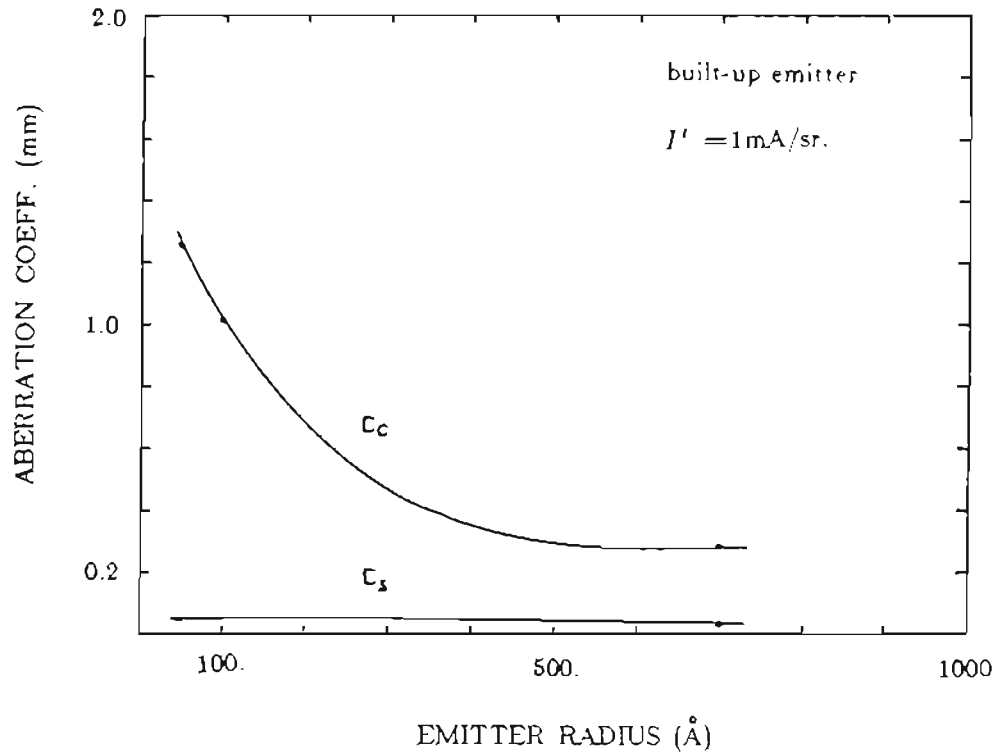

Fig.6-8 : Cathode aberration coefficients C_C and C_S versus emitter radius r for the built-up emitter.

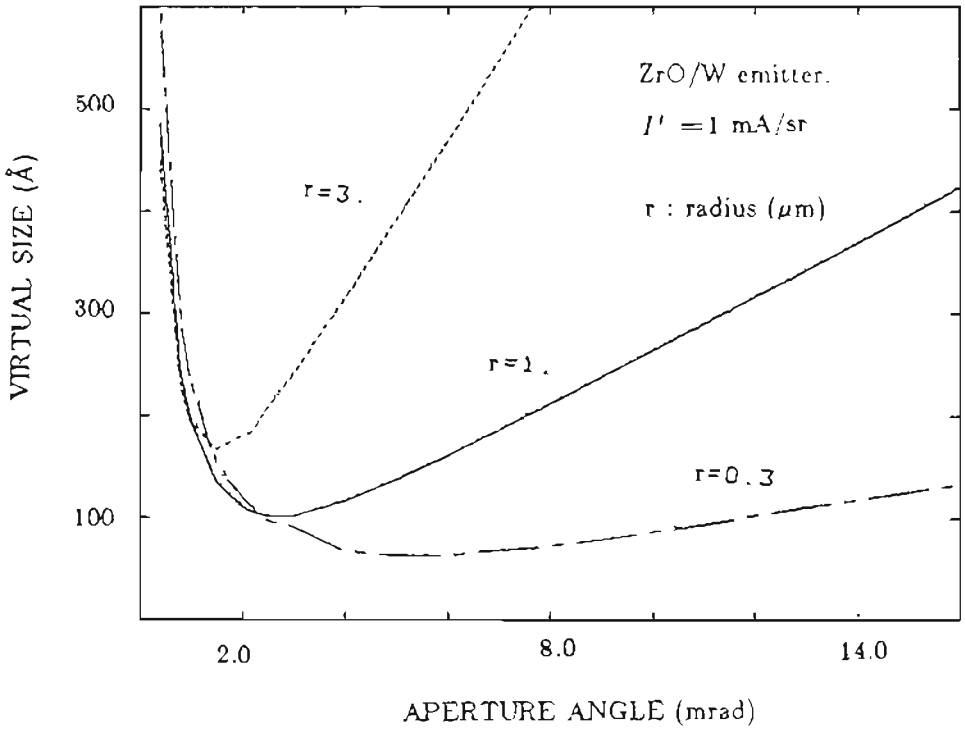

Fig 6-9 : Virtual source size versus aperture half angle for various emitter radii for the ZrO/W emitter.

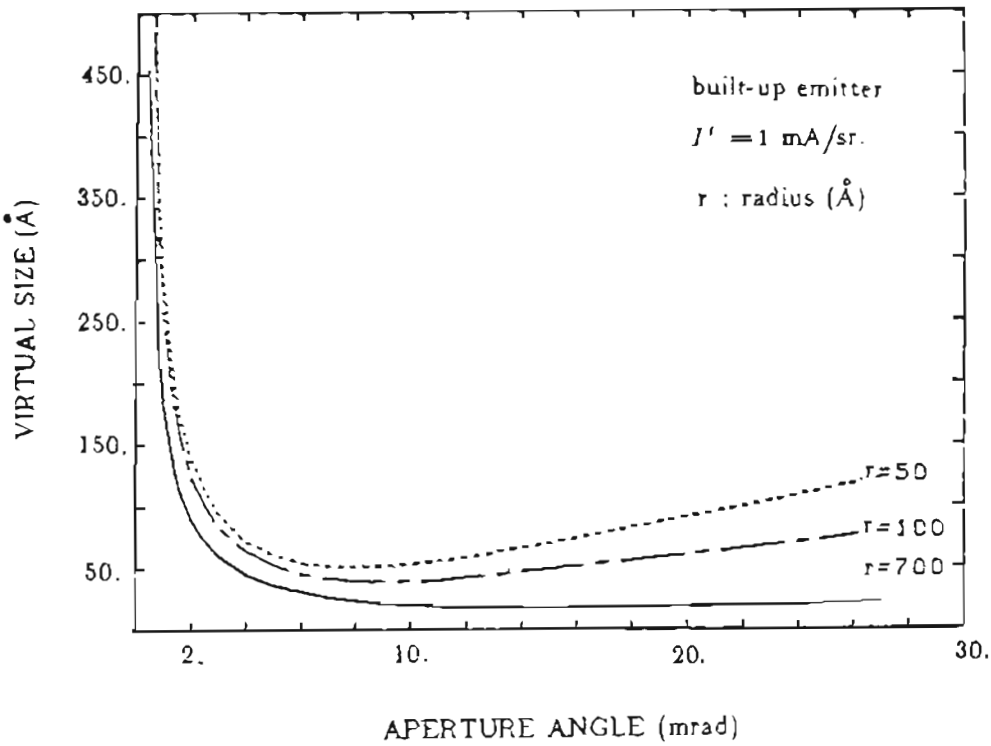

Fig.6-10 : Virtual source size versus aperture half angle for various emitter radii for the built-up emitter.

spherical aberration coefficient remains nearly constant with varying radius. However, the Gaussian source size r_g varies with r since

$$r_g = 0.9539\, Mr\, \tan\frac{\alpha_i}{m} \tag{6-16}$$

which is the same as Eq.(6-11). The r_g plays an important role on the virtual source size d_v. Figs.6-11 and 6-12 show the different contributions to the virtual source from the Gaussian size d_g, the spherical aberration d_s, the chromatic aberration d_c and the diffraction aberration d_d. Apparently, the main contributions come from d_g and d_d depending on the aperture angle.

6.5 Influence of gun structure parameters

Other geometrical parameters of the gun (refer to Fig.5-4 and Table 6) having some influence on the aberration coefficients and virtual sizes are the emitter protrusion from the suppressor, the spacing between emitter and anode, and the anode bore radius as shown in Tables 9, 10 and 11. Figs.6-13 to 6-16 show the effect of emitter protrusion from the suppressor on C_S, C_C and virtual source size d_V. The main influence is on C_C and in general longer protrusion leads to smaller C_C and C_S and smaller virtual source size.

Figs.6-17 to 6-20 show the effect of spacing between emitter and anode. The C_C values are mainly affected, but it leads to negligible difference of the virtual source size. This is a desirable result since one can choose a suitable spacing between emitter and anode to obtain desired emission current and operating voltage.

If the emitter-to-anode spacing is increased and V_E is increased in such a way as to keep the field on the emitter constant, the following expression for the source angular magnification m_s is obtained

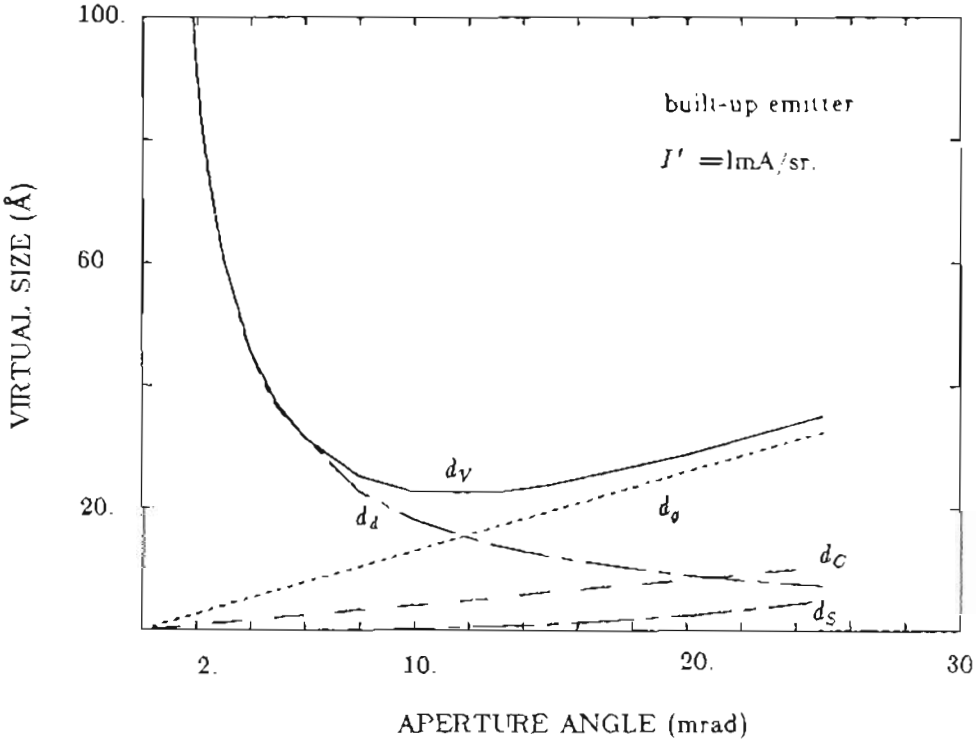

Fig.6-11 : Virtual source size d_V versus aperture angle with different contributions from Gaussian size d_g, spherical aberration d_S chromatic aberration d_C and diffraction aberration d_d for the built-up emitter with r=.07μm, I' =1mA/sr, V_E=6.8kV.

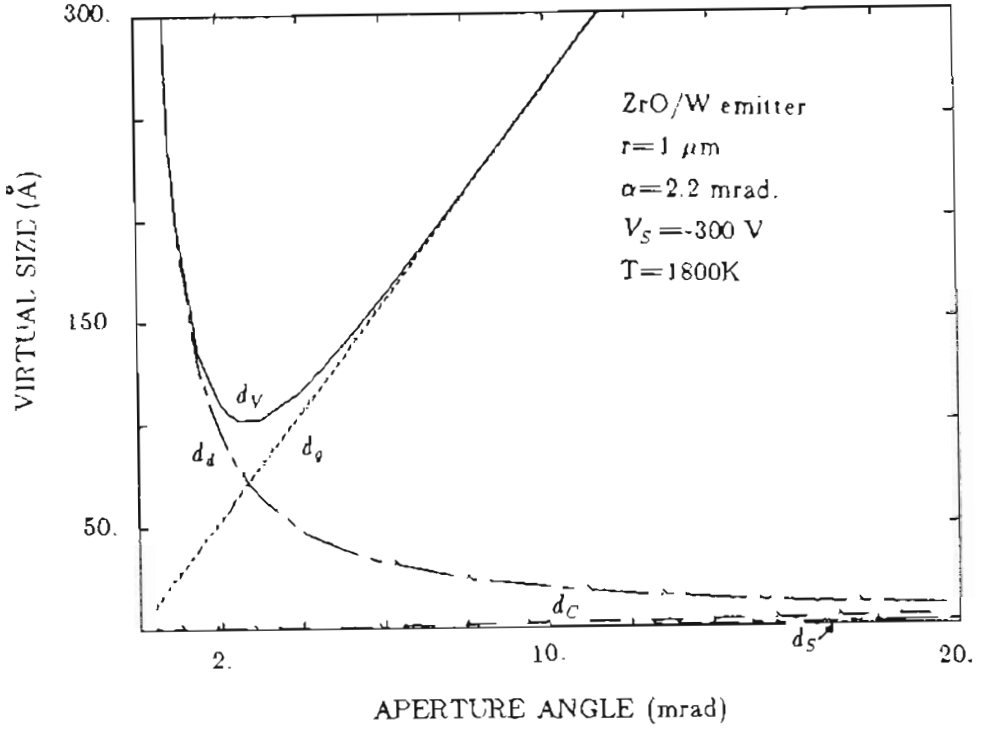

Fig.6-12 : Virtual source size d_V versus aperture angle with different contributions from Gaussian size d_g, spherical aberration d_S chromatic aberration d_C and diffraction aberration d_d for the ZrO/W emitter with r=1.μm, I' =1mA/sr, V_E=6.kV. d_S and d_C is small.

Table 9

Effect of emitter protrusion from the suppressor on aberration parameters

($I' = 1.\text{mA/sr}$)

	ZrO/W			W Built-up		
g (mm)	0.127	0.254	0.381	0.127	0.254	0.381
V_E (kV)	8.0	6.0	5.0	9.2	6.8	5.65
F (V/Å)	0.061	0.069	0.069	0.516	0.539	0.538
C_C (mm)	0.271	0.147	0.059	0.651	0.283	0.140
C_S (mm)	0.093	0.051	0.032	0.078	0.034	0.021
d_g (Å)	74.0	58.0	54.4	3.4	2.8	2.8
d_C (Å)	0.74	0.53	0.25	1.5	0.91	0.54
d_S (Å)	0.005	0.003	0.002	0.004	0.002	0.001
d_d (Å)	76.	88.	96.	71.	82.	90.
m	0.201	0.248	0.260	0.300	0.343	0.377

Table 10

Effect of spacing between emitter and anode on aberration parameters

($I' = 1\text{mA/sr}$ $V_S = -300$ V)

	ZrO/W ($\phi = 2.8eV, r = 1.\mu m$)			W built-up ($\phi = 4.5eV, r = .07\mu m$)		
L (mm)	0.254	0.508	0.762	0.254	0.508	0.762
V_E (kV)	4.5	6.2	7.8	4.6	6.8	8.9
F (V/Å)	0.079	0.072	0.067	0.551	0.540	0.525
C_C (mm)	0.028	0.147	0.593	---	0.283	1.077
C_S (mm)	0.016	0.051	0.102	0.009	0.034	0.118
d_φ (Å)	52.0	58.0	62.0	2.6	2.8	3.2
d_C (Å)	0.15	0.53	1.60	---	0.97	2.60
d_S (Å)	0.001	0.003	0.005	0.001	0.002	0.006
d_d (Å)	100.	88.	76.	100.	82.	72.
m	0.291	0.248	0.219	0.400	0.343	0.310
J (A/cm^2)	8.28×10^3	5.94×10^3	4.71×10^3	3.06×10^6	2.42×10^6	1.76×10^6

Table 11

Effect of anode bore radius on aberration parameters

(I' =1mA/sr)

	ZrO/W			W Built-up		
R (mm)	0.1	0.191	0.3	0.1	0.191	0.3
V_E (kV)	6.0	6.0	6.0	6.8	6.8	6.8
F (V/Å)	0.070	0.069	0.068	0.543	0.530	0.543
C_C (mm)	0.281	0.147	0.055	0.498	0.283	0.248
C_S (mm)	0.074	0.051	0.048	0.056	0.034	0.031
d_g (Å)	58.0	58.0	57.5	3.0	2.8	2.8
d_C (Å)	1.0	0.53	0.20	1.60	0.91	0.80
d_S (Å)	0.004	0.003	0.003	0.003	0.002	0.002
d_d (Å)	88.	88.	88.	82.	82.	82.
m	0.237	0.248	0.238	0.348	0.343	0.348

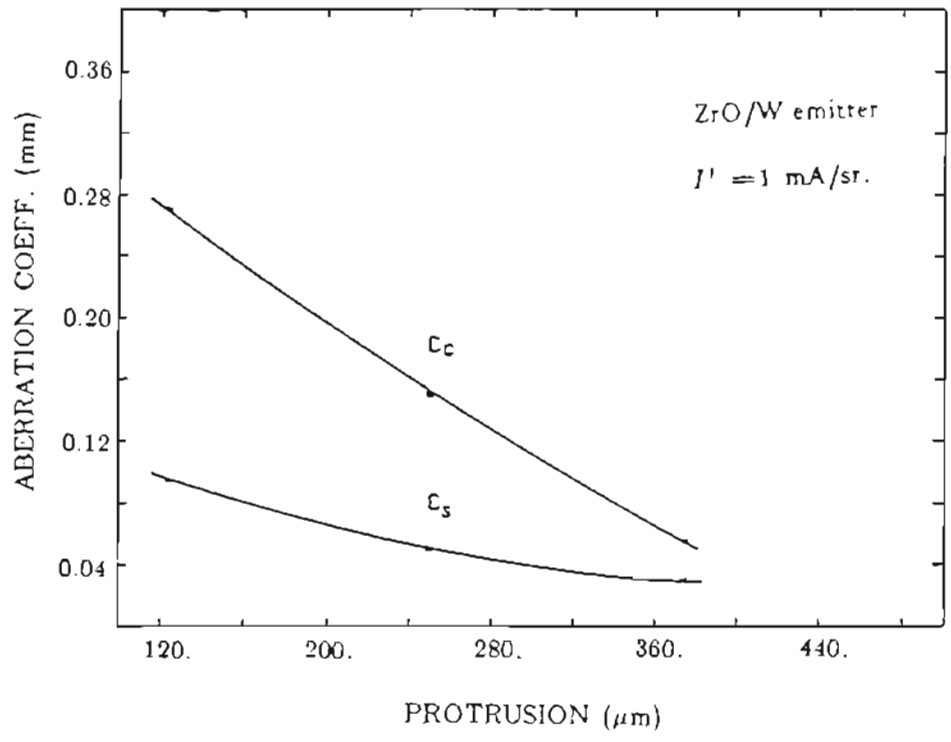

Fig.6-13 : Cathode aberration coefficients versus emitter protrusion from the suppressor for the ZrO/W emitter.

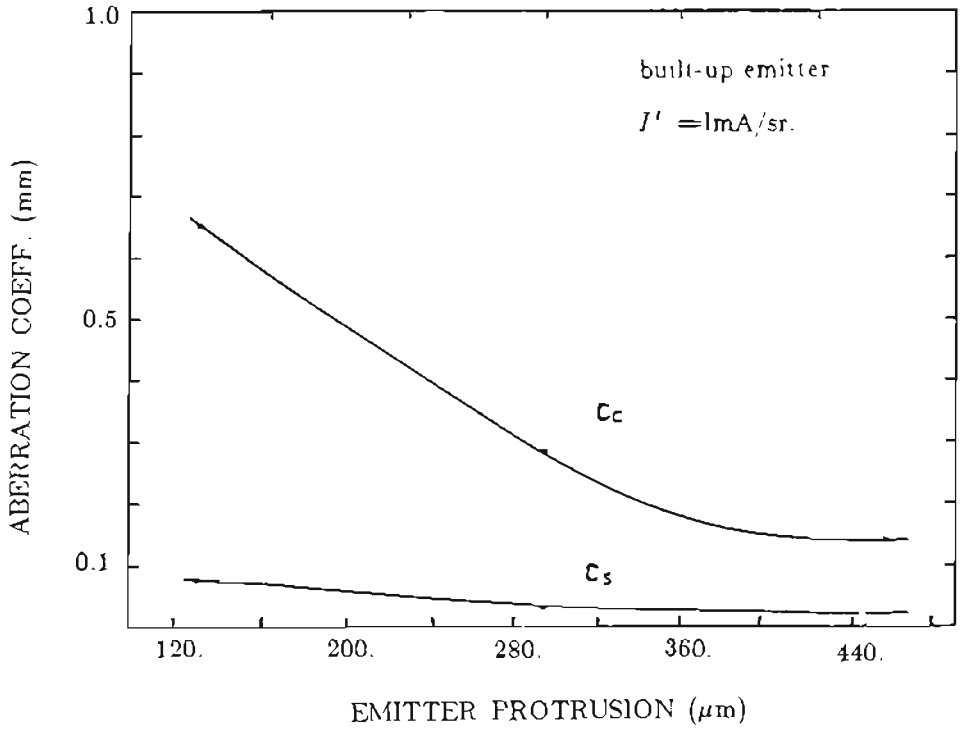

Fig.6-14 : Cathode aberration coefficients versus emitter protrusion from the suppressor for the built-up emitter.

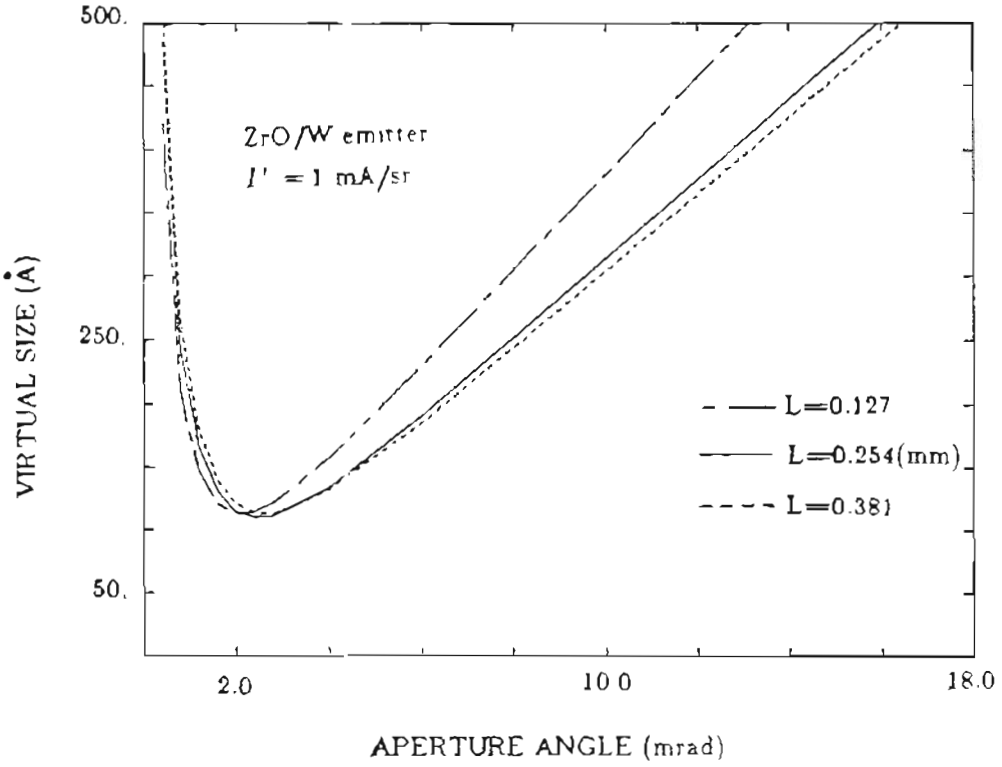

Fig.6-15 : Virtual source size versus aperture half angle for various emitter protrusions for the ZrO/W emitter.

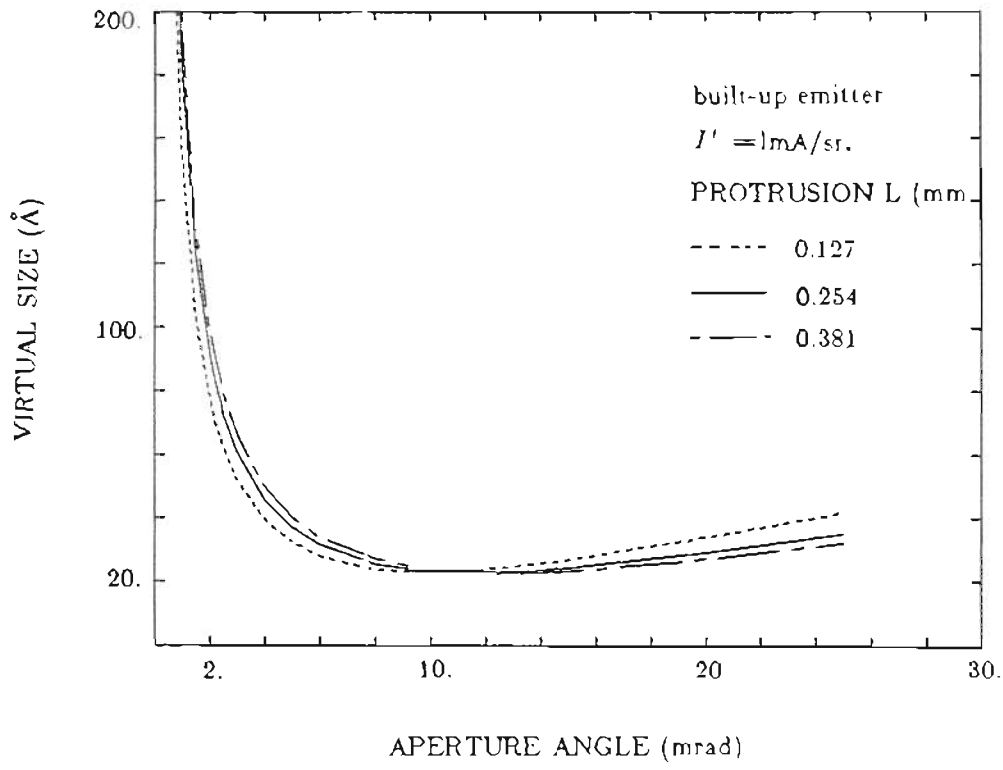

Fig.6-16 : Virtual source size versus aperture half angle for various emitter protrusions for the built-up emitter.

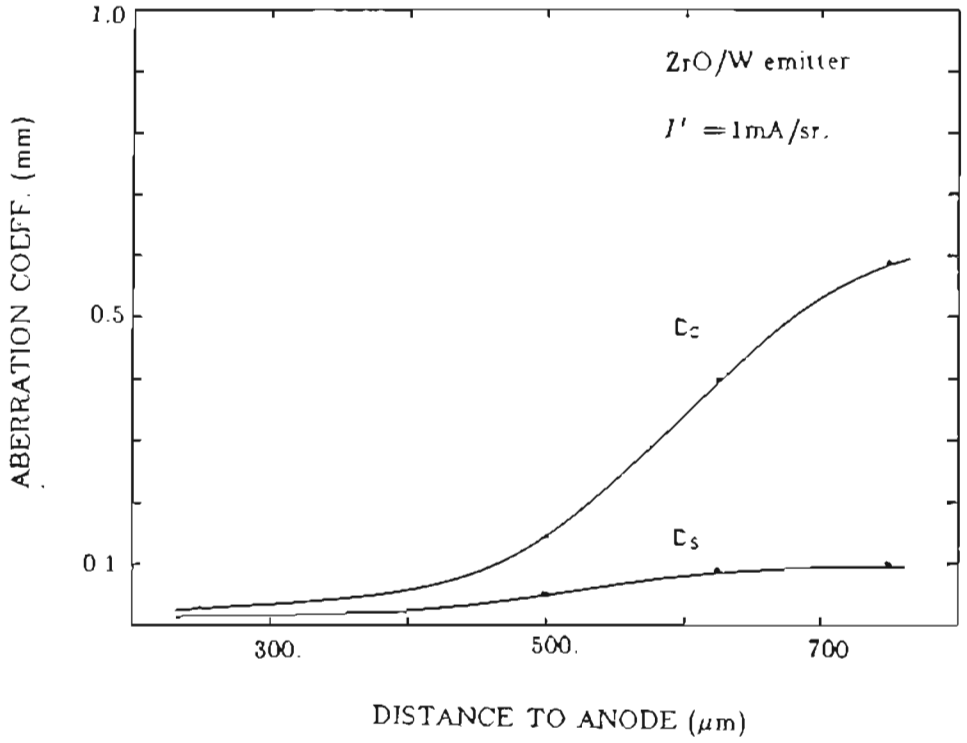

Fig.6-17 : Cathode aberration coefficients versus spacing between emitter and anode for the ZrO/W emitter.

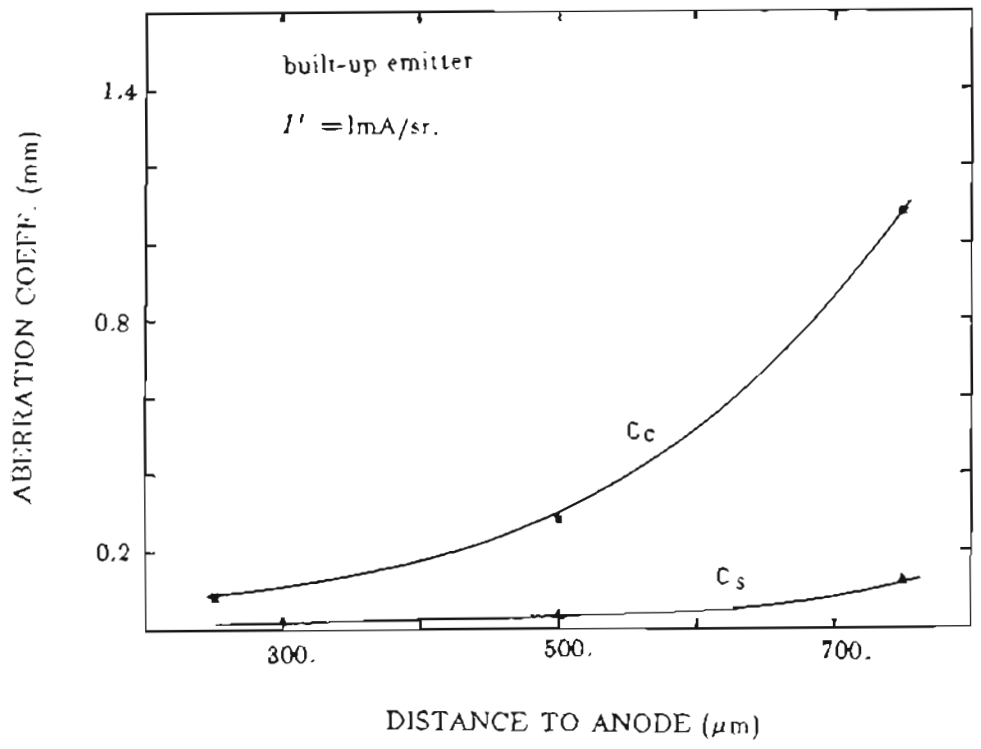

Fig.6-18 : Cathode aberration coefficients versus spacing between emitter and anode for the built-up emitter.

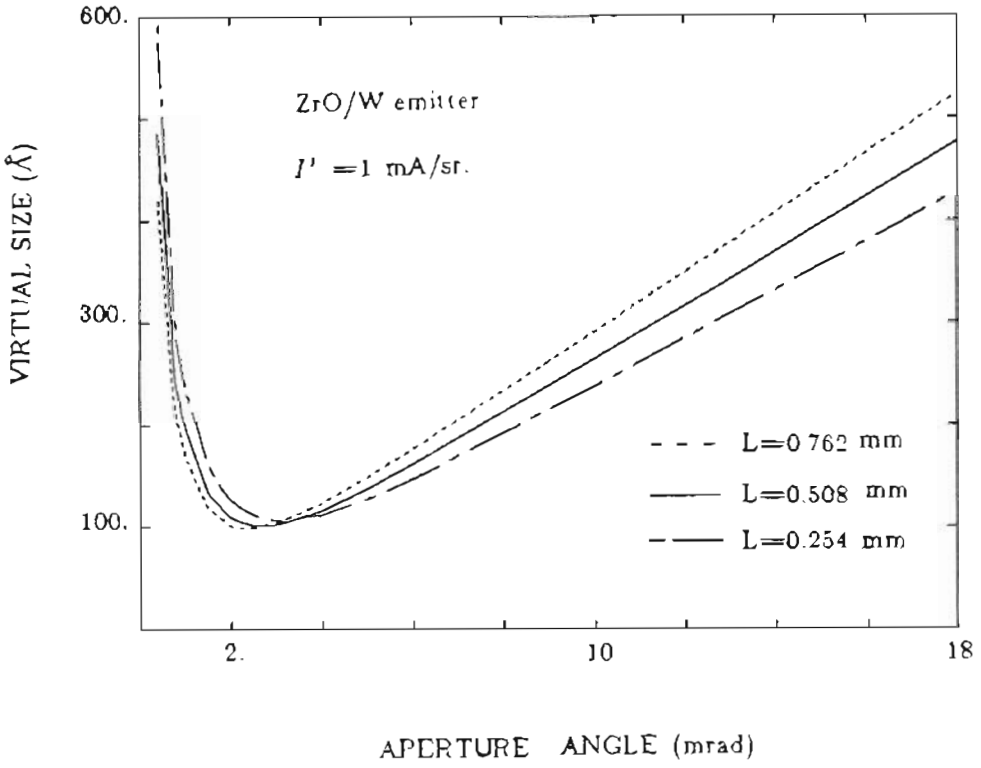

Fig.6-19 : Virtual source size versus aperture half angle at various values of spacing L between emitter and anode for the ZrO/W emitter.

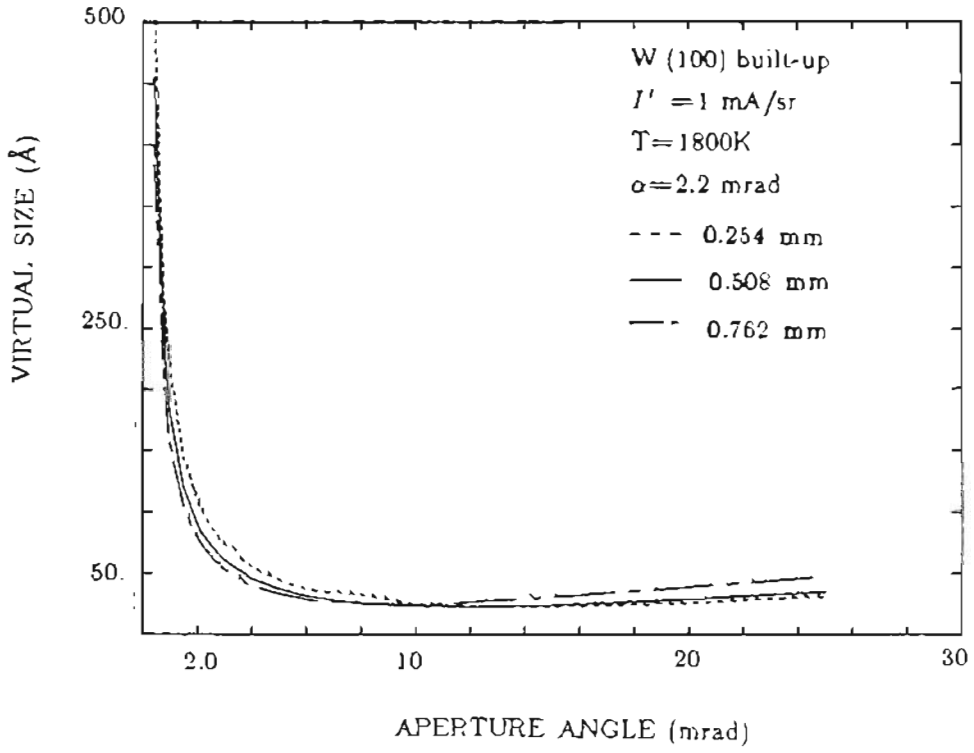

Fig.6-20 : Virtual source size versus aperture half angle at various values of spacing L between emitter and anode for the built-up emitter.

$$m_s \propto \frac{1}{V_E^{1/2}} \propto \frac{1}{L^{1/2}} \qquad (F \text{ constant}) \tag{6-17}$$

where L is the spacing, V_E is the extraction voltage. It indicates that the m decreases with increasing L and V_E. From the source optics Eq.(1-2) the source angular intensity is given by

$$I' = \frac{J_C \, r^2}{m_s^2} \tag{6-18}$$

where J_C is the cathode current density, m_s is the angular magnification in source. Thus, I' increases with decreasing m_s. This provides a way to increase I' by adjusting L and V_E values.

Moreover, if V_E and I' are increased, another advantage appears upon looking at the current density J_i in the image plane of the SEM. In the chromatic aberration limited case Eq.(1-6) for the beam current in the image plane can be simplified as

$$I_P = \frac{d^2}{M^2}\left(\frac{V_E}{C_C \Delta V}\right)^2 \pi I' \tag{6-19}$$

where M is the linear magnification of the optical system, d is the spot size. It can be rewritten as

$$J_i = \frac{I_P}{\pi r_i^2} = \frac{4 V_E^2}{M^2 (\Delta V)^2 C_C^2} I' \tag{6-20}$$

where r_i is the focused spot radius in the image plane, because of the Abbe's sin law

$$M = \frac{\sin\alpha_o}{\sin\alpha_i}\left[\frac{V_E}{V_B}\right]^{1/2} \approx \frac{1}{m_\alpha}\left[\frac{V_E}{V_B}\right]^{1/2} \tag{6-21}$$

combining Eq.(6-17), (6-20) and (6-21) yields

$$J_i = \frac{4 m_o^2 V_B \, V_E \, I'}{(\Delta V)^2 C_C^2} \propto \frac{k_1 m_\alpha^2 J_C \, V_B \, V_E^2}{(\Delta V)^2 C_C^2} \propto \frac{k_2 m_\alpha^2 J_C \, V_B \, V_E \, L}{(\Delta V)^2 C_C^2} \tag{6-22}$$

where k_1 and k_2 are constant. Thus, the current density J_i in the image plane

increases with the values of V_E and L, but m_α, C_C andΔVmay vary, too. All these considerations may be useful for designing a better source and optical system.

Figs.6-21 to 6-24 show the effect of anode bore radius upon aberration coefficients and virtual source sizes. It is shown that C_C varies with bore radius, however, the virtual source size changes little due to the small absolute value of the aberration coefficient. It appears that larger bore radius leads to smaller chromatic aberration coefficients. One favorable effect of a larger bore radius is the reduction of the ion sputtering caused by apertured electrons at the anode. This is helpful for extension of emitter life and reduction of noise level.

It is seen that the C_C and C_S only have a minor contribution to the virtual size compared with Gaussian and diffraction terms, especially for small aperture angles α_0. The optimum operating conditions are collected in Table 12 based on our calculations.

6.6 Space charge effect

Because of the high current density of field emission cathodes, space charge may affect the virtual source calculations. With the aid of the SCWJM program one can determine the effect of space charge.

The space charge effect has been discussed previously in several articles[33,36,40] and can affect both the trajectories and energy spread. The trajectory effects can be divided into two groups: those that depend on the mean charge density and are "deterministic" in nature and those that depend on the charge density fluctuations because of the discreteness of the electron and therefore are "non-deterministic". By "deterministic" we mean that the trajectories are determined a priori.

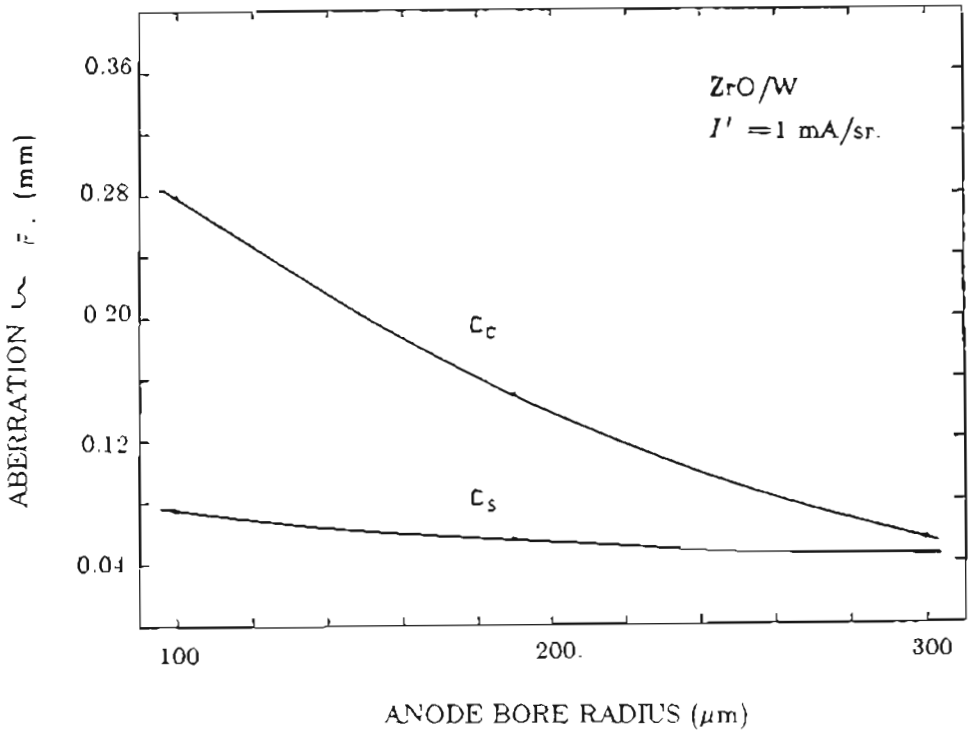

Fig.6-21 : Cathode aberration coefficients versus anode bore radius for the ZrO/W emitter.

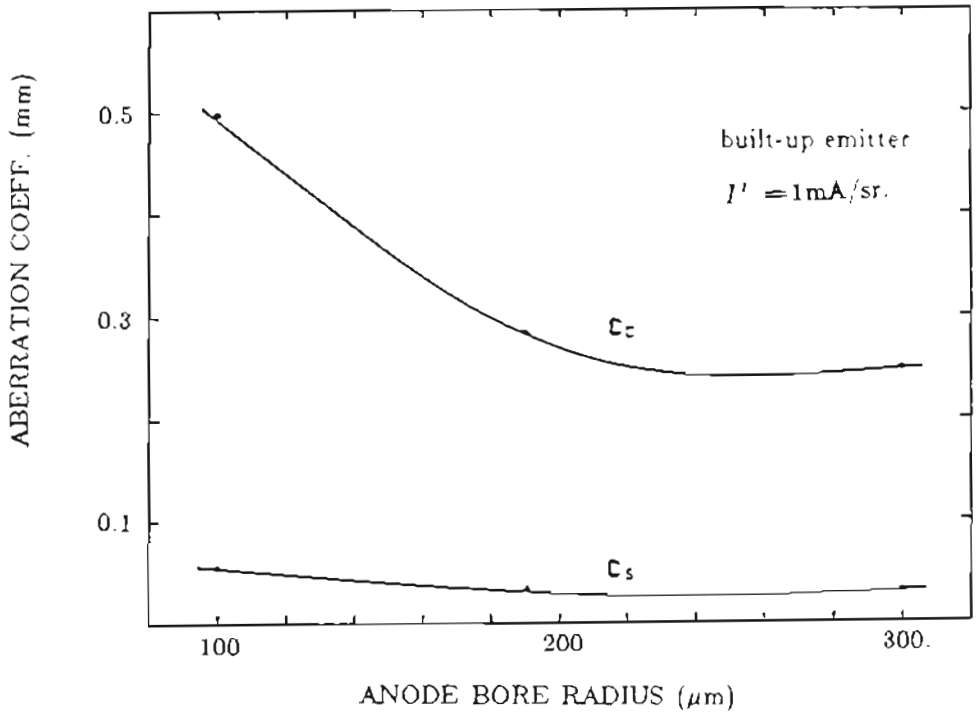

Fig.6-22 : Cathode aberration coefficients versus anode bore radius for the built-up emitter.

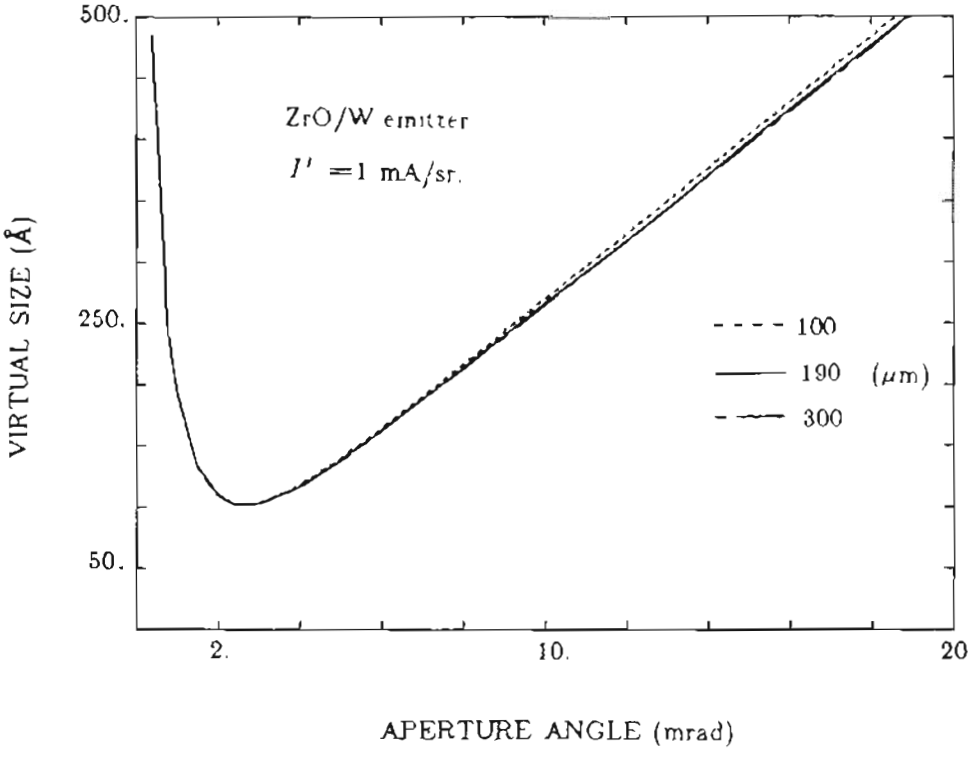

Fig.6-23 : Virtual source size versus aperture half angle for various values of anode bore radius for the ZrO/W emitter.

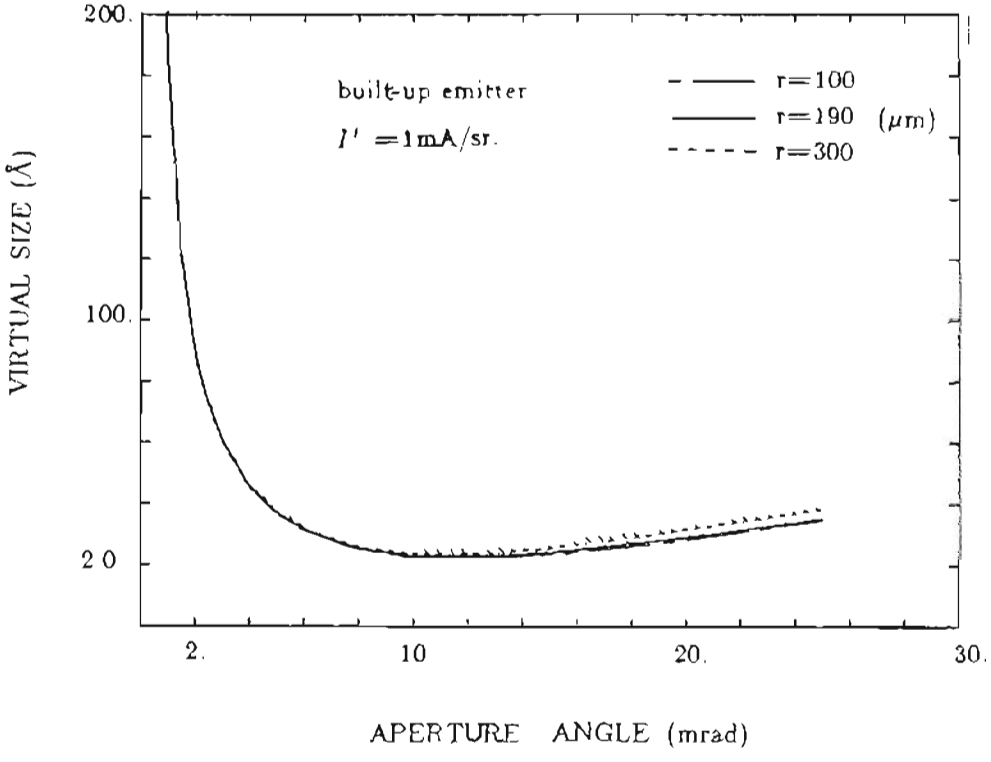

Fig.6-24 : Virtual source size versus aperture half angle for various values of anode bore radius for the built-up emitter.

Table 12

Summary of the optimum operation parameters

emitter radius (μm)	0.5 to 1.0 (for ZrO/W)
	0.01 to 0.1 (for built-up)
protrusion (mm)	0.254 to 0.381
spacing (mm)	0.254 to 0.508
anode bore (mm)	0.150 to 0.250
suppressor voltage (V)	-300 to -500
temperature (K)	1800 to 1850

In the deterministic model Poission's equation was used to obtain the local electric field. Only the radial field E_r alters the electron trajectories. Massey et al[33] showed that the space charge effect would cause an image shift along the Z-axis, i.e. the intersection of trajectory tangents on the Z-axis would move towards to the emitter apex causing an overfocusing. However, in his model the net effect of the axial field on electron energy was shown to be essentially negligible.

The energy distribution is not affected by the continuous charge and therefore is more correctly treated using the statistical, discrete charge model. The emission process introduces a random potential energy into a beam which causes random repulsive forces between electrons. The mean square fluctuation in the longitudinal electric field E_Z can be calculated under some assumptions, such as a uniform random space charge distribution at the cathode and a slowly varying electron number density. Then, the rms field fluctuation $\delta E_Z = <E_Z^2>^{1/2}$ can be obtained. The energy spread ΔV can be found simply by integrating the force δE_Z along the Z direction:

$$\Delta V = e \int \delta E_Z(Z) dZ \tag{6-23}$$

In addition to initial potential energy relaxation, redistribution of the initial electron velocities by electron scattering in the beam produces an energy broadening. Massey proved, for a plane diode, that if the initial energy spread is about 1eV or greater, the statistical chromatic effects due to space charge at the usual current densities will be small compared to the chromatic aberration corresponding to the initial velocity effects alone.

In our study only the continuous charge density that fills the diode space was considered. Thus we consider only the deterministic case. Our calculations indicate, in agreement with Massey's "deterministic" calculations, that the virtual source position shifts slightly toward the emitter apex (see Table 13). Additionally, large increases in

Table 13

Emitter properties with and without space charge

	ZrO/W (ϕ=2.8eV, r =1.μm)		W Built-up (ϕ=4.5eV, r =.07μm)	
	without	with	without	with
C_C (mm)	0.147	3.25	0.283	12.7
C_S (mm)	0.051	0.691	0.034	0.587
d_g (Å)	58.10	56.85	2.99	2.97
Z_V (μm) (from apex)	-31.47	-31.35	-30.56	-30.45
F (V/Å)	0.0695	0.0690	0.540	0.481
J (A/cm^2)	5.29×10^3	5.20×10^3	2.43×10^6	2.33×10^6
I' (mA/sr)	0.974	0.967	1.046	0.972
m	0.248	0.239	0.348	0.346

C_C and C_S are observed due to the space charge, but since the Gaussian source size d_g is dominant for aperture angles less than 10 mrad. (see Figs. 6-25 and 6-26), these increases do not significantly affect the virtual source size.

By solving the Poisson equation the SCWIM program can be used to estimate the deterministic effect of space charge. In order to calculate space charge numerically an iteration procedure was carried out. First, the Laplace equation, $\nabla^2 V = 0$ is solved, from which the emission current density J is calculated using the numerical integration method mentioned in section 2.2. Trajectories are then computed by integrating the equation of motion. Trajectories starting from the emitter surface are assumed to fill a region of space with electron charge. To simplify the process if the current carried by the trajectory which falls in the i-th auxiliary mesh cell is I_i, the time Δt for the electron to pass through the mesh cell and the volume element Δv_i are known, the space charge density ρ at mesh point can be expressed as

$$\rho = \sum_i I_i \ \Delta t_i / \Delta v_i \tag{6-24}$$

By substituting ρ into the Poisson equation, $\nabla^2 V = -\rho/\epsilon_0$, a new field map can be generated and the cycle is repeated until self-consistency is achieved.

The overall consequence of including the effect of a space charge continuum on the minimum value of d_V is negligible, although the summary in Table 13 shows a substantial change in C_C and C_S. The effect on the primary contribution to d_V, namely d_g, is small. Since, in principle, the first order effect of space charge on the image should be a displacement on the z axis. We should expect little change in d_V as in the case in Figs.6-25 and 6-26 for two TF emitters.

The results given in Figs.6-27 and 6-28 show that only for the built-up emitter is there a perceptible change in J due to space charge. This is an expected result since $J_{built-up} / J_{ZrO/W} \sim 10^3$. Should a smaller radius ZrO/W emitter be used, the current

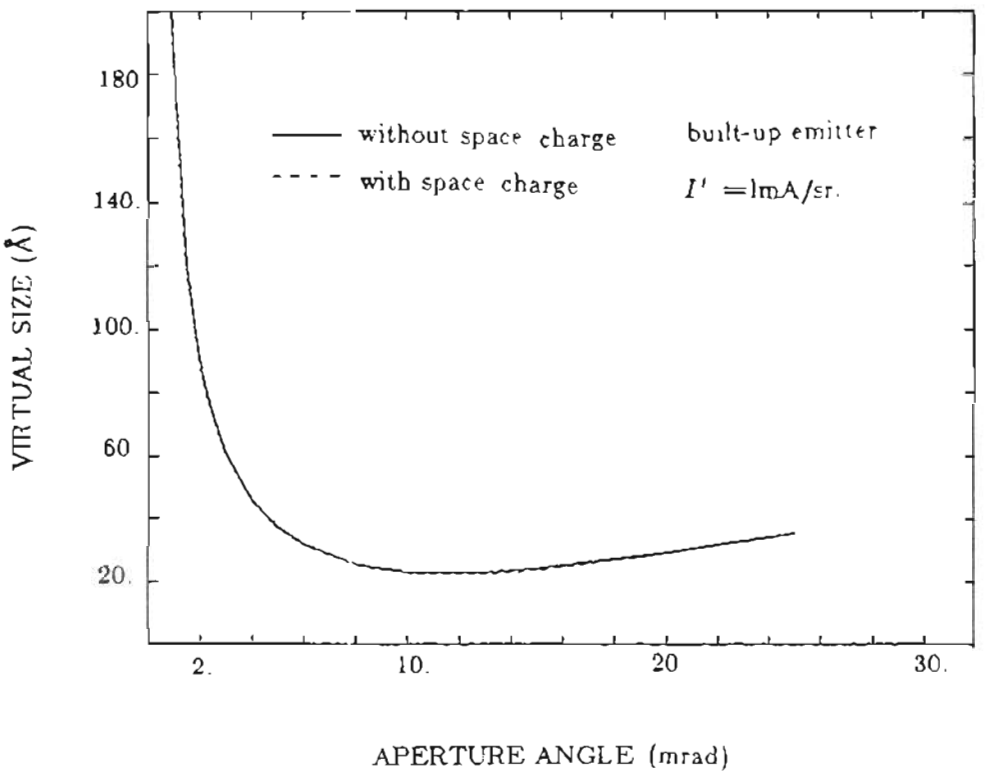

Fig.6-25 : Virtual source size versus aperture half angle with and without inclusion of space charge for the ZrO/W emitter.

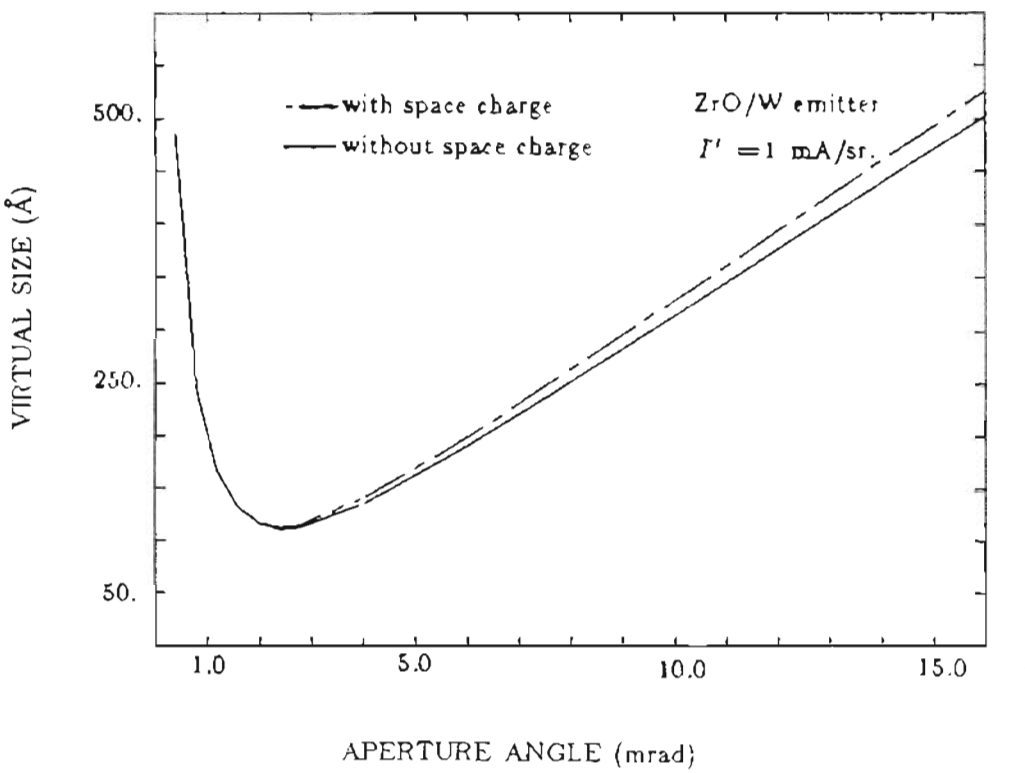

Fig 8-26 : Virtual source size versus aperture half angle with and without inclusion of space charge for the built-up emitter.

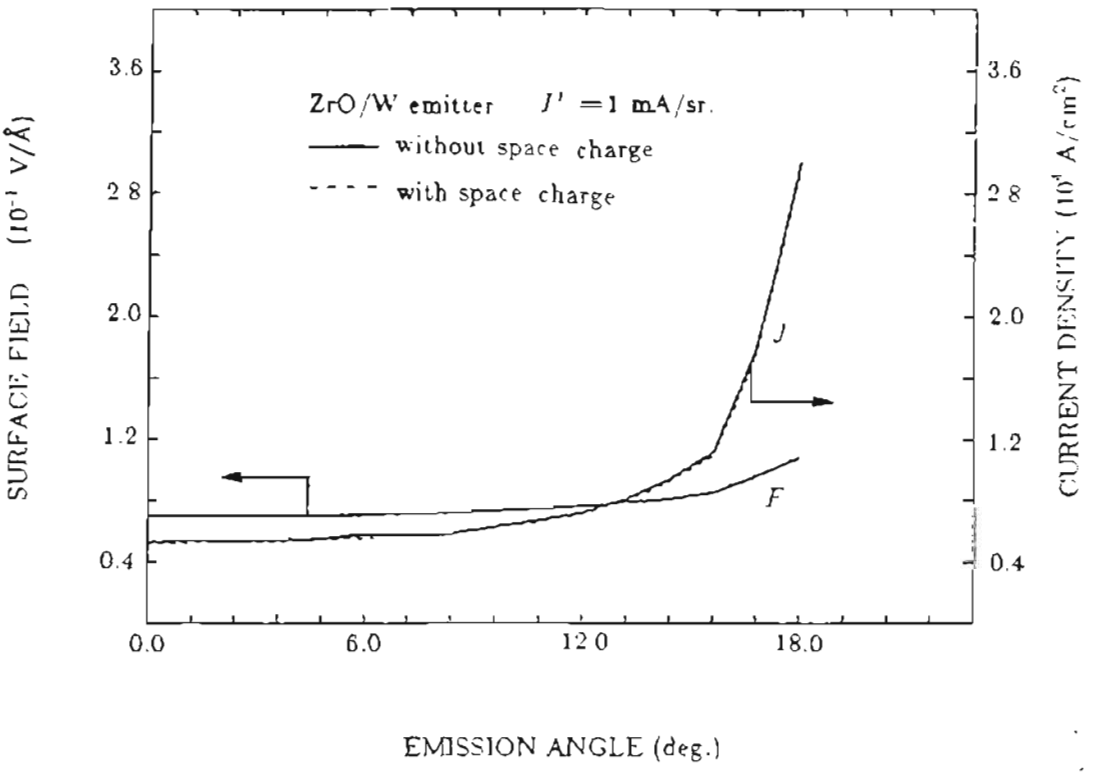

Fig.6-27 : Surface field strength and current density variation with emission angle with and without space charge for the ZrO/W emitter.

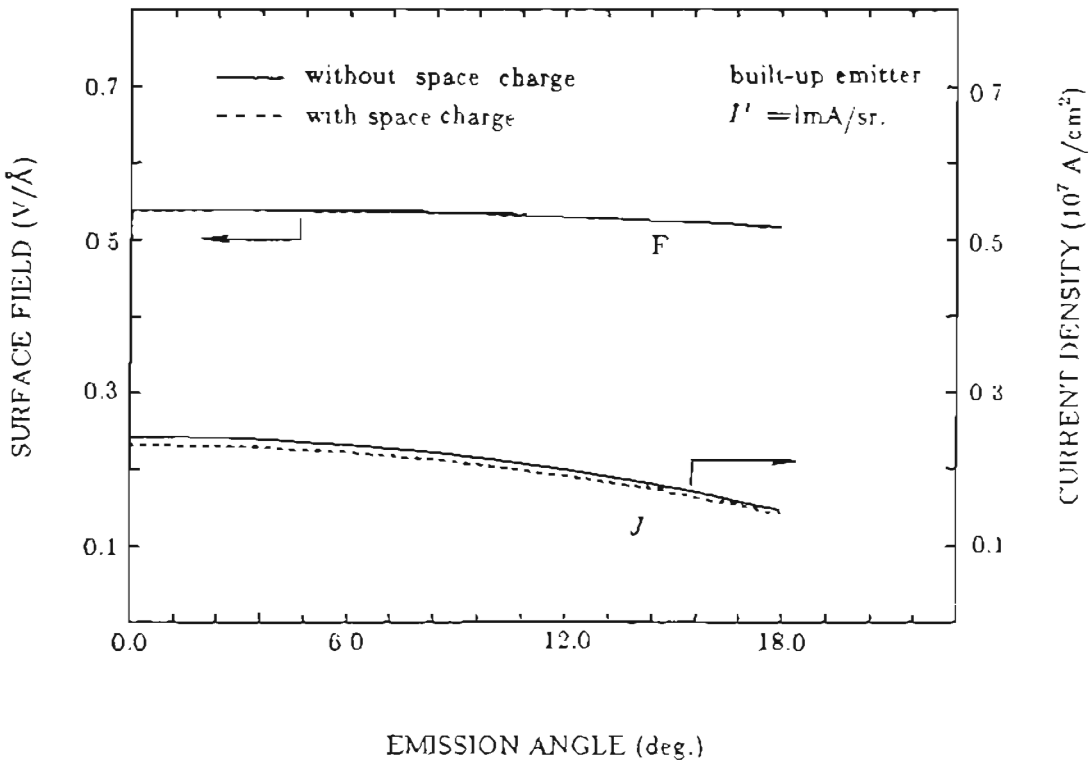

Fig.6-28 : Surface field strength and current density variation with emission angle with and without space charge for the built-up emitter.

density for a constant I' increases as r^{-2}; thus as shown elsewhere[41] space charge effects can become significant for the ZrO/W emitter if r is $\leq$ 0.3 μm.

Chapter 7

Conclusion

Two types of thermal field emitters, the W (100) built-up emitter and the ZrO/W (100) emitter have been investigated in detail in conjunction with use in a low beam voltage SEM. In general, the ZrO/W emitter is superior to that of the built-up emitter. The following table summarizes the performance of the two type emitters in the C & W SEM operating at a low beam voltage.

Parameters & Properties		ZrO/W (100) (T=1800K)	built-up W (100) (T=1800K)
Work Function ϕ (eV)		2.8	4.5
Emitter Radius r (μm)		0.3 to 1.2	0.01 to 0.1
Brightness (10^8A/cm^{2}sr) at I' ~1mA/sr		2.88 (r=1.μm)	4.62 (r=.07μm)
Spot Size (μm) at V_B/V_E ~.15 or .35	I' =1mA/sr	~0.2	~0.4
	I' =0.1mA/sr	<0.1	~0.2
Noise/Signal 10^{-3} to 25k (Hz) (%)	typical	~0.5%	~5.0%
	with r & α	N/S $\propto r^{-2}\alpha^{-1}$	non-sensitive
	with T	non-sensitive	non-sensitive
Vacuum Requirement (torr)		~2×10^{-8}	~5×10^{-9}
Energy Spread (eV) at I' ~1.0mA/sr		~.7 (r~1.μm)	2. to 2.5 (r~.05μm)
Energy Broadening		low (r is larger)	high (r is smaller)
Radial Broadening		high at high linear magnification	high at high linear magnification
Emitter Life Time		very long (>5000h)	long (>2000h)
Gaussian size (Å) (α=2.2mrad)		~50. (r=1.μm)	~3. (r=.07μm)
Virtual size (Å) (α=2.2mrad)		~105. (r=1.μm)	~83. (r=.07μm)
Minimum Virtual size (Å)		~100. (r=1μm,α=2.5mrad)	~20. (r=.07μm,α=8.mrad)

These properties make the ZrO/W emitter a good candidate for applications in low voltage beam equipment. Mainly, the low work function (ϕ=2.8eV) for ZrO/W allows the emitter radius to be large and it significantly reduces the noise level and the energy broadening. With the emitter geometries normally used and emission levels of ~1.mA/sr the ZrO/W emitter usually operates in the Schottky and extended Schottky emission regimes, while the built-up emitter operates in the thermal field emission regime.

The small virtual source size is the unique feature of point cathodes. The minimum virtual size for the ZrO/W emitter with r=1.μm, α=2.2mrad and I' =1.mA/sr is ~100$\AA$, but, for the built-up emitter with r=0.07μm, α=8.mrad and I' =1.mA/sr is ~20$\AA$. To compare these emitters at equal beam current, and therefore equal α's, the virtual source size for the built-up emitter at α=2.2mrad is ~80$\AA$ which is similar to the ZrO/W emitter.

Because of the high brightness of the source, a high angular intensity with a low beam voltage (around or below 1kV) is readily obtained for the both types of emitters. Also, due to the small virtual source size (<0.015 μm) the electron optical system is relatively simple and there is no need to demagnify the source as in the case in conventional thermionic systems.

The radial broadening is an important contribution to the spot size besides the ordinary spherical aberration, chromatic aberration, diffraction aberration and Gaussian source size. This contribution to the broadening of the spot size is given roughly by $d_b = C_b\ I/\alpha$ with $C_b \propto L/V^{3/2}$. Apparently, high linear magnification (low α), high beam current I and low beam voltage V will cause a large value of d_b. Since it is our desire to gain high beam current and low beam voltage in this SEM attention must be given to the following:

1. Avoid using the high linear magnification (or low angular magnification) region as operating region (e.g. $V_B/V_E \sim 0.2$ to 0.27 in the C & W SEM, though the beam path is in parallel mode and with smallest aberration) because of the dominant effect of the radial broadening.

2. Reduce the low voltage electrons' flight length L by decelerating the beam near the target plane to lower the value of C_b (e.g. put the decelerating electrostatic lens in the lower part of the column).

The ZrO/W thermal field emitter is more suitable for use in a low beam voltage SEM mainly due to its higher brightness and lower noise level than the conventional thermionic or cold field emission cathode. There still are possibilities to improve its performance by column design and technical considerations.

Because the angular magnification changes with the gun structure and the beam voltage can be adjusted independently of the extraction voltage in this column, it is possible to increase the angular intensity by varying the gun geometry (such as extending the spacing between emitter and anode) and increasing the extraction voltage.

The vacuum requirement for the thermal field emitter is much lower than for the cold field emitter ($\sim 1 \times 10^{-9}$torr), but is still higher than for the conventional thermionic emitter ($\sim 10^{-6}$torr). To maintain 1×10^{-8}torr level a routine baking of the gun chamber is necessary every one or two weeks in our C & W SEM. If a good gun vacuum system is designed, the emitter can run continuously once it starts. This will simplify the operational procedure and tremendously increase the up-time of the equipment.

Appendix 1

(SCWIM Program and Application in ZrO/W Gun)

1. Characteristics

1.1 Introduction

A spherical coordinate with increasing mesh scheme called the SCWIM program was developed at OGC[1]. Its main purpose is to calculate the properties of point emission cathodes on arbitrary shaped electrodes regardless of their large geometrical difference between emitter and other electrodes. With the specially designed radial mesh size according to a geometrical series the truncation error in the finite difference formulae is very small. Also, space charge effects are easily incorporated into the analysis.

The SCWIM program is a general name which includes several programs. They are LABGUN, LMIGUN, ZRWGUN etc. Each represents a different emitter and gun geometry:

LABGUN is used for calculating LaB_6 electron guns.

LMIGUN is used for Liquid Metal Ion gun

ZRWGUN is used for ZrO/W thermal field electron gun.

The common part of all SCWIM programs is the potential iteration calculation. Here, a detailed description about program ZRWGUN is given. The basic program concepts and input-output information can be used as references to other SCWIM programs.

1.2 Specification of ZRWGUN program

(1) ZRWGUN program is specified to calculate ZrO/W thermal field electron gun. When the work function Φ is changed, it can be used to calculate the W(100) Built-up field emission gun as well.

(2) The emitter is much smaller than other electrodes. The difference can be as large as a factor of 10^7. The smallest emitter radius we used was 0.005 μm (mainly limited by the computer memory quantity we are allowed to use in the CYBER 175).

(3) By inputing a sphere-on-cone (SOC) model of a common triode-type gun in Fig.A-1 and a few parameters, such as work function Φ and emitter temperature T, one can get the following output information:

Potential values at mesh points between emitter and all electrodes.

Electric field strength on emitter surface.

Emission current density on emitter surface.

Electron trajectories from emitter to the field-free space.

Equi-potential lines in the space.

Angular current intensity.

Virtual source size and gun aberration coefficients.

The space charge effects.

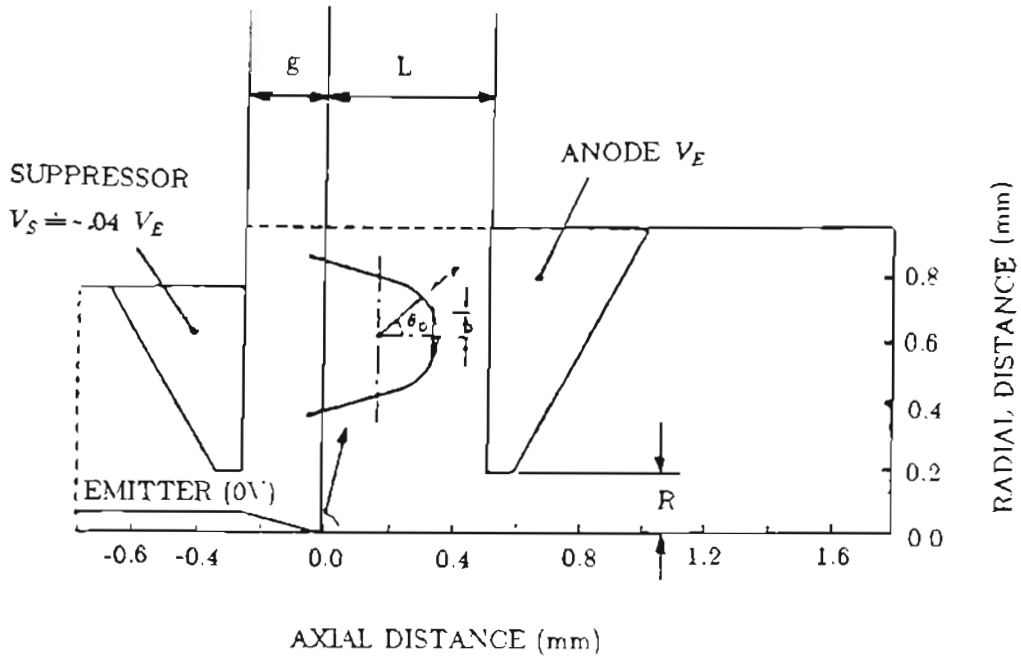

Fig.A-1 : Diagram of electrode configuration used in the gun structure analyzed in this study. Insert shows an expanded view of the emitter apex for the round and faceted cases with radius r. The flat radius is b, the launch angle for electron trajectories is $\theta_0 = 17.5°$.

2. Principle and model description

2.1 SCWIM model

Fig.A-2 shows the definition of terms used in SCWIM model. The minimum radius is R_0. The maximum radius is R_m. To minimize the truncation error for solving differential equation by finite difference method, it is highly desirable to use equidistance difference scheme rather a non-equidistance one. With the former the truncation error is $0(h^4)$ rather than $0(h^2)$ for the latter, where h is the mesh size. With spherical coordinates it is obviously impossible to meet such a demand. But if one chooses that three of four neighboring mesh sizes to be equal, and the other is only alightly larger, the truncation error will be very close to that of the equidistance scheme.

The first mesh size is determined by

$$h_0 = h_\theta \ (h_0 + R_0) \tag{A-1}$$

where h_θ is angular mesh size in radians. In the SCWIM model the three neighboring mesh sizes are taken to be same, i.e. $h_S = h_E = h_W$.

The first mesh size from Eq.(A-1) becomes

$$h_0 = R_0 \ (h_\theta^{-1} - 1)^{-1} \tag{A-2}$$

$$h_1 = h_0 \ (1 - h_\theta)^{-1}$$

$$h_N = h_0 \ (1 - h_\theta)^{-N} \tag{A-3}$$

where N is the total number of mesh points in the radial direction, which can be predetermined from equations (2) and (3) for given R_m, R_0 and h_θ by

$$N = \frac{Ln\,(h_0/R_m\,h_\theta)}{Ln\,(1 - h_\theta)} = \frac{Ln\,(R_0/R_m)}{Ln\,(1 - h_\theta)} \ - 1 \tag{A-4}$$

One can estimates total point number from the equation that the required number of mesh

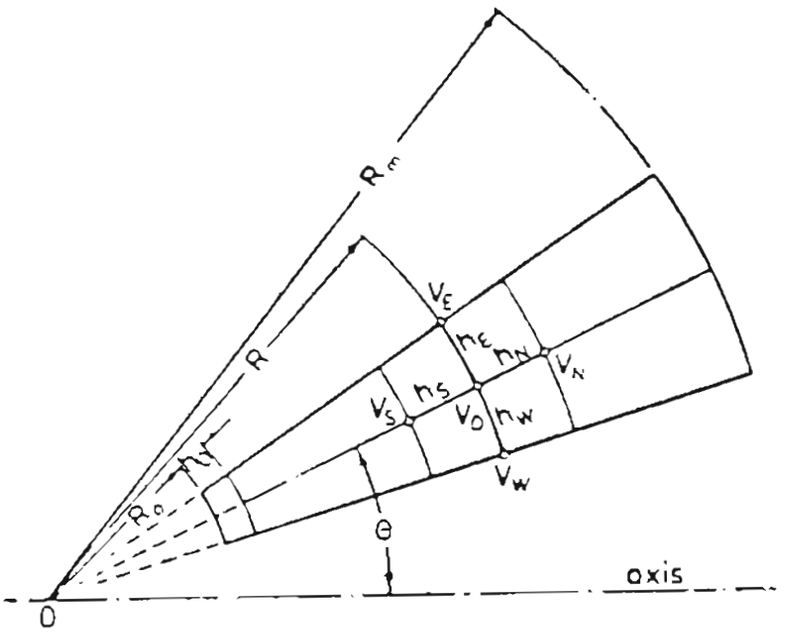

Fig.A-2 : Schematic representation of the mesh arrangement used in the SCWIM method. The minimum and maximum electrode dimensions are R_0 and R_m, respectively

points approximately doubles when the ratio of geometrical sizes increases by two orders (10^2) of magnitude. It is quite economical for computation.

2.2 Difference formulae in SCWIM

By the use of Eq.(A-3) the axisymmetric Poisson equation in spherical coordinates, which is given by

$$\frac{\partial^2 V}{\partial r^2}+\frac{2}{r}\frac{\partial V}{\partial r}+\frac{1}{r^2\tan\theta}\frac{\partial V}{\partial \theta}+\frac{1}{r^2}\frac{\partial^2 V}{\partial \theta^2} = -\frac{\rho}{\epsilon_0} \tag{A-5}$$

can be cast into a five point difference form, which up to the fourth order term of a Taylor series, is given as follows

$$V_0 = B_1\,(1+\frac{h_\theta}{2\tan\theta})V_E + B_1\,(1-\frac{h_\theta}{2\tan\theta})V_W + B_2\,V_N + B_3 V_S + B_4\,\frac{h_S^2\rho}{\epsilon_0} \qquad (off-axis)$$

$$V_0 = B_{10}\,V_E + B_{20}\,V_N + B_{30}\,V_S + B_{40}\,\frac{h_S^2\,\rho}{\epsilon_0} \qquad (on-axis) \tag{A-6}$$

where ρ is space charge density in Coulomb/m^3, ϵ_0 is the permeativity of free space, B_1, B_2, B_3, B_4 and $B_{10}, B_{20}, B_{30}, B_{40}$ are function of h_θ only:

$$B_1 = B_4 = 1/2(1-h_\theta)\,(2+h_\theta)$$

$$B_2 = (1-h_\theta)\,(1+h_\theta)/(2-h_\theta)\,(2+h_\theta)$$

$$B_3 = (1-2h_\theta)/(1-h_\theta)\,(2-h_\theta)\,(2+h_\theta)$$

$$B_{10} = 2/\left[1+(1-h_\theta)\,(2+h_\theta)\right]$$

$$B_{20} = (1-h_\theta)^2\,(1+h_\theta)/\left[1+(1-h_\theta)\,(2+h_\theta)\right](2-h_\theta)$$

$$B_{30} = (1-2h_\theta)/(2-h_\theta)\left[1+(1-h_\theta)\,(2+h_\theta)\right]$$

$$B_{40} = 1/2\left[1+(1-h_\theta)\,(2+h_\theta)\right]$$

This is to say, after h_ϕ is chosen, the B coefficients are constants, a factor which saves considerable computing time in electric potential iterations.

3. Flow chart and algorithm

3.1 Flow chart

The flow chart in Fig.A-3 gives a basic idea about how the program operates.

3.2 Program details and definitions

3.2.1 Input data

The gun geometry and electrode voltage are READ from Tape 7. The program control data are READ from Tape 6. Tape 6 has three forms for the calculation of Cold, Alpha, and V-electrons.

3.2.2 Establish boundaries

Boundary establishment is the most complicated stage because of the various shapes of the emitter and other electrodes.

(a) The emitter tip may be spherical or a faceted shape such as the ZrO/W emitter. The emitter radius RT and the coordinate system origin have to be determined. The center of a nominal spherical emitter tip is taken to be the origin, so the value Z_0 which is the distance from the origin to the emitter apex should be added to the coordinates of node points of the electrodes.

(b) Total mesh point number I_0 and J_0 in the radial and angular directions are determined by Eq.(A-2) and (A-4).

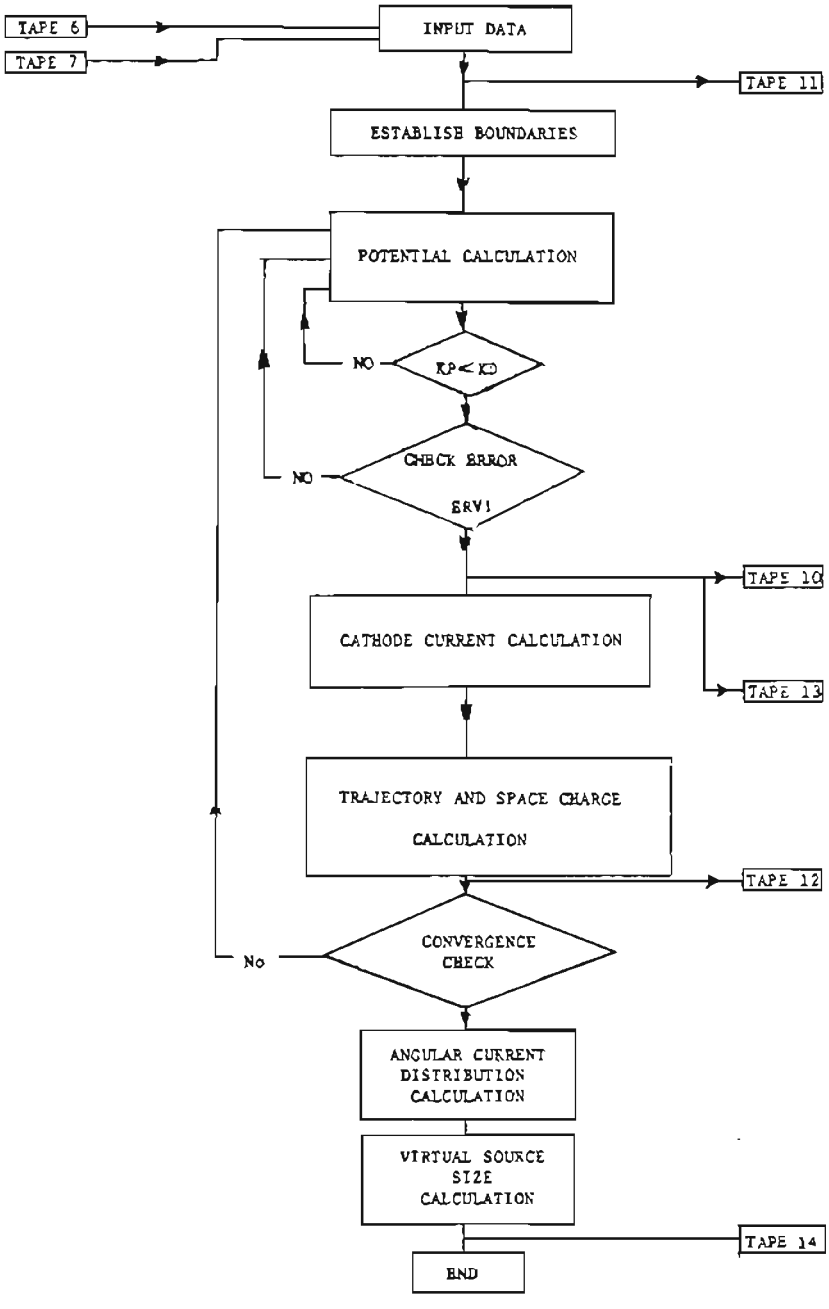

Fig.A-3 : Flow chart of the SCWIM program.

(c) Fine mesh region

A multiple mesh size (or fine mesh) is usually desirable in the vicinity of the emitter and near the axis. This region is bounded by the second node point of cathode. For the faceted ZrO/W emitter the emission area side length is 0.3 times the tip radius. For spherical emitter (W (100) Built-up) the emission boundary angle is within 17.5^0 which makes the emission area radius 0.3 times the tip radius. The multiple can be chosen from 3 to 10. Usually 4 is good enough to get accurate solution.

The fine mesh potentials are transferred to coarse mesh region by linear interpolation. The first coarse mesh potential is interpolated from values of two fine mesh points which are located just before and after the coarse point.

(d) Boundary points

The program gives mesh points inside electrodes the potential equal to the voltage of electrodes, gives mesh point between electrodes the potential by linear interpolation along z direction, and logarithmatic interpolation along r direction due to that the potential varys logarithmatically inside two coaxial cylinders.

The non-normal points which do not take part in iteration have two groups according to their entering or outcomming from electrodes:

IU and IU1 are the nearest mesh number outside the electrodes.

IC0 and IC1 are the mesh numbers in which the boundary points have one surrounding mesh point locating inside electrode at least. So, the points from IU-IC0 and IC1-IU1 do not attend iterations, instead, a interpolation method is used.

3.2.3 Potential calculation

The well-known overrelaxation technique is used for calculation of the potential[42]. The potential, both in the fine and coarse mesh region, are calculated by Eq.(A-6) , in which B_1 and B_{10} etc. are only functions of angular mesh size h_θ. The potential on every point depends on the values of its surrounding four points. To reduce the truncation error a "successive overrelaxation" method is used. After each calculated potential $\Phi^{(k)}$, a new potential value

$$V^{(k)} = C\ \Phi^{(k)} + (1-C)\ V^{(k-1)} \tag{A-7}$$

is used for next calculation, where C is relaxation factor. It can be proved that the optimum value of C is about 1.90.

The minor iteration are performed 19 times (if KP<19, where KP is a controlling integer in the program) and then the truncation error is judged

$$ERV^{(k)} = Max\left[\ 1-\frac{V_n^{(k-1)}}{V_n^{(k)}}\ \right] \qquad n = 1,2,\cdots\cdots\ n \tag{A-8}$$

In the fine mesh region if ERV1 $\geq .2\times10^{-7}$, another medium (scale) iteration is needed. This procedure is repeated until the error meets the requirement.

3.2.4 Current density calculation

First, the electric field strength ER and EC in radial and angular directions, respectively, are calculated by a sixteen point interpolation subroutine. Then the normal field EN on the surface is obtained by

$$EN = \sqrt{ER^2+EC^2/R^2} \tag{A-9}$$

where R is distance between the origin and cathode surface.

The value of EN , work fuction Φ and emitter temperature T can be substituted to the transmmission coefficient D(E_N), which is given by Murphy and Good[11] by applying a

parabolic WKB-type approximation to the Schoedinger Equation

$$D(E_N) = \left[1+ \exp\left(4(2m\ |\mu+\Phi-E_N|\ )^{1/2} v(y)/3\ h\ e\ F\ \right)\right]^{-1} \qquad \text{(A-10)}$$

The free electron model gives the following number of electrons per second per unit area having a normal energy E_N within the range dE_N incident upon the barrier:

$$N(E_N) = (4\pi mKT/h^3)\ Ln\ (1+e^{-(E_N-\mu)/KT})\ \ dE_N \qquad \text{(A-11)}$$

so, the current density J is

$$J = \int_0^{\infty}\ e\ N(E_N)\ D(E_N)\ \ dE_N \qquad \text{(A-12)}$$

this integral is calculated numerically by Simpson's rule in a function subroutine DENSIT (EN,Φ,T). The total current is the sum of products of each current density and its associated emission area. The truncation error of current density is judged by ERI (error judgement).

3.2.5 Trajectory calculation

The initial values of trajectory are their radial coordinate, angular coordinate, radial velocity and angular velocity in the vicinity of emitter. They are put in array Y(4).

The trajectories are obtained by solving the equation of motion for electrons.

$$\ddot{r}\ = -\eta\ E_r + r\ \dot{\theta}^2 = -\eta\ \bar{E}_r \qquad \text{(A-13)}$$

$$\ddot{\theta}\ = -\eta\ E_\theta/r - 2\dot{r}\ \dot{\theta}/r\ = -\eta\ \bar{E}_\theta \qquad \text{(A-14)}$$

where $\ddot{r}$ and $\ddot{\theta}$ are the acceleration, E_r, E_θ, $\bar{E}_r$ and $\bar{E}_\theta$ are electric field and equivalent electric field in radial and angular directions, respectively. The Runge-Kutta method is used to solve the above differential equations. The second order equations are first changed to a set of first order equations

$$\dot{v}_r\ = -\eta\ \bar{E}_r(r,\theta) \qquad \text{(A-15)}$$

$$\dot{v}_\theta\ = -\eta\ \bar{E}_\theta(r,\theta) \qquad \text{(A-16)}$$

$$\dot{r} = v_r \tag{A-17}$$

$$\dot{\theta} = v_\theta \tag{A-18}$$

The coresponding difference equations are

$$v_r^{(n+1)} = v_r^{(n)} + \frac{1}{6}(L_1 + 2L_2 + 2L_3 + L_4) \tag{A-19}$$

$$v_\theta^{(n+1)} = v_\theta^{(n)} + \frac{1}{6}(K_1 + 2K_2 + 2K_3 + K_4)$$

$$r^{(n+1)} = r^{(n)} + \frac{1}{6}(N_1 + 2N_2 + 2N_3 + N_4)$$

$$\theta^{(n+1)} = \theta^{(n)} + \frac{1}{6}(M_1 + 2M_2 + 2M_3 + M_4)$$

where

$$N_1 = T\ v_r^{(n)} \tag{A-20}$$

$$M_1 = T\ v_\theta^{(n)}$$

$$L_1 = -T\ \bar{E}_r(r^{(n)}, \theta^{(n)})$$

$$K_1 = -T\ \bar{E}_\theta(r^{(n)}, \theta^{(n)})$$

$$N_2 = T\ (v_r^{(n)} + \frac{L_1}{2}) \tag{A-21}$$

$$M_2 = T\ (v_\theta^{(n)} + \frac{K_1}{2})$$

$$L_2 = -T\ \bar{E}_r(r^{(n)} + \frac{N_2}{2},\ \theta^{(n)} + \frac{M_1}{2})$$

$$K_2 = -T\ \bar{E}_\theta(r^{(n)} + \frac{N_2}{2},\ \theta^{(n)} + \frac{M_1}{2})$$

$$N_3 = T\ (v_r^{(n)} + \frac{L_2}{2}) \tag{A-22}$$

$$M_3 = T\ (v_\theta^{(n)} + \frac{K_2}{2})$$

$$L_3 = -T\ \bar{E}_r\left(r^{(n)}+\frac{N_2}{2},\ \theta^{(n)}+\frac{M_2}{2}\right)$$

$$K_3 = -T\ \bar{E}_\theta\left(r^{(n)}+\frac{N_2}{2},\ \theta^{(n)}+\frac{M_2}{2}\right)$$

$$N_4 = T\ \left(v_r^{(n)}+L_3\right) \qquad \text{(A-23)}$$

$$M_4 = T\ \left(v_\theta^{(n)}+K_3\right)$$

$$L_4 = -T\ \bar{E}_r\left(r^{(n)}+N_3,\ \theta^{(n)}+M_3\right)$$

$$K_4 = -T\ \bar{E}_\theta\left(r^{(n)}+N_3,\ \theta^{(n)}+M_3\right)$$

These procedures are carried out by two subroutines: SUBROUTINE LORENZ (F1,F2) and SUBROUTINE RK(Y,T,LORENZ).

In LORENZ, F2(1) is velocity in radial direction, F2(2) is velocity in angular direction, F2(3) and F2(4) are accelerations in radial and angular directions which include electric force, centrifugal force and Coriolis force. In SUBROUTINE RK, the coefficients N,L,M,K are calculated. Array U(4) represents Eq.(A-20), Array Z(4) represents Eq.(A-21), Array W(4) represents Eq.(A-22) and Array S(4) represents Eq.(A-23). The trajectory output is given as coordinates along z and r axis; trajectory tangent and the angle subtended to the origin are also given as outputs.

3.2.6 Space charge effect

The difference formulae Eq.(A-6) may include the space charge density ρ. When one considers the Laplace Equation only (ρ=0), there are just medium (scale) iterations of potential (go back to line 350 of the program), in this case, the space charge array P(I,J) and PP(II,JJ) equal to zero.

When space charge is considered, the calculated space charge array P and PP will be substituted to the big (scale) iterations of potential, Poisson Equation is solved (KD>1).

The space charge density is calculated by

$$\rho = \frac{dQ}{dV} \approx \frac{\Delta Q}{\Delta V} \tag{A-24}$$

where ΔV is volume element surrounding the mesh point, ΔQ is the charge inside the volume. Usually, the volume is an annular shaped space.

Auxiliary mesh lines are used to put mesh point at the center of volume element. It is assumed that the emission current J_i concentrates on each trajectory, if the time Δt_i for the electron to pass the volume element is known, the incident charge from the passing trajectory is

$$\Delta Q = \sum_i J_i \, \Delta t_i \tag{A-25}$$

so, the space charge density ρ in mesh point is

$$\rho = \sum_i J_i \, \Delta t_i / \Delta V \tag{A-26}$$

The space charge calculation is performed simultaneously with the trajectory calculation. When the space charge is inserted into the Poisson Equation, the big (scale) potential iteration will repeat several times controlled by a convergency criteria. In every big (scale) iteration the emitter surface field and current will change slightly due to the space charge effects.

3.2.7 Virtual source size and position

The arrays of last ten points in trajectories: POINTX, POINTY, POINTVR, POINTVC represent the coordinates and velocities along radial and angular directions,respectively.

They are put in SUBROUTINE TARGET to obtain values of the trajectory end point ZEND. These data provide the necessary information to calculate the virtual source size and

positions[2].

3.2.8 Angular current intensity

By using the trajectory and current data the angular intensity calculation is straightforward with the SUBROUTINE IPRIME(CI,SLOPE,KD,LT,ANGI,ALPHA). The relationship is

$$I' = I/\pi\alpha^2 \tag{A-27}$$

where I is total current and α is aperture half angle.

3.2.9 Equi-potential line

There are 20 equipotential lines between cathode and anode voltage. The coordinates of equipotential line, ZC and RC, are output in Tape 13.

3.2.10 Three initial conditions

Wiesner[2] used a method to treat the emitter-anode region as an electron optical lens with the cathode surface as the object and the virtual source as image. The electrons emitted from cathode are divided into three groups.

Cold-electron : zero initial velocity; various initial positions on cathode surface.

Alpha-electron : fixed initial velocity; various initial directions; initial position on cathode apex.

V-electron : various initial velocities; initial direction tangent to apex; initial position on cathode apex.

In the program the three electron types are controled by TY. If TY=0, the Cold and Alpha electron are calculated, if TY=1, V-electrons are calculated. TY is put in Tape 6.

4. Definitions of array and variables

V(I,J) potential value at coarse mesh points

R(I) coordinate of radial mesh points

HC coarse angular mesh size in radians

ATA charge mass ratio of electron

VV(II,JJ) potential value at fine mesh points

RR(II,JJ) coordinate of fine radial mesh points

HCC fine angular mesh size in radians

UU(J) distance from origin to cathode

P(I,J) space charge density in coarse region

VOLUME(I,10) volume of auxiliary mesh cell

HS(I) south mesh size

CJ(LT) emission current density

CI(LT) emission current at cathode

RM(LT) start point of emission current in radial direction

CM(LT) start point of emission current in angular direction

RB(LT) start point of trajectory in radial direction

CB(LT) start point of trajectory in angular direction

SI(LT) emission area on cathode

Y(1)-Y(4) initial values of trajectories and transmision arrays

U(J,K) distance between origin and intercept of angular line going out electhode

U1(J,K) distance between origin and intercept of angular line comming in electrode

IU(J,K) integer mesh point next to U(J,K)

IU1(J,K) integer mesh point before U1(J,K)

KK(K) accumulated node number of electrodes

ZR(100,3) coordinates of electhode nodes

V0(K) potential of electrodes

IK(J) start point of potential iteration

IG(J) end point of potential iteration

JC(100) angular mesh number on node of electrodes

VEQ(20) equipotential values

UB(J) distance between origin and open boundary

VB(J) potential on open boundary points

IB(J) integer mesh number before open boundary

IB1(J) minimum non-normal point before open boundary

IC0(J,K) integer mesh number next to IU(J,K)

IC1(J,K) integer mesh number before IU1(J,K)

VB1(J) interpolation value near open boundary

RX(20,J) distance between origin and intercept of angular line with boundary

RPOINT(KK) distance from origin to node points

HHS(II) south fine mesh size

IIK(JJ) start point for fine potential iteration

EQJ(11) equi-current line

PP(II,JJ) space charge density in fine region

VVOLUME(II,JJ) fine mesh volumes

POINTX(10,LT) coordinate along z axis of last ten points

POINTY(10,LT) coordinate along r axis of last ten points

POINTVR(10,LT) velocity along r axis of last ten points

POINTVC(10,LT) velocity along r axis of last ten points

SLOPE1(LT) trajectory slope of end points

VFINAL(LT) final velocity

5. Input formation

5.1 Tape 6

Tape 6 gives program control and additional input data. Some data can be adjusted according to calculation requirements and computer memory capacity available.

TY : control the three types electron initial conditions.

AF : acceleration factor for overrelaxation, about 1.90.

KB : cllows AF to be a constant or changeable value, usually constant.

LT : control the number of trajectories.

KREADY : control the potential used in the trajectory calculation, for Alpha and V-electrons the previous potential stored in Tape 10 is used to speed up calculation.

WF : work function Φ should be adjusted for different kind emitters.

MO : Demagnification factor of fine mesh size, usually 4 is good enough for accuracy.

KFIELD : control tbe potential calculation with or without space charge effects.

HC : angular mesh size in degree, usually in 3-5 degrees.

5.2 Tape 7

The first digit line is the number of electrodes. It is demanded that every angular line intercepts any electrode less or equal two times, otherwise, the electrodes have to be divided into more pieces end to end. The second digit line is the accumulated number of electrode node points. After the third line but the last one there are coordinates of all node points. They are in sequence with electrode number.

The first column is coordinate along z axis

The second column is coordinate along r axis.

The third column is radius of curvature of electrode at node point.

One should pay enough attention to that the emission area is located between the first and second node region.

The last line of Tape 6 is potential values of each electrode in voltage.

6. output data

The tape 1 controls the display in screen to tell you the performance of running program and some necessary information:

(a) the array dimension requirement for the biggest array V(I,J) or VV(II,JJ) in coarse and fine mesh region. If the dimension is not big enough a modification in the source program is needed.

(b) the assigned computer time, more must be entered if limit is reached.

(c) the convergence of potential iteration, if the potential truncation error remains unchanged, the reason must be found and the AF value adjusted.

(d) If there is abortion of execution due to program mistakes or computer memory limitation, you should observe a messages on the screen.

In additions,

Tape 8 is used to check up data (not often used),

Tape 9 is a temporary file (not often used),

Tape 10 is potential at all mesh points.

Tape 11 is boundary plotting data,

Tape 12 is trajectory plotting data,

Tape 13 is equipotential plotting data, and

Tape 14 is main output data. It contains the surface field F, current density J, trajectory parameters in end point, lateral magnification, angular current intensity and many useful informations.

Reference

1. A.V.Crewe, D.N.Eggenbeger, L.M.Wall, (1968) "Electron Using Field Emission Sources", Rev. Sci. Instrum. 39, 576-583
2. W.J.Keery, K.O.Leedy, & K.F.Galloway, (1976) "Electron beam effects on microelectronic devices", IITRI/SEM, 1976 IV, 507-514
3. L.W. Swanson "Field Emission Source Optics" (to be published)
4. R.F.M. Thornley, (1960) "Recent Development in Scanning Electron Microscopy", Proc. Eur. Reg. Conf. Elect. Microsc. Delft. (ED. by A.L. Houwink and B.J. Spit), 137
5. R.H.Fowler and L.Nordheim, Proc. Roy. Soc., A119 173 (1928)
6. W.Z.Schottky, Phys.,14, 63 (1923)
7. R.D. Young, Phys. Rev. 113,110(1959)
8. L.Nordheim, Proc. Roy. Soc. Lond., Ser. A121,626 (1928)
9. R.Gomer, "Field Emission and Field Ionization" (Harvard Univ. Press, 1961), p.10-11
10. L.W. Swanson and A.E. Bell, "Recent Advances in Field Electron Microscopy of Metals" (Academic Press, Inc. New York 1973 p298)
11. E.L.Murphy and R.H.Good, Phys. Rev. 102, 1464 (1956)
12. A.B. El-kareh and J.C. Wolfe, J. Appl. Phys. Vol 48 No.11 (1977)

13. A.E. Bell and L.W. Swanson, Phys. Rev. B vol 19 No.7 (1979)

14. B.Philip, and M.H.Francis, Phys. Rev. 119. 1. 85-94 (1960)

15. E.W. Muller and T.T. Tsong, "Field Ion Microscopy" (American Elsevier, New York, 1969)

16. L.W. Swanson and N.A. Martin, J. Appl. Phys. vol 46 No.5 (1975)

17. J.E. Wolfe, J.E. Ledges and H.H. Glascick, U.S. Patent 3814975 (1974)

18. E. Munro, Ph.D. dissertation, University of Cambridge, 1972.

19. L.W.Swanson and L.C.Crouser, J Appl. Phys. 40, 4741 (1969)

20. D.W. Tuggle, L.W. Swanson and S.G. Watson, "Spot Shape In A Chromatically Limited Electron Optical System" (to be published)

21. D.W. Tuggle and L.W. Swanson, J. Vac. Technol. B3(1) (1985)

22. A.B. El-karch, J.C. Wolfe and J.E. Wolfe, J. Appl. Phys. 48, 4749 (1977)

23. H. Boersch Experimentells Bestimmung der Energieverleilung in Thermisch Ausgelosten Elektronenstrahlen. Z. Physik 139,115-146

24. J.Orloff, Optik, 63 No.4 (1983) 369-375

25. D.W. Tuggle and S.G. Watson, "A Low Voltage Field Emission Column With A Schottky Emitter" (to be published)

26. R.Gomer, surf. Sci. 38 (1973) 373-393

27. J.A. Becker, "Advances in Catalysis" 7. 136 (1955)

28. D.W. Tuggle (Ph.D. dissertation, Oregon Graduate Center, 1983)

29. W.P. Dyke et al. J. Appl. Phys. 31. 5. (1960)

30. J.C.Wiesner and T.E.Everhart, J. Appl. Phys. 44, 2140 (1973)

31. N.Kang, J.Orloff, L.W.Swanson, D.Tuggle, J. Vac.Sci. Technol. 19, 1077 (1981)

32. A.E.Bell and L.W.Swanson, Phys. Rev. B 19, 7. 3353 (1977)

33. G.A. Massey and M.D. Jone, J. Appl. Phys. 52(6) 3780-3786 June (1981)

34. C. Kittle, "Introduction to Solid State Physics" John Wiley & Sons, Inc. 1976 p162

35. Erwin W. Muller "Modern Research Technology Physics Metallurgy " (American Society of Metals, Cleveland, Ohio. 1953), p33

36. W. Knauer, Optik 59, 334-354 (1981)

37. R.A. Collins and B.H. Blott, Surface Sci. 10 (1968) 349

38. R.W. Strayer et al. "Field emission research final report", 1 May 1957 to 30 April 1960, Contract Nonr-2341(00), Authority NR 372-171, Linfield Research Institute, McMinnville, OR.

39. T.R. Groves, D. Hammond, and H.P. Kuo J. Vac. Sci. Technol. Vol 16 No. 6 1680-1685 (1979)

40. A.V. Crewe, Optik 52,337 (1978)

41. N.K. Kang, D. Tuggle, L.W. Swanson, Optik, 63 No.4 313 (1983)

42. J.M.J. van Leeuwen and G.H. Jansen, Optik, 65 No.3 (1983) 179-207

43. D. Tuggle, L.W. Swanson "Determination of Radius and Work Function of A Schottky Point Cathode From I-V Data" (to be published)